

Diss. ETH ex. B

Diss. ETH No. 11762

Wave Propagation in Viscoelastic and Anisotropic, Cylindrical Structures

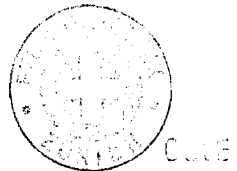
A dissertation submitted to the
SWISS FEDERAL INSTITUTE OF TECHNOLOGY
for the degree of
Doctor of Technical Sciences

presented by

JOHANNES VOLLMANN

Dipl. Bau-Ing. ETH, Masch.-Ing. HTL
born 1 April 1964
Citizen of Oberrohrdorf, AG

Accepted on the recommendation of
Prof. Dr. J. Dual, examiner
Prof. Dr. J.D. Achenbach, coexaminer



Zürich 1996



Copyright © 1996, by Johannes Vollmann
All rights reserved.



The view from my office on a clear winter morning.

To my father

Acknowledgements

This work was carried out during my appointment as an assistant at the Institute of Mechanics, ETH Zürich, a status which gave me the freedom to follow new ideas whenever they came up without the pressure of daily accountability as to the success of these new approaches.

I would like to express my thanks to all of those who contributed to this work, in particular to:

Prof. Dr. J. Dual, who directed the entire work, for his kind support, many helpful suggestions and for carefully supervising each step of this thesis.

Prof. Dr. J.D. Achenbach, Northwestern University, Evanston, Illinois, USA, for reviewing this thesis and for spontaneously accepting the coexamination.

Prof. Dr. M.B. Sayir, chairman of the Institute of Mechanics, ETH Zürich, for providing the spiritual environment in which research is conducted in the sense mentioned above.

Prof. Dr. G. Herrmann, Stanford University, Stanford, California, USA, for many valuable discussions and for inviting me to a workshop on Structural Acoustics, organized by the Office of Naval Research and held at the University of Cambridge, U.K. in Spring 1993, where my eyes were opened to 'modern spectrum estimation methods' for the first time.

Gilbert Schiltges, Roger Breu, and Markus Pfaffinger, not only for the contributions they made with their Diploma-theses, but also for sharing my enthusiasm in the exciting field of wave propagation. All of them became colleagues, working towards their own PhDs.

Sandra Nilssen, for her friendly help concerning the linguistic aspects of this thesis.

Dr. Stephan Kaufmann, for his kind support in solving numerical problems and, last but not least, for 'conducting the orchestra' of our computer network perfectly for many years.

*Johannes Vollmann
Zürich, April 1996*

Table of contents

Abstract	iv
Zusammenfassung	vi
List of symbols	viii
1 Introduction	1
1.1 Previous work	1
1.2 Scope and outline of the present work	3
2 Theory of wave propagation in a shell with viscoelastic core	5
2.1 Nature and representational forms of dispersion	5
2.2 Derivation of the governing equations	7
2.2.1 Dynamic shell equations	7
2.2.2 Wave propagation in the linear viscoelastic cylindrical core	11
2.2.3 Boundary and interface conditions between shell and core	15
2.2.4 Dispersion relation	17
2.2.5 Normalized shell displacement	18
2.2.6 Normalized stress field in the viscoelastic core	19
2.3 Examples of numerical results	20
2.3.1 The empty shell	22
2.3.2 The hypothetical inviscid fluid column with stress-free boundaries ..	24
2.3.3 The shell filled with an inviscid core	27
2.3.4 The shell filled with a dissipative core	31
2.3.5 The shell filled with a shear elastic core	39
2.3.6 Notation of the mode numbering	43
2.4 Conclusions	44

3	High resolution measurement of the complex dispersion relation	47
3.1	Outline of the problem	47
3.2	Experiments	49
3.2.1	Experimental set-up	49
3.2.2	Piezoelectric excitation	52
3.3	Signal processing	54
3.3.1	Spectrum analysis in time domain	55
3.3.2	Spectrum analysis in space domain	55
3.3.3	Confidence and accuracy	63
4	Experimental results versus theory	65
4.1	The empty shell	65
4.2	The shell filled with silicone oil in low frequency range.....	66
4.3	The shell filled with silicone oil in high frequency range.....	69
4.4	The shell filled with alcohol (low viscosity).....	73
4.5	The shell filled with polyisobutylene (high viscosity).....	74
4.6	The linear elastic aluminium rod	76
4.7	Backward wave propagation and boundary movements	81
4.8	Conclusions	86
5	Complete elastic characterization of anisotropic material by guided waves	87
5.1	Motivation.....	87
5.2	Derivation of the dispersion relation of axisymmetric wave modes in a transversely isotropic rod	88
5.2.1	Constitutive equation of anisotropic material	88
5.2.2	Orthotropic and transversely isotropic material	89
5.2.3	Dynamic equations for the transversely isotropic rod	91
5.2.4	Boundary conditions and dispersion relation	95
5.2.5	Special case of axisymmetry	96

5.3	Influence of the material constants on the dispersion relation	99
5.3.1	Variation of the Young's modulus E_{33}	103
5.3.2	Variation of the shear modulus G_{13}	104
5.3.3	Variation of the Young's modulus E_{11}	105
5.3.4	Variation of the Poisson's ratio ν_{12}	106
5.3.5	Variation of the Poisson's ratio ν_{13}	107
5.4	Experiments	108
5.4.1	Longitudinal and radial modes	108
5.4.2	Torsional modes	110
5.5	Determination of the material constants from the measured dispersion relation	112
5.5.1	Determination of E_{33} and G_{13}	112
5.5.2	Determination of E_{11} and ν_{12}	112
5.5.3	Determination of ν_{13}	114
5.5.4	Results for the best fit	115
5.6	Conclusions	117
6	Outlook	119
	Appendix A: Matrix m_{ij}	123
	Appendix B: Shell theory versus exact theory	125
	Appendix C: Matrix a_{ij}	127
	Bibliography	129
	Curriculum vitae	135

Abstract

In this thesis, the complex dispersion relation (frequency versus complex wavenumber) of guided, axisymmetric waves in circular cylindrical structures is investigated theoretically and confirmed by an extended series of experiments. The goal of this work is to understand the topology of the complex wave spectrum for various cylindrical structures, such as elastic shells containing a viscoelastic core, as well as isotropic and anisotropic rods with a circular cross-section in order to determine complex material properties of the structures. In particular, a theoretical model is derived to calculate the complex dispersion relation of axisymmetric wave modes in a thin-walled linear elastic shell containing a viscoelastic core. Curvature and transverse strain cause a coupling between the shell wall bending and longitudinal motion in an empty cylindrical shell. Therefore the dispersion relation of a system consisting of a shell and a viscoelastic core is governed by the shell properties as well as the bulk modulus, the shear modulus, and the density of the core material. By varying the complex moduli, the core can be modelled as an inviscid fluid, an elastic material, or anything between these two extremes.

New dynamic metrology is developed to measure complex dispersion relations in a frequency range of between 1 kHz to 2 MHz with up to 40 travelling wave modes in one single process. With a heterodyne LASER interferometer, which was partly developed at the Institute of Mechanics, ETH Zürich, the radial and the longitudinal displacement of the shell surface is detected. The signals are processed with FFT¹ in the time domain. To decompose the complex wave-number dependence, a complex total least squares algorithm is used in the space domain. This algorithm, originally developed for the signal processing of NMR² signals, demands fewer measurements than FFT and allows a lower signal-to-noise ratio. It extracts both the real and the imaginary part of the wavenumber from the measured data.

The axisymmetric waves are excited with a radially and a longitudinally-acting piezo transducer simultaneously. Most of the experiments are performed using a steel tube with a diameter of 25 mm and a wall thickness of 0.5 mm. The tubes are filled with water, milk, alcohol, glycerine, silicone

-
1. Fast Fourier Transform
 2. Nuclear Magnetic Resonance

oil, and polyisobutylene.

Linear elasticity can be considered as an extreme case of viscoelasticity (long relaxation times compared with the deformation cycles). To ascertain the validity of the theory as well as the computational precision, dispersion curves are also calculated for a shell containing a viscoelastic material behaving like the elastic shell. These results are compared with measured curves of an isotropic aluminium rod where excellent agreement was found.

In the case of the isotropic aluminium rod, the phenomenon of 'backward wave propagation' in which the group velocity and the phase velocity of particular modes have opposite signs, is clearly measured.

The method is finally applied in order to determine material properties of anisotropic materials. In this case, the complex dispersion relation of a carbon fibre-reinforced epoxy rod with cylindrical cross-section is measured. The theory presented by Mirsky in 1965 is implemented and the influence of the material constants on the topology of the dispersion relation is discussed numerically. Using the knowledge of the mode shapes at specific locations in the dispersion diagram, the five material parameters describing the dynamic behaviour of transversely isotropic material can be determined step by step with high accuracy. As the imaginary wave-numbers are measured as well, the frequency-dependent damping behaviour of the composite material is discussed on a qualitative basis.

Zusammenfassung

Die komplexe Dispersionsbeziehung (Frequenz über komplexe Wellenzahl) von axialsymmetrischen, geführten, mechanischen Wellen in kreiszylindrischen Strukturen ist Gegenstand einer theoretischen und experimentellen Untersuchung. Das Ziel der Arbeit besteht im Verständnis der Topologie des komplexen Wellenspektrums von verschiedenen zylindrischen Strukturen wie elastischen Schalen mit viskoelastischem Kern sowie von isotropen und anisotropen Stäben mit Kreisquerschnitt. Dieses Verständnis bildet die Basis zur Bestimmung von Materialeigenschaften mittels Wellenausbreitungsphänomenen.

Ein theoretisches Modell wird hergeleitet, das die Berechnung der komplexen Dispersionsbeziehung von axialsymmetrischen Wellen in dünnwandigen, linearelastischen Zylinderschalen, die mit einem viskoelastischen Material gefüllt sind, ermöglicht.

Durch Krümmung und Querkontraktion der Schalenstruktur entsteht eine wellenlängenabhängige Koppelung zwischen Longitudinal- und Biegebewegungen. Die Dispersionsbeziehung des Systems bestehend aus Schale und Kern wird deshalb durch den Kompressionsmodul, den Schubmodul und die Dichte des Kernmaterials beeinflusst. Die Variation der komplexen Moduli des Kernmaterials ermöglicht die Simulation eines inviskosen Fluids, eines linearelastischen Materials oder jeder beliebigen, "viskoelastischen" Zwischenstufe dieser beiden Extremfälle.

Zur Messung der komplexen Dispersionsbeziehung wurde eigens ein Messverfahren entwickelt, das die Detektion von bis zu 40 lauffähigen Wellenmoden in einem Frequenzbereich von 1 kHz bis 2 MHz ermöglicht. Mit einem heterodynen LASER Interferometer, das teilweise am Institut für Mechanik der ETH Zürich entwickelt wurde, wird die radiale und die longitudinale Bewegung der Schalenwand gemessen. Im Zeitbereich erfolgt die Signalverarbeitung mittels FFT¹. Die Zerlegung der Messsignale im Ortsbereich in ihre harmonischen Bestandteile wird mit einem Algorithmus ausgeführt, der auf der Methode der kleinsten, komplexen Fehlerquadrate beruht. Dieser Algorithmus, der ursprünglich zur Signalverarbeitung von NMR² Signalen geschrieben wurde, kommt mit weniger Stützstellen aus, arbeitet bei einem schlechteren Signal/Rauschverhältnis

1. Fast Fourier Transform
2. Nuclear Magnetic Resonance (Kernspinresonanz)

als FFT und extrahiert sowohl den Real- als auch den Imaginärteil der Wellenzahlen aus den Messsignalen.

Die axialsymmetrischen Wellen werden mit einem radial wirkenden, ringförmigen und teilweise zusätzlich mit einem longitudinal wirkenden piezoelektrischen Transducer angeregt. Die meisten Experimente wurden mit Stahlrohren von 25 mm Durchmesser und 0.5 mm Wandstärke ausgeführt. Dazu wurden die Rohre mit Wasser, Milch, Alkohol, Glycerin, Silikonöl und Polyisobutylen gefüllt.

Lineare Elastizität kann als derjenige Spezialfall der Viskoelastizität betrachtet werden, bei dem die Relaxationszeiten gemessen am zeitlichen Zyklus einer Strukturwelle lang sind. Zur Bestätigung der Gültigkeit des theoretischen Modells und zur Überprüfung der numerischen Zuverlässigkeit des entsprechenden Computerprogrammes, wurde die Dispersionsbeziehung für ein Rohr berechnet, das mit einem hypothetischen, "viskoelastischen" Material gefüllt ist, welches die gleichen dynamischen Eigenschaften hat wie das Rohr selbst. Diese Dispersionskurven zeigen hervorragende Übereinstimmung mit Kurven, die an einem vollen Aluminiumstab mit Kreisquerschnitt gemessen wurden.

An diesem Aluminiumstab konnte das Phänomen der "Backward wave propagation" gemessen werden, ein Bereich einer Dispersionskurve, bei dem Phasen- und Gruppengeschwindigkeit der Strukturwellen entgegengesetzte Vorzeichen haben.

In einer dritten Phase wurde die oben beschriebene Messtechnik zur Bestimmung der Materialeigenschaften von anisotropen Materialien verwendet. Dazu wurde die komplexe Dispersionsbeziehung von axialsymmetrischen Wellen in einem kohlefaserverstärkten Kunststoffstab mit Kreisquerschnitt gemessen und mit theoretischen Dispersionskurven verglichen, die nach der Theorie von Mirsky (1965) berechnet wurden. Mit Hilfe der Kenntnis der Wellenformen an verschiedenen Punkten des Dispersionsdiagrammes konnten die fünf Materialparameter, welche das elastische Verhalten eines transversalisotropen Werkstoffes beschreiben, schrittweise mit hoher Genauigkeit bestimmt werden. Die Messung der Imaginärteile der Wellenzahlen erlaubt zudem eine qualitative Diskussion des frequenzabhängigen Dämpfungsverhaltens.

List of symbols

- A Area and constant
 - A Data matrix (spectrum estimation)
 - B Constant
 - B* Complex bulk modulus
 - C Longitudinal stiffness of a plate (membrane stiffness) and constant
 - C Augmented matrix (spectrum estimation)
 - D Bending stiffness of a plate
 - E Young's modulus
 - E Error matrix (noise) of the data matrix (spectrum estimation)
 - G Shear modulus
 - I Area moment of inertia of unit length
 - J_i Bessel function of order i
 - K_i Bessel function of order i
 - M Moment of unit length
 - N Normal stress resultant of unit length and number of samples
 - Q Shear stress resultant of unit length
 - R Radius of the shell mid-plane and radius of the rod
 - S Centre of gravity and elastic compliance matrix
 - T Relaxation time and period of a harmonic cycle
 - U Matrix (spectrum estimation)
 - V Matrix (spectrum estimation)
 - Y_i Bessel function of order i
 - Σ Diagonal matrix containing singular values (spectrum estimation)
-
- a, b Constants
 - a_{ij} Matrix element
 - b* Complex bulk viscosity
 - b Observation vector (spectrum estimation)
 - c Phase velocity
 - c₀ Velocity of longitudinal waves of infinite wavelength in an elastic bar
 - c₁ Velocity of dilatational waves in an unbounded elastic medium
 - c₂ Velocity of transverse waves in an elastic medium
 - c_p Velocity of longitudinal waves in a thin plate (membrane waves)
 - c_φ* Complex velocity of the potential φ equals complex velocity of dilatational waves in an unbounded viscoelastic medium
 - c_ψ* Complex velocity of the potential ψ equals complex velocity of transverse waves in a viscoelastic medium

c_g	Group velocity
c_{gr}	Real part of complex group velocity
c_{gi}	Imaginary part of complex group velocity
c_{ij}	Elastic constants of anisotropic material
e	Euler's constant
\underline{e}	Unit base vector
f	Frequency and function and index for quantities associated with the core
g	Function
h	Shell wall thickness
i	$\sqrt{-1}$ and general index
j	General index
k	Wavenumber
m	Number of expected modes, prediction order (spectrum estimation)
m_{ij}	Matrix element
n	Constant and polynomial order and order of non-axisymmetric modes
n_t	Number of samples in time domain
n_s	Number of samples in space domain
p	Number of propagating modes and constant
q	Constant
r	Radial coordinate (core and anisotropic rod)
s	Index for quantities associated with the shell
t	Time variable
u	Displacement (general) and radial displacement (anisotropic rod)
v	Circumferential displacement (anisotropic rod)
w	Axial displacement (anisotropic rod)
x	Longitudinal coordinate (shell and core)
y	Radial coordinate within the shell
z	Longitudinal coordinate (anisotropic rod) and constant and sampling index along the specimen (spectrum estimation)
α	Phase angle
$\underline{\alpha}$	Vector (spectrum estimation)
β	Difference between two wavenumbers
γ_0	Angle caused by shear effects
δ_{ij}	Kronecker symbol
δ	0.2 % dynamic penetration depth
ϵ	Strain

ε	Error vector (noise) of the observation vector (spectrum estimation)
η^*	Complex shear viscosity
θ	Circumferential coordinate (anisotropic rod)
ϑ	Circumferential coordinate (shell and core)
κ	Timoshenko's shear coefficient
λ	Wavelength and constant
λ^*	Complex Lamé constant
μ^*	Complex Lamé constant equals complex shear modulus
μ	Constant
ν	Poisson's ratio
ξ	Angle caused by bending
ρ	Density
σ	Normal and shear stress (core) and singular value and variance of Gaussian white noise (spectrum estimation)
τ	Shear stress (anisotropic rod)
φ	Scalar displacement potential
$\underline{\Psi}$	Vectorial displacement potential
ω	Angular frequency
ω_c	Angular cut-off frequency
$()^*$	Complex quantity
$()_{,i}$	Derivative with respect to i
$()'$	Index for reflected waves (isotropic rod)
(\wedge)	Component of normalized vector
A^T	Transpose of matrix A
A^H	Hermitian transpose of matrix A
A^{-1}	Inverse of matrix A
$A^\#$	Pseudoinverse of matrix A (Moore-Penrose inverse)
\widehat{A}	Matrix with less noise
$\ A\ _F$	Frobenius norm of matrix A
\tilde{x}	Normalized quantity x
\underline{x}	Vector x
∇	Nabla operator
Δ	Laplace operator and difference between two numbers

Numbers in [] brackets refer to the bibliography.

1 Introduction

Most of the information about our surrounding world is carried to our sense organs by wave propagation phenomena. Imagine walking in an unfamiliar room in total darkness; one can easily estimate the size of the room or the height of the ceiling, and one can even say whether or not the room is furnished. In this case the human body acts as an emitter and receiver of acoustic waves and most of the information concerning the surrounding world is connected with the time delay between the emitted and the received signals, as well as with the frequency spectrum of the response.

In this investigation, wave propagation phenomena are used to characterize and inspect various cylindrical structures consisting of linear elastic material, isotropic material, combinations of linear elastic and viscoelastic materials, and anisotropic material. The common feature of all structures investigated below is the axisymmetry of the specimen and of the propagating, guided waves. One of the advantages of the axisymmetry is the well-defined geometry and the reduction of radiation loss towards support devices when exciting the structural waves. A further advantage of the axisymmetry is the fact that the energy carried by the waves is focused around the longitudinal axis of the specimen, which is of particular importance for systems with high damping, such as shells containing highly viscous fluids. The theoretical and experimental analysis of the dynamic behaviour of the structure is based on the complex dispersion relation of propagating axisymmetric wave modes. The complex dispersion relation can be considered as a dynamic fingerprint of one particular structure containing information about the geometry and the elastic or viscoelastic properties of the materials forming the structure.

1.1 Previous work

The various aspects of problems relating to wave propagation in a tube filled or surrounded by a fluid have been the subject of numerous studies. Many of these studies pertain to the water hammer effect or to the propagation of heartbeat in human arteries. Recent work deals with both the fields of acoustic radiation and wave scattering of submerged cylindrical shells with various end caps. The aim of the latter is to interpret the

acoustic far field in order to draw conclusions about the shell geometry. The history of analytical description of waves in cylindrical structures dates back to 1876, when Pochhammer [1] published his work. Early work on the water hammer effect was performed by Joukowsky [2] and in 1956, Skalak [3] published an extension of the water hammer theory. A brief overview of further significant contributions to this subject is given by Fuller and Fahy [4]. Heimann and Kolsky [5] contributed to the investigation of waves in thin-walled empty shells, both, theoretically and experimentally in 1966. The problem of a thin-walled elastic shell with a compressible, inviscid fluid was first solved by Lin and Morgan [6] in which the results were limited to real wavenumbers. Assuming the fluid to be inviscid, Fuller and Fahy [4] calculated the dispersion curves for axisymmetric waves ($n=0$) and for the first order non-axisymmetric modes ($n=1$) in the plane of real wavenumber vs. frequency, the plane of imaginary wavenumber vs. frequency, and in the space of complex wavenumber vs. frequency. Guo presented approximate solutions to the dispersion equation for fluid-loaded shells [7] and has studied the attenuation of helical waves in a three-layered shell consisting of elastic and viscoelastic layers [8]. On the experimental side, Plona et al. [9] analysed waves in a thick-walled tube which was surrounded and/or filled with water and compared it with the theoretical results from Sinha et al. [10].

It is generally observed that the number of papers treating this subject experimentally is rather limited when compared with the various theoretical publications which differ mainly in their objectives and assumptions. This might be due to the fact that the number of travelling modes grows with frequency and the group and phase velocities of the various modes are almost equal over wide frequency ranges. Thus the dispersion relation can scarcely be detected by means of measuring arrival times of narrow band pulses or by calculating phase differences of propagating narrow band pulses at two locations, except for the first two modes in a very low frequency range, as recently presented by Lafleur and Shields [11]. For a linear elastic cylindrical rod, a simple but more effective method was used by Zemanek [12]. He was able to measure up to six symmetric and antisymmetric modes in an elastic cylindrical rod with a circular cross-section measuring the frequencies of standing waves.

In 1977 Krause, Goldsmith, and Sackman [13] recorded and published some plots of the strain versus time function of a fluid-filled tube which was subjected to a longitudinal impact. In addition, these results were

compared with those of the extended Skalak water hammer theory [3] by Barez, Goldsmith, and Sackman [14] in 1979.

In the field of anisotropic cylindrical structures, Mirsky [15] published a theoretical investigation of axisymmetric and non-axisymmetric wave propagation in a transversely isotropic, hollow rod with circular cross-section. In a companion paper, he provided numerical results [16]. Mirsky's approach formed the basis for the investigation found in Chapter 5 of this thesis. On the experimental side, Dual [17] detected the first two axisymmetric wave modes in an orthotropic, hollow cylinder and compared it with the theoretical results of Shulga [18] and Ramskaya [19].

Throughout the duration of this thesis work, two text books covering the fundamentals of wave propagation have frequently been consulted: "Wave Propagation in Elastic Solids" by Achenbach [20] and "Wave Motion in Elastic Solids" by Graff [21].

1.2 Scope and outline of the present work

The original motivation of this thesis was the extension of a dynamic viscometer which was developed by Dual [17] at the Institute of Mechanics, ETH Zürich. The principle of this viscometer is the damping measurement of a submerged cylindrical rod or tube vibrating with one of its lower torsional modes, an idea which led to a successfully commercialized product. One of the major problems in the application of such sensors is that most practical, important fluids are viscoelastic in nature. Therefore the dynamic interaction within a thin-walled cylindrical shell containing a viscoelastic core is extensively studied in this thesis with the aim of finding effects which could permit the detection of further fluid properties such as the density and the complex, frequency-dependent shear and bulk moduli.

In a field 'somewhere' between acoustics, fluid mechanics, and solid mechanics, many effects and phenomena interfere with each other, and the borders between these classical disciplines fade with the increasing generality of the constitutive equations. In fluid mechanics, shear resistance in a boundary layer is assumed to be proportional to the velocity gradient, whereas an acoustic fluid is assumed to be inviscid. The various

motivations, the complexity of the interaction of two wave guides, and the lack of powerful computers led to diverse assumptions and simplifications in the past. In this study, a general viscoelastic approach for dilatation and shear deformation of the core material enables one to calculate the dispersion relation of an empty shell, a fluid-filled shell, a shell filled with a viscoelastic medium, and a linear elastic rod with circular cross-section by varying the values of the viscoelastic material properties only.

Many interesting effects have been found in this way, thus forming a basis for the development of future fluid sensors, as outlined in detail in Chapter 2.

Another main achievement is the development of a new high resolution measurement technique for the detection of complex dispersion relations. Before this method was introduced, the frequency-wavespeed dependence of waves propagating in one dimension in rods and plates has typically been measured with narrow band pulses multiplied by Hanning windows. The propagating pulses were then recorded at two locations along the specimen. The phase velocity was calculated from the difference of the two phase spectra and the distance between the locations. This method, however, is completely inadequate if more than one mode propagating with similar group velocities are present and/or if reflected pulses from the ends of the specimen interfere with the outgoing pulses. The new method, introduced in Chapter 3 of this thesis, is based on the following idea: All modes of interest should be excited simultaneously by broad band pulses. If the displacement function is recorded at many points along the specimen during a certain period, a spectrum analysis in time domain and a spectrum analysis in space domain lead directly to the dispersion curves, no matter how many modes or reflections are present. For the signal processing of the experiments in this thesis, the combination of FFT, used for the spectrum analysis in time domain, and a total least squares algorithm, used for the spectrum analysis in space domain, provided excellent results, while keeping the required computer capacity at a reasonable level.

The new method, first applied to cylindrical shells containing several viscoelastic liquids, has since been successfully applied to measure the complex dispersion relation of longitudinal/radial and torsional modes of a transversely isotropic rod in order to determine the elastic properties of the fibre-reinforced composite material.

2 Theory of wave propagation in a shell with viscoelastic core

2.1 Nature and representational forms of dispersion

Constructive interference between P-, SH- and SV-waves and their reflections in a three-dimensional medium of finite cross-sectional dimensions causes so-called 'wave modes' of guided waves in structures. In a limited interval of frequency and wavenumber, a finite number of propagating modes regularly exists. In the case of axisymmetric waves in a cylindrical structure, it is sufficient to consider one-dimensional wave propagation in the direction of the symmetry axis (*x*-axis) in order to characterize a three-dimensional structure. The propagating harmonic waves can be described as follows:

$$u(x, t) = \sum_{n=1}^{n=p} (A_n e^{i(\omega t + k_n x)} + B_n e^{i(\omega t - k_n x)}) \quad (2.1)$$

in which *u* denotes the displacement of a surface point of the structure and *p* denotes the number of travelling modes in the *x*-direction. Here ω indicates the frequency and *k* the complex wavenumber which can be regarded as 'frequency' in space domain. The imaginary part of the wavenumber *k* indicates a decaying or a growing wave mode depending on its sign, whereas the constants A_n and B_n describe the size of the amplitudes.

Dispersion diagrams referring to a steel shell with a diameter of 26 mm, a wall thickness of 0.5 mm, and filled with silicone oil are presented here to illustrate different representational forms of dispersion. Detailed physical interpretations of the shapes of the curves are given in Section 2.3. Regarding Eq. (2.1), the clearest way to represent a dispersion relation is by drawing curves in the ωk plane, as shown in Fig. 2.1. Here *R* denotes the mean radius of the shell, *h* the wall thickness, and c_p the velocity of longitudinal waves in a plate (see Appendix A of this thesis). However, other forms like phase velocity versus frequency (Fig. 2.2) or group velocity versus frequency (Fig. 2.3) are also very common. All diagrams shown in Fig. 2.1, Fig. 2.2, and Fig. 2.3 represent the same dispersion relation,

thus providing clarity for those readers who are not familiar with the ωk form. Since the experimental verification directly yields ω versus k , the theoretical dispersion curves will also be represented in the frequency-wavenumber plane or in the space defined by real frequency and complex wavenumber in the following.

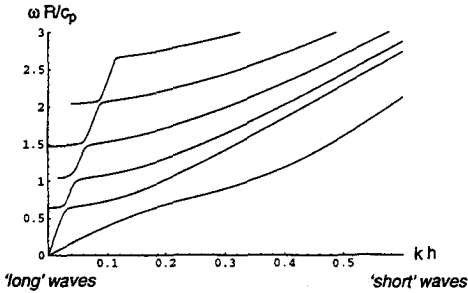


Fig. 2.1 'Normalized frequency versus normalized wavenumber' representational form of axisymmetric wave modes in a fluid-filled cylindrical shell.

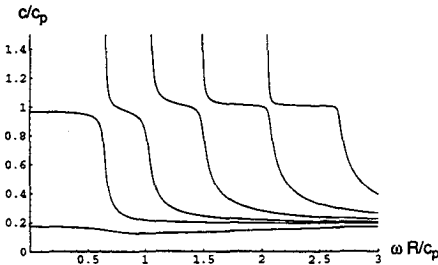


Fig. 2.2 'Normalized phase velocity versus normalized frequency' representational form of axisymmetric wave modes in a fluid-filled cylindrical shell.

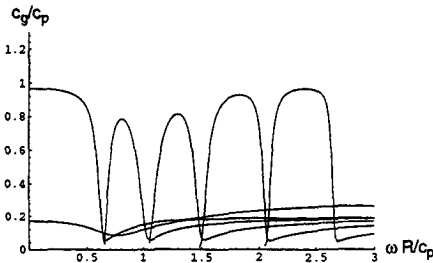


Fig. 2.3 'Normalized group velocity versus normalized frequency' representational form of axisymmetric wave modes in a fluid-filled cylindrical shell.

2.2 Derivation of the governing equations

2.2.1 Dynamic shell equations

A model for isotropic thin-walled elastic shells, including effects of shear deformation and rotary inertia, forms the basis of the dispersion relation. Despite the fact that torsional modes are axisymmetric as well, they are not considered in this investigation. Thus the dynamic equilibrium of an infinite shell element bordering the viscoelastic core is formulated in the plane defined by the radial and the longitudinal coordinate. In Fig. 2.4 the forces acting on a differential shell element are shown.

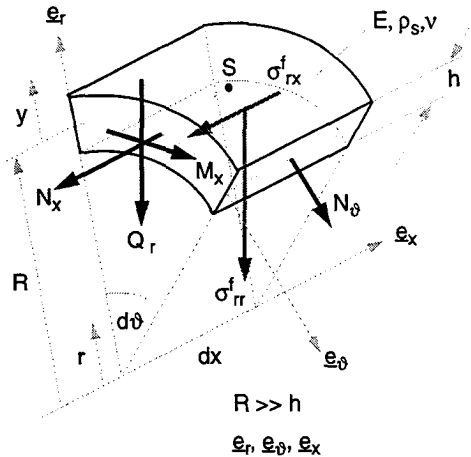


Fig. 2.4 Differential shell element and forces involved in axisymmetric wave propagation.

$$N_{x,x} = \rho_s h u_{x,tt} + \sigma_{rx}^f \tag{2.2}$$

$$Q_{r,x} - \frac{N_{\theta}}{R} = \rho_s h u_{r,tt} + \sigma_{rr}^f \tag{2.3}$$

$$-M_{x,x} + Q_r = \rho_s I \xi_{,tt} + \sigma_{rx}^f \frac{h}{2} \tag{2.4}$$

In Eq. (2.2), Eq. (2.3), and Eq. (2.4), σ^f denotes the stress at the interface between the inner shell surface and the viscoelastic core medium. The term I indicates the moment of inertia, and ξ the slope of the cross-section due to bending. In general, index s designates terms associated with the shell and index f designates terms associated with the core. Derivatives are written in the short form: $u_{r,x}$ denotes the derivative of the radial displacement u_r with respect to x .

According to Timoshenko [22], effects of shear deformation and rotary inertia of the linear elastic shell are considered. Here the 'wrong' assumption that the cross-section remains plane is corrected by the factor κ . Values for κ depend on the shape of the cross-section and are chosen from a publication by Cowper [23]. The limits of the author's approach were evaluated by comparing the results for an empty shell with those of the exact, three-dimensional theory presented by Herrmann and Mirsky [24]. The difference between the exact theory and the approximate theory amounted to less than 1 % for the frequency range considered (see Appendix B).

Fig. 2.5 and Eq. (2.5) show that the derivative of the deflection u_r with respect to the longitudinal coordinate x consists of a part caused by bending (ξ) and a part caused by shear deformation (γ_0).

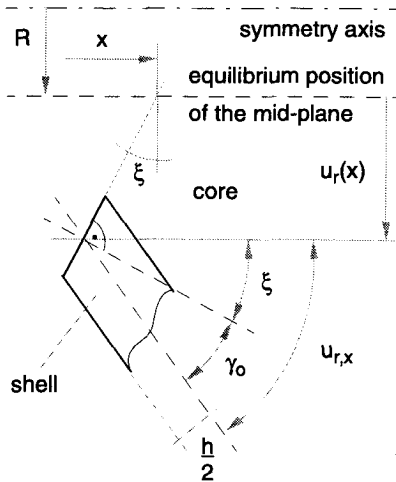


Fig. 2.5 Deflection of the cross-section of a shell element due to bending and shear deformation.

$$u_{r,x} = \xi + \gamma_0 \quad (2.5)$$

Using the kinematic relations for cylindrical coordinates, Eq. (2.6), Eq. (2.7) and the constitutive equations for linear elastic shell material, Eq. (2.8), Eq. (2.9), the stress resultants M , N , and Q are obtained by integrating the stresses through the thickness of the shell element (see Eq. (2.10) to Eq. (2.13)).

$$\varepsilon_x = u_{x,x} - \xi y \quad (2.6)$$

$$\varepsilon_\theta = \frac{u_r}{R} \quad (2.7)$$

$$\sigma_x = \frac{E}{1-\nu^2} (\varepsilon_x + \nu \varepsilon_\theta) \quad (2.8)$$

$$\sigma_\theta = \frac{E}{1-\nu^2} (\varepsilon_\theta + \nu \varepsilon_x) \quad (2.9)$$

y indicates the integration variable in the shell wall in radial direction, and higher order terms are neglected.

$$N_x = \int_{-\frac{h}{2}}^{\frac{h}{2}} \sigma_x dy = \frac{Eh}{1-\nu^2} \left(u_{x,x} + \nu \frac{u_r}{R} \right) \quad (2.10)$$

$$N_\theta = \int_{-\frac{h}{2}}^{\frac{h}{2}} \sigma_\theta dy = \frac{Eh}{1-\nu^2} \left(\frac{u_r}{R} + \nu u_{x,x} \right) \quad (2.11)$$

$$Q_r = hG\kappa(u_{r,x} - \xi) \quad (2.12)$$

$$M_x = \int_{-\frac{h}{2}}^{\frac{h}{2}} y\sigma_x dy = -\frac{Eh^3}{12(1-\nu^2)}\xi_{,x} \quad (2.13)$$

Substituting the expressions for the stress resultants M , N , and Q into Eq. (2.2), Eq. (2.3), and Eq. (2.4) and eliminating ξ , leads to Eq. (2.14) and Eq. (2.15), a system of two coupled differential equations. In these equations, D denotes the bending stiffness of a plate [$D := Eh^3 / (12(1-\nu^2))$] and C denotes the longitudinal stiffness of a plate [$C := Eh / (1-\nu^2)$]. It can easily be seen that in the limit $R \rightarrow \infty$, Eq. (2.14) and Eq. (2.15) are decoupled and represent the dynamic equations for bending waves and longitudinal waves in a thin plate, respectively.

$$\begin{aligned} & D u_{r,xxxx}^s - \left(\frac{D\rho_s}{\kappa G} + \rho_s l \right) u_{r,ttxx}^s - \frac{D}{\kappa Gh} \left[\sigma_{rr,xx}^f + \frac{C}{R} \left(\frac{u_{r,xx}^s}{R} + \nu u_{x,xxx}^s \right) \right] \\ & + \left(\rho_s h + \frac{C\rho_s l}{R^2 \kappa Gh} \right) u_{r,tt}^s + \frac{C}{R} \left(\frac{u_r^s}{R} + \nu u_{x,x}^s \right) \\ & = -\sigma_{rr}^f + \sigma_{rx,x}^f \frac{h}{2} - \frac{\rho_s l}{\kappa Gh} \left[\sigma_{rr,tt}^f + \rho_s h u_{r,tttt}^s + \frac{C}{R} \nu u_{x,ttx}^s \right] \end{aligned} \quad (2.14)$$

$$C \left(u_{x,xx}^s + \nu \frac{u_{r,x}^s}{R} \right) = \rho_s h u_{x,tt}^s + \sigma_{rx}^f \quad (2.15)$$

The next step in deriving the dispersion relation is the formulation of the interface stress σ_{rr}^f and σ_{rx}^f as a function of shell displacement.

2.2.2 Wave propagation in the linear viscoelastic cylindrical core

To describe the interface stresses between the shell and the viscoelastic core, wave propagation in the three-dimensional core must be investigated. For harmonic time functions, the constitutive equation for isotropic linear viscoelastic material is derived from the equations for linear elastic material, written in terms of Lamé constants λ and μ , see Eq. (2.16).

$$\sigma_{ij} = \lambda \delta_{ij} \epsilon_{kk} + 2\mu \epsilon_{ij} \tag{2.16}$$

By adding loss moduli to the storage moduli, the whole investigation becomes complex:

$$\sigma_{ij} = \lambda^*(\omega) \delta_{ij} \epsilon_{kk} + 2\mu^*(\omega) \epsilon_{ij} \tag{2.17}$$

In Eq. (2.17), λ^* and μ^* are complex, frequency-dependent functions describing the relation between stress σ_{ij} and strain ϵ_{ij} . The Kronecker symbol is denoted by δ_{ij} . In general, the asterisk * designates values which are complex due to viscoelasticity.

In this investigation, Maxwell models are used for both $\lambda^*(\omega)$ and $\mu^*(\omega)$, represented in Eq. (2.18) and Eq. (2.19), in order to represent the viscoelastic behaviour of the medium. As illustrated in Fig. 2.6, this model consists of a spring and a damper on the same axis subjected to the same force. For high frequency, compared with the reciprocal value of the relaxation time T , this model is governed by the spring and for low frequency by the damper.

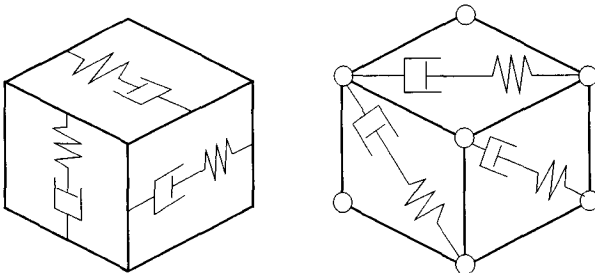


Fig. 2.6 Illustration of Maxwell behaviour for dilatation and shear deformation.

$$\lambda^*(\omega) = \frac{\lambda_0 i \omega}{i \omega + 1/T_\lambda} \quad (2.18)$$

$$\mu^*(\omega) = \frac{\mu_0 i \omega}{i \omega + 1/T_\mu} \quad (2.19)$$

Eq. (2.19) shows the complex shear modulus μ^* and Eq. (2.20) the complex bulk modulus B^* .

$$B^*(\omega) = \lambda^*(\omega) + \frac{2}{3}\mu^*(\omega) \quad (2.20)$$

Eq. (2.21) represents the complex shear viscosity η^* and Eq. (2.22) the complex bulk viscosity b^* , two definitions which help to visualize the properties of the core material.

$$\eta^*(\omega) = \frac{\mu^*(\omega)}{i \omega} \quad (2.21)$$

$$b^*(\omega) = \frac{\lambda^*(\omega)}{i \omega} + \frac{2}{3} \frac{\mu^*(\omega)}{i \omega} \quad (2.22)$$

A Maxwell model is one of the simplest models used to characterize viscoelastic material behaviour. However, if experimental results show reason to use a more sophisticated model, this can easily be realized by modifying Eq. (2.18) and Eq. (2.19).

The displacement field is expressed in terms of derivatives of potentials, as shown in Eq. (2.23). This form decomposes the displacement field in a dilatational part, associated with φ , and a rotational part, associated with Ψ .

$$\underline{u}^f = \underline{\nabla} \varphi + \underline{\nabla} \times \underline{\Psi} \quad (2.23)$$

Since the motion is assumed to be axisymmetric and torsional modes are

not considered in this investigation, all derivatives with respect to ϑ vanish and the vector field $\underline{\Psi}$ is reduced to one dimension, as shown in Eq. (2.24).

$$\underline{\Psi} = \begin{pmatrix} 0 \\ \Psi \\ 0 \end{pmatrix} \quad (2.24)$$

The approach used in Eq. (2.23) enables one to separate the dynamic equation of motion into two so-called Helmholtz equations, Eq. (2.25) and Eq. (2.26).

$$-\omega^2 \rho_f \varphi - (\lambda^*(\omega) + 2\mu^*(\omega)) \Delta \varphi = 0 \quad (2.25)$$

$$-\omega^2 \rho_f \Psi - \mu^*(\omega) \Delta \Psi = 0 \quad (2.26)$$

The potentials φ and Ψ propagate with the velocities c_φ^* and c_Ψ^* , as specified in Eq. (2.27) and Eq. (2.28). k_φ^* and k_Ψ^* are the corresponding wavenumbers. In linear elasticity, the common designations for c_φ^* and c_Ψ^* are c_1 and c_2 .

$$c_\varphi^* = \sqrt{\frac{\lambda^*(\omega) + 2\mu^*(\omega)}{\rho_f}} \quad ; \quad k_\varphi^* = \frac{\omega}{c_\varphi^*} \quad (2.27)$$

$$c_\Psi^* = \sqrt{\frac{\mu^*(\omega)}{\rho_f}} \quad ; \quad k_\Psi^* = \frac{\omega}{c_\Psi^*} \quad (2.28)$$

To solve the Helmholtz equations Eq. (2.25) and Eq. (2.26), the following assumptions are made for waves propagating along the tube:

$$\varphi(r, x, t) = f(r) e^{i(\omega t - k^* x)} \quad (2.29)$$

$$\Psi(r, x, t) = g(r) e^{i(\omega t - k^* x)} \quad (2.30)$$

The derivatives of the potential functions Eq. (2.29) and Eq. (2.30) are expressed in terms of Laplace operators for cylindrical coordinates, Eq. (2.31) and Eq. (2.32). Substituting these expressions into the Helmholtz equations, the differential equations Eq. (2.33) and Eq. (2.34) for the unknown functions $f(r)$ and $g(r)$ are obtained.

$$\Delta\varphi = \varphi_{,xx} + \frac{1}{r}\varphi_{,r} + \varphi_{,rr} \quad (2.31)$$

$$\Delta\Psi = \begin{pmatrix} 0 \\ \Psi_{,rr} + \frac{1}{r}\Psi_{,r} + \Psi_{,xx} - \frac{1}{r^2}\Psi \\ 0 \end{pmatrix} \quad (2.32)$$

$$r^2 f_{,rr} + r f_{,r} + r^2 (k_\varphi^{*2} - k^{*2}) f = 0 \quad (2.33)$$

$$r^2 g_{,rr} + r g_{,r} + [r^2 (k_\Psi^{*2} - k^{*2}) - 1] g = 0 \quad (2.34)$$

For simplicity of notation, the following abbreviations are used:

$$\beta_\varphi^{*2} := k_\varphi^{*2} - k^{*2} \text{ and } \beta_\Psi^{*2} := k_\Psi^{*2} - k^{*2}.$$

According to Abramowitz and Stegun [25], Eq. (2.33) and Eq. (2.34) are solved by combinations of complex Bessel functions J_0 , J_1 , K_0 , K_1 , represented in Eq. (2.35) and Eq. (2.36), in which a_1, a_2, b_1, b_2 are arbitrary constants to be determined by satisfying boundary and interface conditions.

$$f(r) = a_1 J_0(\beta_\varphi^* r) + a_2 K_0(i\beta_\varphi^* r) \quad (2.35)$$

$$g(r) = b_1 J_1(\beta_\Psi^* r) + b_2 K_1(i\beta_\Psi^* r) \quad (2.36)$$

The displacement field can now be expressed by substituting Eq. (2.29) and Eq. (2.30) into Eq. (2.37).

$$u_r = \varphi_{,r} - \Psi_{,x}$$

$$u_{\theta} = 0$$

$$u_x = \varphi_{,x} + \Psi_{,r} + \frac{1}{r}\Psi \quad (2.37)$$

If the motion is axisymmetric, the radial motion vanishes on the symmetry axis and the axial motion must remain finite. Since the values of the Bessel functions K_0 and K_1 go to infinity for r going to zero, this condition can only be satisfied if the values of the constants a_2 and b_2 are set to zero. The kinematic relations for the axisymmetric case [Eq. (2.38)],

$$\begin{aligned} \varepsilon_{rr} &= u_{r,r} & ; \quad \varepsilon_{\theta\theta} &= \frac{u_r}{r} \\ \varepsilon_{xx} &= u_{x,x} & ; \quad \varepsilon_{rx} &= \frac{1}{2}(u_{r,x} + u_{x,r}) \end{aligned} \quad (2.38)$$

combined with the stress-strain relations [Eq. (2.17)], represent the final step in formulating the problem.

2.2.3 Boundary and interface conditions between shell and core

At the interface between the shell and the viscoelastic core ($r = R-h/2$), the radial displacement is equal and the components of the stress vector are equal with opposite directions. The stress functions in the cylindrical core, $\sigma_{rr}^f(r)$ and $\sigma_{rx}^f(r)$, are presented in Eq. (2.39) and Eq. (2.40).

$$\begin{aligned} \sigma_{rr}^i(r) = e^{i(\omega t - k^*x)} \{ & -J_0(\beta_\phi^* r) [a_1 k^{*2} \lambda^* + a_1 \beta_\phi^{*2} (\lambda^* + 2\mu^*)] \\ & + J_1(\beta_\phi^* r) \left[\frac{2a_1 \mu^* \beta_\phi^*}{r} \right] + J_0(\beta_\psi^* r) [2b_1 i k^* \beta_\psi^* \mu^*] \\ & - J_1(\beta_\psi^* r) \left[\frac{2b_1 i k^* \mu^*}{r} \right] \} \end{aligned} \quad (2.39)$$

$$\begin{aligned} \sigma_{rx}^f(r) = e^{i(\omega t - k^*x)} \mu^* \{ & J_1(\beta_\phi^* r) 2a_1 i k^* \beta_\phi^* \\ & + J_1(\beta_\psi^* r) [b_1 (k^{*2} - \beta_\psi^{*2})] \} \end{aligned} \quad (2.40)$$

For the shell displacement, the following time- and space-harmonic approaches are made:

$$u_r^s = a_r e^{i(\omega t - k^*x)} = u_r^f(r = R - h/2) \quad (2.41)$$

$$u_x^s = a_x e^{i(\omega t - k^*x)} \quad (2.42)$$

Whereas the radial displacement of the shell mid-plane equals the radial displacement at the core interface, the longitudinal displacement at the interface consists of both the longitudinal shell displacement and the displacement caused by the rotation of the cross-section due to shell wall bending [see Eq. (2.43) and Fig. 2.5].

$$u_x^f(r = R - h/2) = u_x^s + \xi \frac{h}{2} = a_x e^{i(\omega t - k^*x)} + \xi \frac{h}{2} \quad (2.43)$$

The deflection component ξ of the cross-section caused by bending is a function of wave speed of lateral waves and vanishes for $c \rightarrow c_2 \sqrt{\kappa}$. The variable c_2 indicates the velocity of shear waves in the shell material [see Eq. (2.44)].

$$c_2 = \sqrt{\frac{E}{2\rho_s(1+\nu)}} \quad (2.44)$$

According to Timoshenko's model [22], lateral and longitudinal modes in a plate can be separated by their mode shapes and the speed limit of lateral waves is given by $c_2\sqrt{\kappa}$. In a shell the relation between longitudinal and lateral motion is frequency dependent and the wave speed can exceed $c_2\sqrt{\kappa}$ due to membrane coupling. For that reason the term $\xi h/2$ in Eq. (2.43) has to be 'switched off' if $c > c_2\sqrt{\kappa}$ as shown in Eq. (2.45)

$$u_x^f(r = R - h/2) = a_x e^{i(\omega t - k^*x)} \quad (2.45)$$

$$- \left\{ \frac{i\omega}{c} a_r e^{i(\omega t - k^*x)} \left(1 - \frac{c^2}{c_2^2 \kappa} \right) \frac{h}{2} \cdot \frac{1}{2} \left(\text{Sign} \left[1 - \frac{(\text{Re}[c])^2}{c_2^2 \kappa} \right] + 1 \right) \right\}$$

in which $\text{Sign}[x] = 1$ for $x > 0$, $\text{Sign}[x] = -1$ for $x < 0$ and $\text{Sign}[x] = 0$ for $x = 0$. The function $\text{Re}[c]$ takes the real part from the complex phase velocity c .

2.2.4 Dispersion relation

Eq. (2.41) and Eq. (2.43) show the interface condition between shell and core. Substituting these equations into Eq. (2.37) provides two linear equations for the arbitrary constants a_x , a_r , a_1 , b_1 . Two further equations are obtained by substituting Eq. (2.39) and Eq. (2.40) into the dynamic shell equations Eq. (2.14) and Eq. (2.15).

$$\begin{bmatrix} m_{11} & m_{12} & m_{13} & m_{14} \\ m_{21} & m_{22} & m_{23} & m_{24} \\ m_{31} & m_{32} & m_{33} & m_{34} \\ m_{41} & m_{42} & m_{43} & m_{44} \end{bmatrix} \begin{pmatrix} a_x \\ a_r \\ a_1 \\ b_1 \end{pmatrix} = \begin{pmatrix} 0 \\ 0 \\ 0 \\ 0 \end{pmatrix} \quad (2.46)$$

This homogeneous system of linear equations for the remaining constants a_x , a_r , a_1 , b_1 [Eq. (2.46)] has non-trivial solutions if the determinant of the coefficients equals zero. (The coefficients m_{ij} are presented in Appendix A of this thesis.)

$$\text{Det}[m_{ij}] = 0 \quad (2.47)$$

Since this condition contains ω , k^* , as well as all geometrical and material parameters of the shell and the viscoelastic core, Eq. (2.47) represents the implicit dispersion relation. Assuming a real ω , the corresponding wavenumbers k_n^* are calculated with a complex root-finding algorithm based on Newton's method. Then ω is increased by $\Delta\omega$ and the wavenumbers of the former step are used as initial values for the next root-finding procedure.

2.2.5 Normalized shell displacement

A knowledge of the shell displacement as a function of frequency is of importance in interpreting the shapes of the various modes. As the shell displacement can be measured in only one direction, this knowledge is also very helpful in determining the optimal angle between the shell axis and the measuring LASER beam.

In general, the relative shell displacement, i.e. the relation between u_x and u_r is complex. Hence it contains information of the amplitude and the relative phase shift between u_x and u_r of continuously propagating wave modes. In Eq. (2.48) the complex relative displacement relation is written in terms of the coefficients m_{ij} found in Appendix A.

$$\frac{a_x}{a_r} = [(m_{42}m_{13} - m_{43})(m_{24}m_{13} - m_{23}m_{14}) + \quad (2.48)$$

$$(m_{23} - m_{22}m_{13})(m_{44}m_{13} - m_{43}m_{14})] /$$

$$[-m_{13}m_{41}(m_{24}m_{13} - m_{23}m_{14}) + m_{13}(m_{44}m_{13} - m_{43}m_{14})]$$

Since a_x and a_r are complex constants, the shell displacements [Eq. (2.41) and Eq. (2.42)] can be written as follows:

$$u_r^s = |a_r| e^{i(\omega t - k^* x) + i\alpha_r} \quad (2.49)$$

$$u_x^s = |a_x| e^{i(\omega t - k^* x) + i\alpha_x} \quad (2.50)$$

Now the complex displacement relation can be separated into the amplitude ratio, Eq. (2.51), and the phase angle between u_x and u_r , Eq. (2.52).

$$\frac{|u_x^s|}{|u_r^s|} = \frac{|a_x|}{|a_r|} = \frac{|a_x|}{|a_r|} = \text{Abs}\left(\frac{a_x}{a_r}\right) \quad (2.51)$$

$$\Delta\alpha = (\alpha_x - \alpha_r) = \text{Arg}\left(\frac{a_x}{a_r}\right) \quad (2.52)$$

Numerical analysis of Eq. (2.52) shows that the phase angle is very sensitive to small differences in the viscoelastic material properties.

2.2.6 Normalized stress field in the viscoelastic core

Another important characteristic feature of the wave modes is their associated stress field. To discuss the penetration depth of the wave propagation in radial direction, the normalized stress vectors $\tilde{\sigma}_{rr}^f$ and $\tilde{\sigma}_{rx}^f$ versus a normalized radial coordinate \tilde{r} are calculated for one particular mode at one particular frequency.

$$\tilde{r} := \frac{r}{R - \frac{h}{2}} \quad (2.53)$$

Transforming the variable r to \tilde{r} in Eq. (2.39) and Eq. (2.40) leads to Eq. (2.54) and Eq. (2.55). Again, these expressions are complex. The real

part represents a snapshot of the stress field in the core, the absolute value represents the highest magnitude ever reached at a specific location during one cycle, and the phase angle between the stress in the core and the stress at the shell wall is associated with the time delay of the stress when propagating in radial direction through the viscoelastic material.

$$\tilde{\sigma}_{rr}^f(\tilde{r}) = \frac{\sigma_{rr}^f(\tilde{r})}{\sigma_{rr}^f(\tilde{r} = 1)} \quad (2.54)$$

$$\tilde{\sigma}_{rx}^f(\tilde{r}) = \frac{\sigma_{rx}^f(\tilde{r})}{\sigma_{rx}^f(\tilde{r} = 1)} \quad (2.55)$$

Eq. (2.54) and Eq. (2.55), which enable one to calculate the normalized *partial* stress due to one travelling mode, are tools for the interpretation of the mode shapes. However, the real stress situation in a system excited with one particular frequency consists of the superposition of the stress fields caused by all travelling modes at that frequency.

2.3 Examples of numerical results

In this research project, the theoretical formulation and the experimental investigation began at the same time and were carried out simultaneously. The experimental feasibility has a strong influence on the selection of the parameters being varied in this section. Most of the experiments are conducted using a steel tube ($E = 2.000 \cdot 10^{11} \text{ N/m}^2$, $\nu = 0.28$, $\rho_s = 7800 \text{ kg/m}^3$) with a diameter of 26 mm and a wall thickness of 0.5 mm, so $R/h = 26$. This parameter, as well as the shell material, will remain unchanged in the investigation below. One of the main interests is the influence of the shear behaviour of the core on the complex dispersion relation. The following aspects may help to clarify the influence of the various material parameters on the shape of the dispersion curves.

In general, wave propagation in a medium demands elasticity to store

potential energy and inertia to store kinetic energy. Therefore, discussing wave propagation in a viscoelastic material deals necessarily with the principal limits of wave propagation. The core material can either be dominantly elastic or dominantly viscous for dilatation and/or shear deformation. A viscous behaviour for dilatation suppresses the propagation of P-waves which leads to dispersion curves similar to those of an empty shell. Since no such material was found in reality, this class will not be discussed.

Firstly, the dynamic behaviour of an empty shell and of a hypothetical fluid column of infinite longitudinal extent is discussed. This approach may help one to understand the dispersion relation of a shell with a viscoelastic core as a blend of two interacting wave guides.

Secondly, the numerical discussion is divided into three main sections according to the nature of the shear resistance of the core:

- A shell filled with an inviscid core material (corresponding to an acoustic fluid)
- A shell filled with a shear dissipative core material (corresponding to a classical fluid)
- A shell filled with a shear elastic core material

In all cases, the real part of the velocity of P-waves $c_{\phi}^* = 1005.66$ m/s [see Eq. (2.27)] and the density of the core $\rho_f = 969.00$ kg/m³ are kept constant, the complex bulk modulus [Eq. (2.20)] being dominantly elastic. The starting point for this numerical investigation are values which have achieved the best fit of a measured dispersion relation of silicone oil with high viscosity at low shear velocity. However, to provide a nondimensional form, the material constants are normalized with the Young's modulus E_s , the shear modulus G_s , and the density ρ_s of the shell material. The relaxation times are normalized with the upper frequency f_{\max} of the considered interval, which equals from 1 kHz to 1.0 MHz.

Normalized core parameter	Inviscid core	Dissipative core	Shear elastic core
λ_0/E_s	$4.9000 * 10^{-3}$	$4.8840 * 10^{-3}$	$4.4003 * 10^{-3}$
$T_\lambda f_{\max}$	$1.0000 * 10^6$	$1.0000 * 10^6$	$1.0000 * 10^6$
μ_0/G_s	$1.2800 * 10^{-11}$	$5.1200 * 10^{-3}$	$6.4000 * 10^{-4}$
$T_\mu f_{\max}$	$1.0000 * 10^{-1}$	$1.0000 * 10^{-2}$	$4.0000 * 10^1$
ρ_f/ρ_s	$1.2400 * 10^{-1}$	$1.2400 * 10^{-1}$	$1.2400 * 10^{-1}$

Table 2.1 Normalized parameters for three classes of core material.

Due to numerical reasons, the values can neither be set to zero nor to infinity, but rather to very high or very low values. For example, a relaxation time T_λ of 1 second already signifies an 'infinitely' long time in a frequency range between 1 kHz and 1 MHz, causing primarily elastic behaviour.

2.3.1 The empty shell

The wave spectrum of axisymmetric wavemodes in the empty cylindrical shell is comprised of three modes only, for the model considered. The torsional mode is excluded from this investigation, as mentioned earlier. The shape of the other modes is either lateral (radial), longitudinal, or both. The lack of material damping and radiation loss leads to purely real dispersion curves, as shown in Fig. 2.7. This dispersion diagram will be discussed beginning with the lowest frequency. For low frequencies and long wavelength, the waves propagate with the velocity of longitudinal waves in a bar c_0 . As soon as the wavelength of membrane waves reaches the circumferential dimension, an additional mode (mode 1) appears as explained by Heimann and Kolsky [5]. In that particular frequency range, a strong coupling between radial and longitudinal motion occurs for both modes. Whereas mode 0 changes its shape from dominantly longitudinal to radial, mode 1 arises as a breathing mode transforming to an almost

purely longitudinal mode. The coupling between radial and longitudinal motion leads to the interaction of a core material with the shell through its shear and bulk resistance.

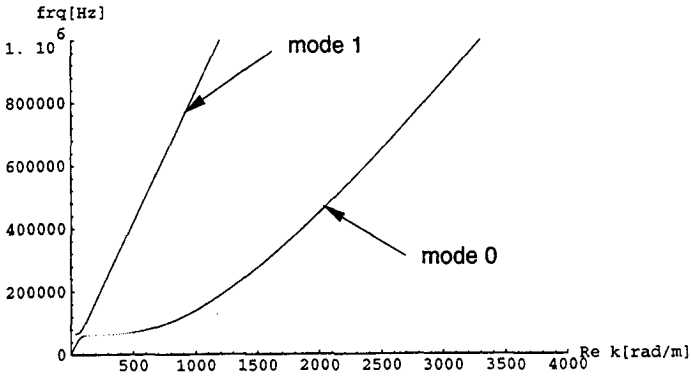


Fig. 2.7 Dispersion diagram of an empty thin-walled shell.

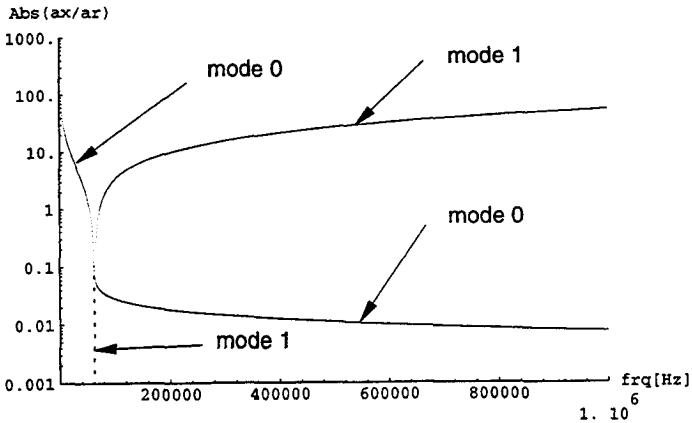


Fig. 2.8 Relation between axial and radial displacement of the empty shell.

2.3.2 The hypothetical inviscid fluid column with stress-free boundaries

Even in a weightless environment, a fluid column with stress-free circumferential boundaries and infinite longitudinal extent would be difficult to realize. It is nevertheless a good tool for the interpretation of the dispersion relations of a cylindrical core which is surrounded by a material of greater stiffness. Fig. 2.9 shows the projection of the dispersion relation of an inviscid fluid column in the k - freq notation. Mode L represents the longitudinal wave in the fluid column.

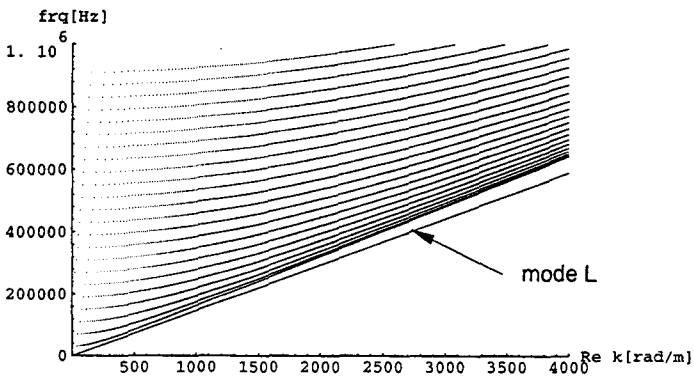


Fig. 2.9 Dispersion diagram of a hypothetical inviscid fluid column with stressfree boundaries. (Projection into the real plane).

Unlike all other mainly radial modes which remain in the real plane (see Fig. 2.10), mode L has a significant imaginary part indicating a relatively strong attenuation. The reason for this dissimilar behaviour of mode L is not understood yet by the author and needs further investigation.

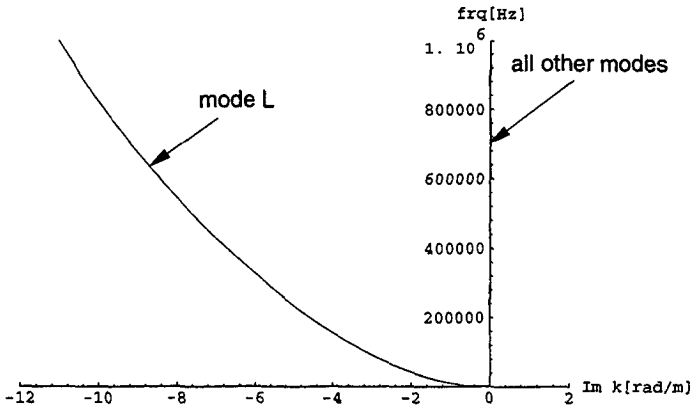


Fig. 2.10 Projection of the dispersion curves of an inviscid fluid column into the imaginary plain.

As the dispersion diagram drawn in the $\text{freq}-c$ notation shows (Fig. 2.11), the phase velocity of mode L is lower than the speed of sound c_ϕ in the fluid. The reason for this diminution of the longitudinal phase velocity is the weakness of the structure in radial direction.

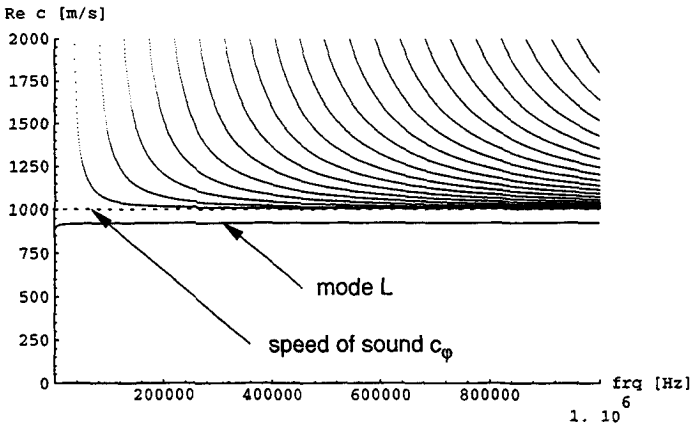


Fig. 2.11 Dispersion diagram of a hypothetical inviscid fluid column with stress-free boundaries. (Projection into the real plane)

Fig. 2.12 shows that mode L is dominantly longitudinal. Lateral contraction forces fluid mass to accelerate in the radial direction, thus reducing the phase velocity of mode L below the speed of sound.

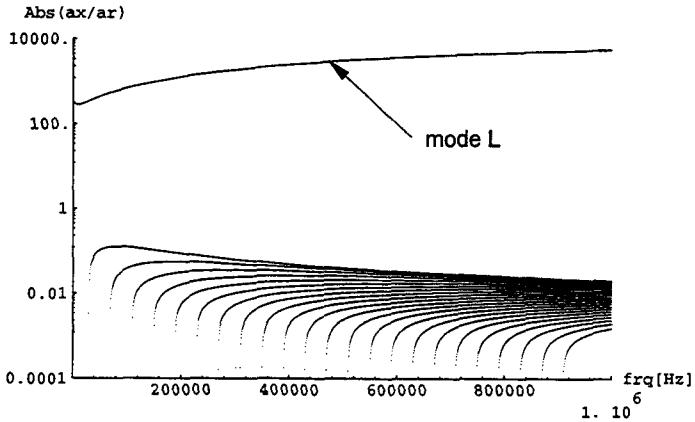


Fig. 2.12 Relation between axial and radial displacement of the circumferential surface of a fluid column.

2.3.3 The shell filled with an inviscid core

In contrast to Fig. 2.7 and Fig. 2.9, in which the behaviour of one single waveguide is presented, all of the following diagrams are determined by a dynamic interaction between shell and core.

Provided that no energy is emitted from the outer surface of the shell, the dispersion curves also remain in the plane of real wavenumber versus frequency when the shell is filled with an inviscid core material, as shown in Fig. 2.13.

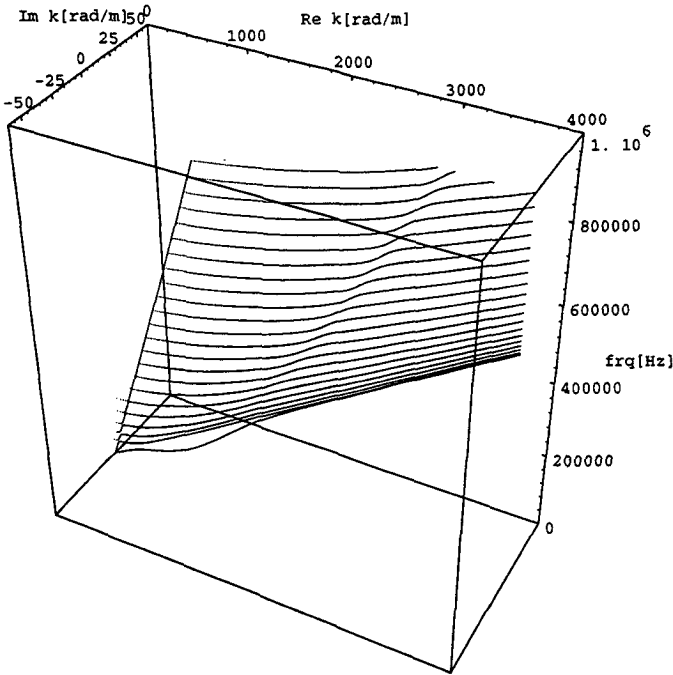


Fig. 2.13 Dispersion curves of the first 24 axisymmetric modes of a shell filled with an inviscid material (acoustic fluid).

The dispersion curves are calculated from the right-hand side to the left, starting with the highest wavenumber. Following the graph of one single mode, a discontinuity in slope appears. As the superposition of the

diagrams for the empty shell and for the shell with inviscid core (Fig. 2.14) shows, this discontinuity is linked with the flexural mode of the empty shell (mode 0 in Fig. 2.7). The straight line of the dispersion curves in Fig. 2.14 is associated with membrane waves in the shell propagating in longitudinal direction with the velocity c_p (see Appendix A of this thesis). The correct shape of the curves on the left side of the straight line can be recognized when observing the first five modes. Except for mode 0 and mode 1, each mode has a cut-off frequency but due to the close proximity of the curves to each other, the root-finding algorithm jumps from one mode to the next lowest mode.

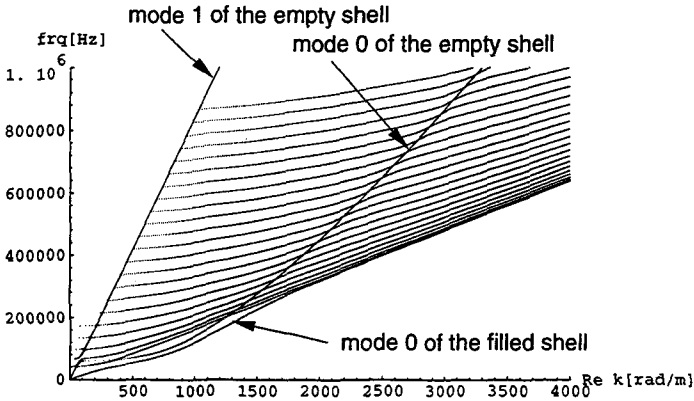


Fig. 2.14 Superposition of the dispersion curves for an empty shell and for a shell filled with an inviscid core material.

In order to explain the different stages of mode shapes along a dispersion curve of one graph, the letters A to E are added to the dispersion curve of mode 19 (Fig. 2.15), as well as to the corresponding graph in the displacement ratio diagram (Fig. 2.16).

Fig. 2.16 shows the absolute value of the normalized complex shell displacement ratio in logarithmic scale versus frequency. Point A indicates the cut-off frequency of mode 19 where the shell is breathing simultaneously over its whole length and the motion is purely radial. The next cut-off frequency, in terms of growing frequency, occurs roughly as soon as the ratio formed by the core radius and a half P-wavelength is an integer.

At point B the longitudinal component of the shell motion is equal to approximately 20 times the radial motion and remains almost constant in a small frequency range before it increases again, reaching its maximum in point C. Following the graph of mode 19 towards higher frequencies leads to point D where the radial motion is dominant again, and remains dominant up to point E and beyond.

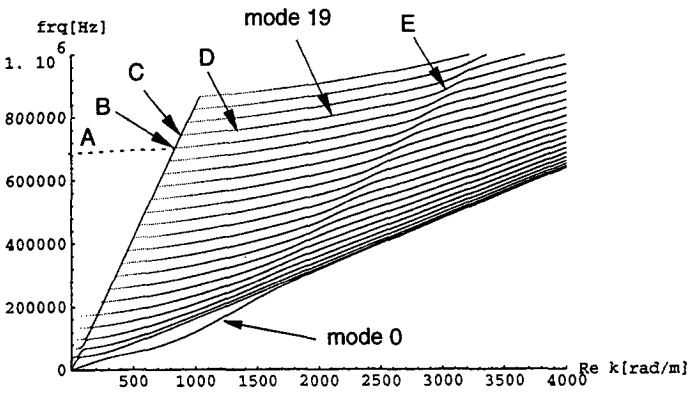


Fig. 2.15 Dispersion curves of the first 24 axisymmetric modes in the real plane

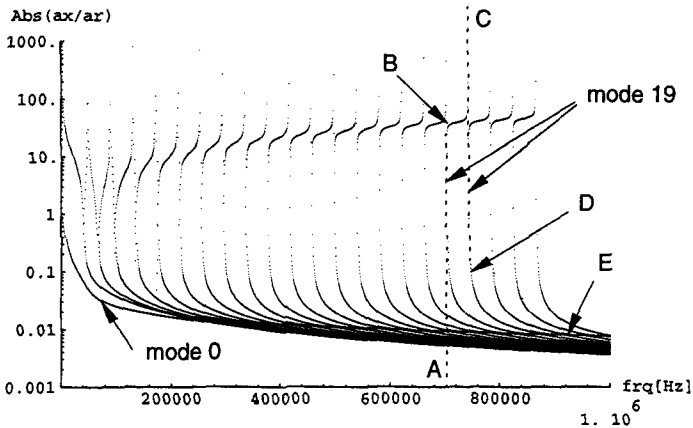


Fig. 2.16 Relation between axial and radial shell displacement of the first 24 axisymmetric wavemodes in a cylindrical shell containing an inviscid material.

Since a_x and a_r are complex, the ratio a_x/a_r can be discussed in terms of amplitudes (see Fig. 2.16) as well as in terms of the relative time delay between the two components, expressed by the argument of the complex ratio. For a shell filled with an inviscid core the phase between a_x and a_r jumps from $-\pi/2$ to $+\pi/2$ so quickly whenever a mode reaches the area of the membrane wave, that no vertical lines can be seen in Fig. 2.17. This situation changes drastically when the core material has shear resistance. To show the line of the phase graph of mode 19, a dashed line has been added to the diagram.

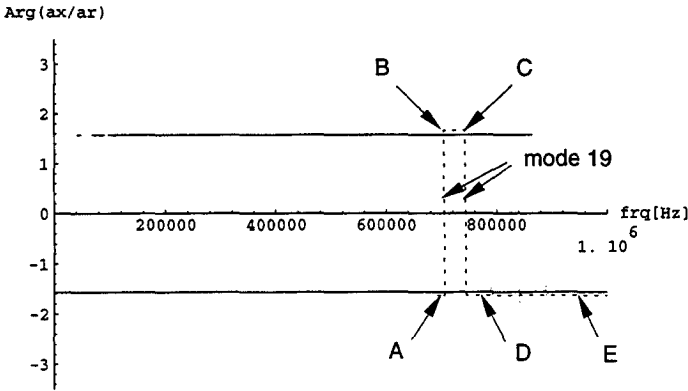


Fig. 2.17 Phase angle between a_x and a_r for the first 24 modes in a shell filled with inviscid material according to Eq. (2.52). The dashed line emphasises mode 19.

2.3.4 The shell filled with a dissipative core

The dissipative shear behaviour of the core causes attenuation of the shell waves, which results in a negative value of the imaginary part of the wavenumber. In order to explain the topology of the dispersion curves of a shell filled with a dissipative core, the quantity δ , representing a dynamic penetration depth is introduced. Eq. (2.56) shows that a wave motion in an arbitrary one-dimensional continuum, described by ω and complex k^* with a negative imaginary part, can be written in terms of an undamped travelling wave times an exponential attenuation factor in z -direction.

$$u(z, t) = ae^{i(\omega t - k^*z)} = ae^{i(\omega t - k_r z)} e^{k_i z} \tag{2.56}$$

$$\delta = \frac{2\pi}{|k_i|} \tag{2.57}$$

According to Eq. (2.57), δ describes the distance in [m] from the emitting source to that point in the viscoelastic medium, where the amplitude has

dropped to about 2 per mill of the initial amplitude, thus providing an approximate value of the penetration depth of mechanical disturbances in an attenuating medium. Assuming z to be a radial coordinate in the core, outgoing from the inner shell surface, the definition of δ is not valid any more due to the cylindrical shape of the core, for the following qualitative discussion, however, it still fits the purpose.

According to Eq. (2.20), the bulk modulus is a function of λ^* and μ^* and therefore a strong shear dissipative behaviour primarily suppresses the propagation of S-waves as well as the propagation of P-waves. Fig. 2.18 shows the normalized thickness of the boundary layer of P-waves in the core material discussed in this subsection to be a function of frequency. One can see that above approximately 700 kHz, δ reaches the order of magnitude of the core radius. This means that the P-waves are 'dead' before they can 'tell' the shell that the core is cylindrical, a fact which leads to a dispersion relation similar to the one of an empty shell for higher frequencies.

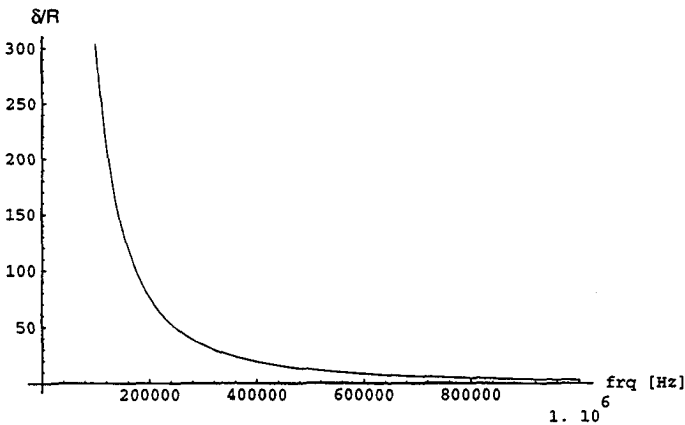


Fig. 2.18 Normalized 2 per mill boundary layer characterizing the attenuation of P-waves in the shear dissipative core material.

Fig. 2.19 shows the complex dispersion relation of a shell filled with a shear dissipative core. The dot in Fig. 2.19 (mode 9) indicates the mode and the frequency for which the stress field is calculated, as represented in Fig. 2.25 to Fig. 2.28 of this section.

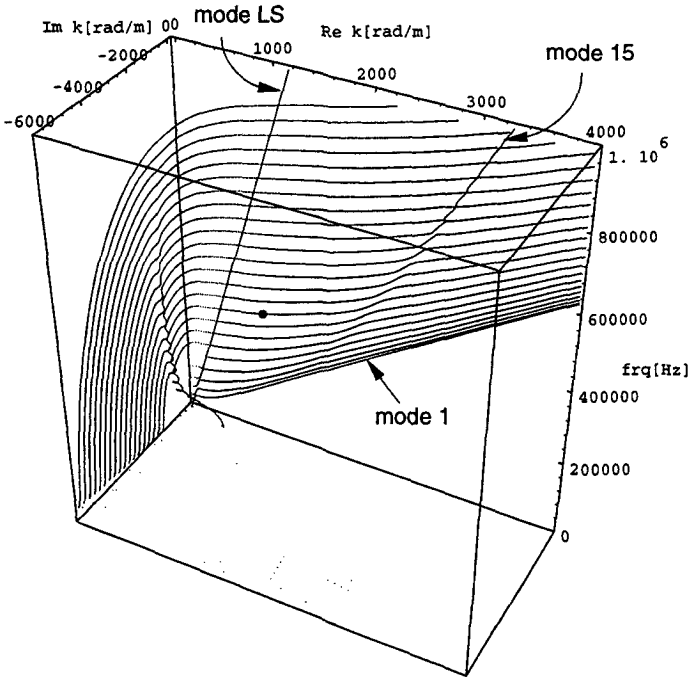


Fig. 2.19 Dispersion curves of axisymmetric modes of a shell filled with a shear dissipative core material (classical fluid).

Difficulties arose while calculating mode 0, in which the root-finding method jumped into mode 1. Mode 0 is therefore not visible in Fig. 2.19 and Fig. 2.20.

The dissipative nature of the core material and the fact that the density of the shell material is approximately ten times the density of the core material leads to a dynamic decoupling of the two waveguides in higher frequency ranges. In terms of growing frequency, this decoupling appears first in the longitudinal shell mode which is coupled with the core primarily through the shear modulus μ^* . Additionally, at higher frequencies the flexural mode of the shell, indicated by the slope-discontinuity of the first 14 modes, arises as a detached mode (mode 15). The two modes in which the decoupling occurs (mode 15 and mode LS) are drawn individually in Fig. 2.21.

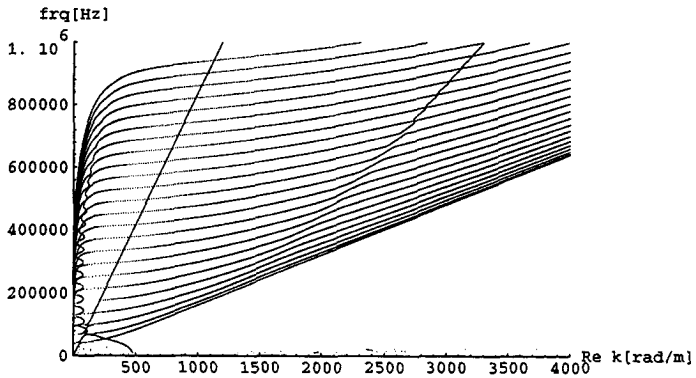


Fig. 2.20 Projection of the curves shown in Fig. 2.19 into the real plane.

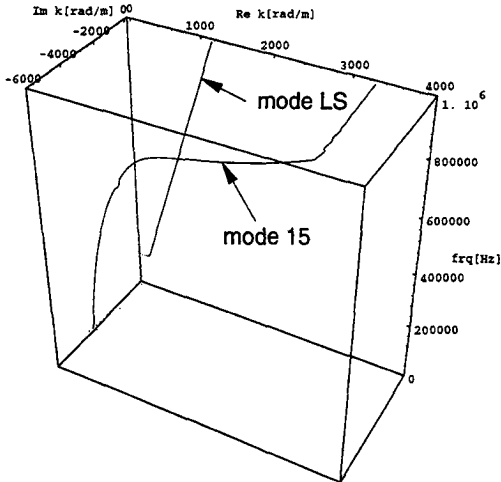


Fig. 2.21 Dispersion curves of the modes which show the decoupling of the shell and the core caused by the dissipative behaviour of the core material.

The projection of the dispersion curves into the imaginary plane

(Fig. 2.22) shows that the detached longitudinal mode (mode LS) has the lowest damping, followed by the detached flexural mode (mode 15).

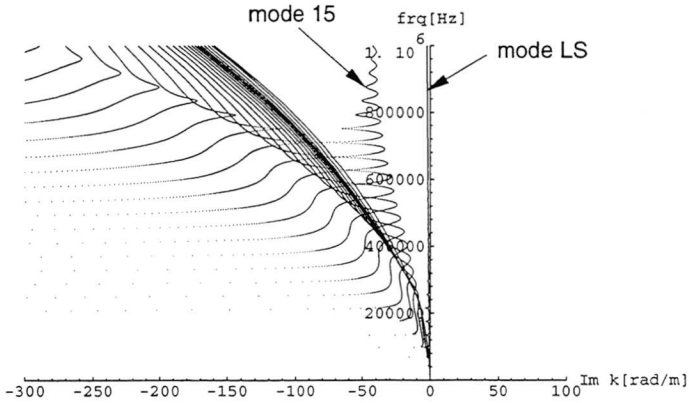


Fig. 2.22 Projection of the curves shown in Fig. 2.19 into the imaginary plane.

In Fig. 2.23 and Fig. 2.24, the absolute value and the argument of the complex displacement ratio are presented.

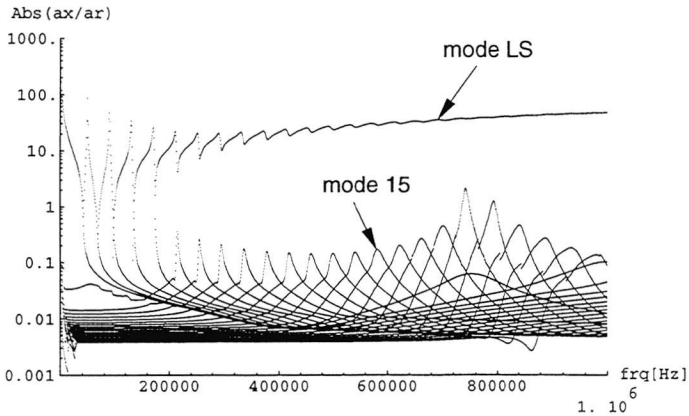


Fig. 2.23 Relation between axial and radial displacement of axisymmetric wavemodes in a cylindrical shell containing a shear dissipative core material.

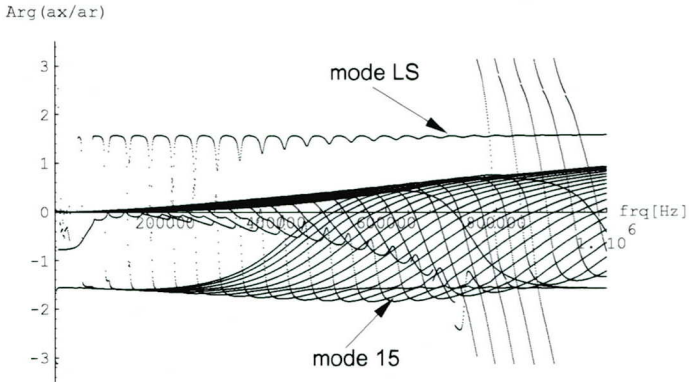


Fig. 2.24 Phase angle between a_x and a_r for axisymmetric modes in a shell filled with shear dissipative material according to Eq. (2.52).

The following diagrams show the normalized radial stress σ_{rr} and the normalized shear stress σ_{rx} in the core material. Mode 9 and a frequency of 360 kHz are chosen as an example.

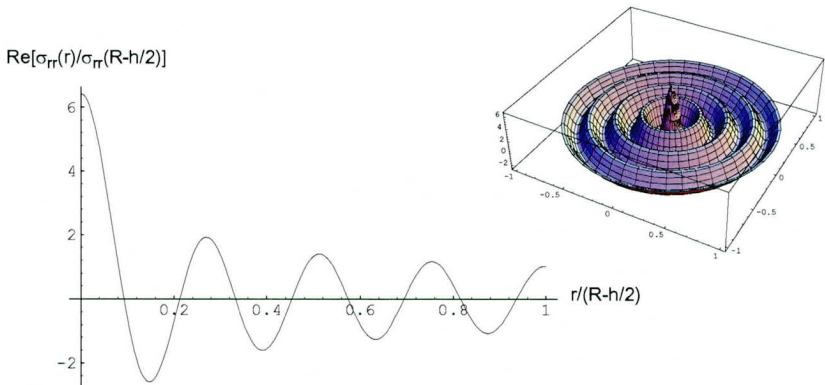


Fig. 2.25 Normalized radial stress σ_{rr} vs. normalized radius for mode 9 at 360 kHz in a shear dissipative core.

In Fig. 2.25 and Fig. 2.27, it can be seen that from geometrical reasons

the radial stress becomes a maximum on the symmetry axis, whereas the shear stress vanishes. Fig. 2.27 shows a quickly-attenuating shear boundary layer (Stokes layer) followed by a curve with increasing amplitude towards the centre. This part of the diagram is governed by the radially-propagating P-waves. To fulfil the dynamic equilibrium conditions, the shear stress in the core σ_{rx} grows with the rate of the normal stress σ_{rr} .

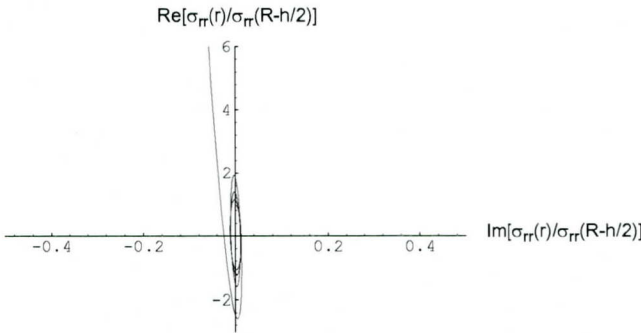


Fig. 2.26 Real part of the normalized radial stress σ_{rr} vs. imaginary part of the normalized radial stress σ_{rr} for mode 9 at 360 kHz in a shear dissipative core.

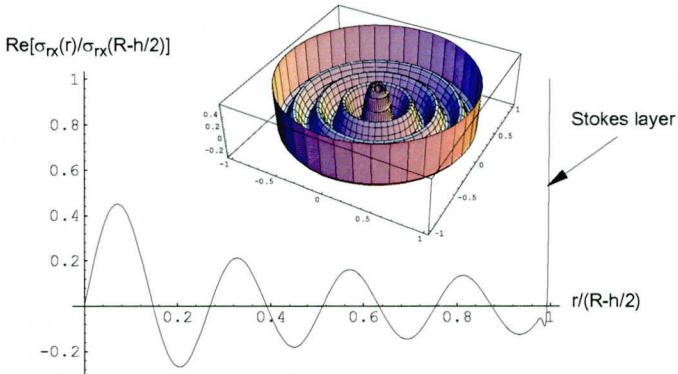


Fig. 2.27 Normalized shear stress σ_{rx} vs. normalized radius for mode 9 at 360 kHz in a shear dissipative core.

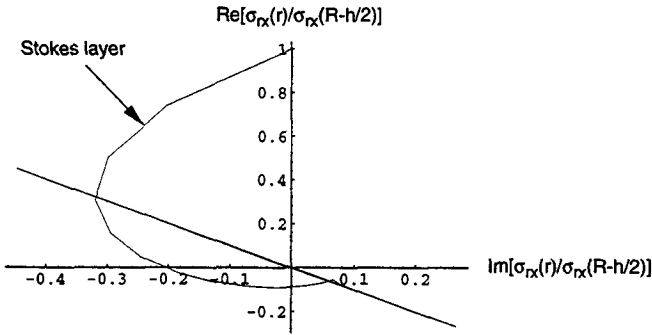


Fig. 2.28 Real part of the normalized shear stress σ_{rx} vs. imaginary part of the normalized shear stress σ_{rx} for mode 9 at 360 kHz in a shear dissipative core.

The interpretation of Fig. 2.26 and Fig. 2.28 demands further explanation. In general, the normalized stress functions according to Eq. (2.54) and Eq. (2.55) are complex and can therefore be written as presented in Eq. (2.58):

$$\vec{\sigma}^f(\tilde{r}) = S(\tilde{r}) e^{i\alpha(\tilde{r})} \quad (2.58)$$

in which a growing α means that waves are propagating from the inner surface of the shell through the core towards the centre. In this case, the graphs of the real stress versus the imaginary stress appear to be more or less circle shaped. On the other hand, if α remains constant, the shell 'is riding on a steady state core vibration' and the graph appears to be a more or less straight line. In Fig. 2.28 both phenomena are visible; the Stokes layer close to the shell wall can be identified as an attenuating, propagating wave, whereas the rest of the graph represents a standing wave, i.e. a vibration of the core in radial direction.

2.3.5 The shell filled with a shear elastic core

The shear elastic parameter set (see Table 2.1) produces the most exciting results. Careful numerical analysis was carried out to ascertain that the effects presented in this section have real physical reasons and are not caused by insufficient accuracy of the root-finding procedure.

In anticipation of Chapter 4 of this thesis (Experimental results versus theory), it should be mentioned that the curves obtained by this parameter set come closest to the measured dispersion curves, in shape and magnitude, for the case of a shell filled with silicone oil.

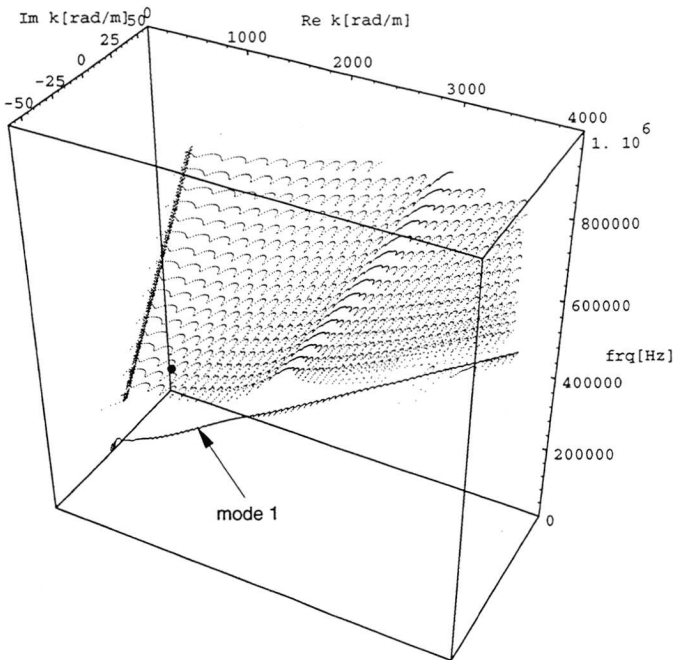


Fig. 2.29 Dispersion curves of axisymmetric modes of a shell filled with a shear elastic core material.

In Fig. 2.29, modes 0, 2, 3, 5, and 6 are not plotted. The dot indicates that the stress field is calculated for mode 9 at 360 kHz.

As shown in Fig. 2.29, increasing the elastic shear resistance leads to

dispersion curves which leave the real plane periodically. Therefore the diagrams for the displacement ratio become very confusing (Fig. 2.30 and Fig. 2.31).

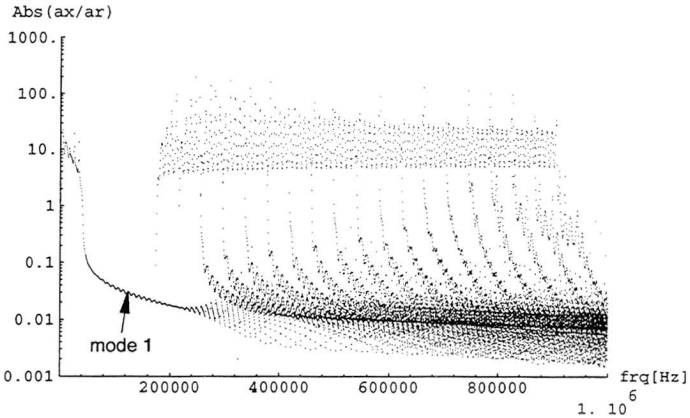


Fig. 2.30 Relation between axial and radial displacement of all axisymmetric wavemodes presented in Fig. 2.29.

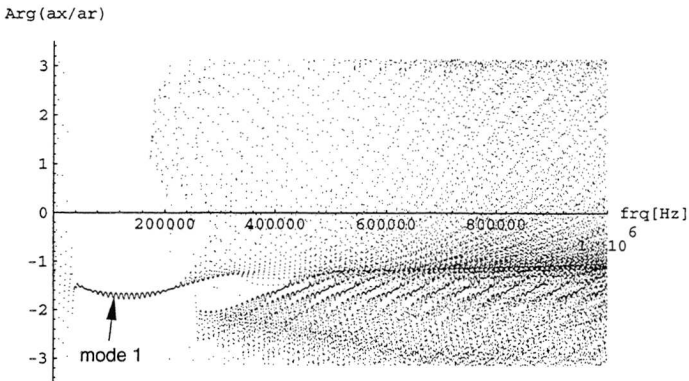


Fig. 2.31 Phase angle between a_x and a_r of all axisymmetric wavemodes presented in Fig. 2.29 according to Eq. (2.52).

Since the propagation velocity of p-waves c_ϕ is (almost) equal for all three classes of core material, the radial stress distribution presented in Fig. 2.32 is very similar to the one presented in Fig. 2.25.

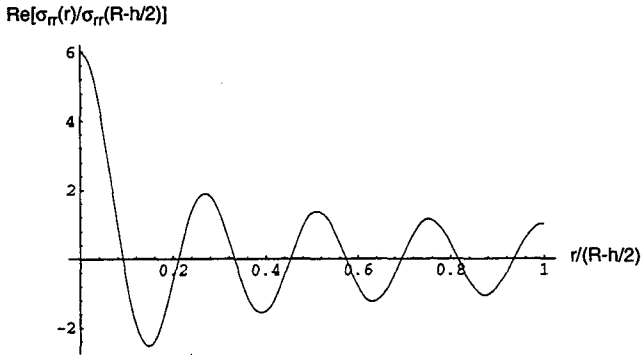


Fig. 2.32 Normalized radial stress σ_{rr} vs. normalized radius for mode 9 at 360 kHz in a shear elastic core.

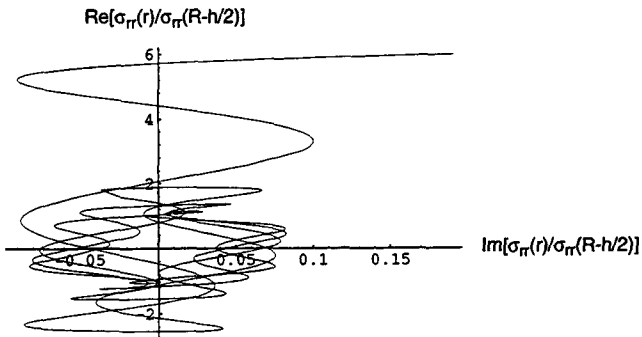


Fig. 2.33 Real part of the normalized radial stress σ_{rr} vs. imaginary part of the normalized radial stress σ_{rr} for mode 9 at 360 kHz in a shear elastic core.

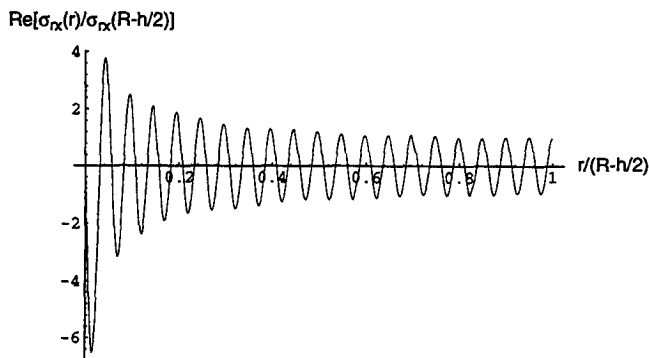


Fig. 2.34 Normalized shear stress σ_{rx} vs. normalized radius for mode 9 at 360 kHz in a shear elastic core.

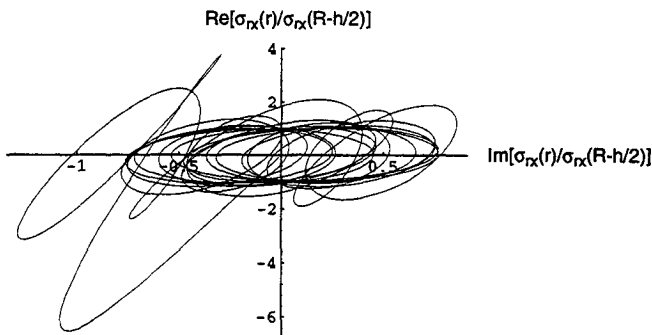


Fig. 2.35 Real part of the normalized shear stress σ_{rx} vs. imaginary part of the normalized shear stress σ_{rx} for mode 9 at 360 kHz in a shear elastic core.

Since the velocity of P-waves is kept constant for all types of fluids, the projection of the radial stress to the real plane in the shear elastic core (Fig. 2.32) is very similar to the corresponding diagram for the dissipative core (Fig. 2.25). As expected, major differences appear in the diagrams representing the shear behaviour. When comparing Fig. 2.34 with

Fig. 2.27, one can see that instead of the thin disappearing Stokes layer, shear waves propagate through the whole core with increasing amplitude towards the symmetry axis, focusing the energy.

Considering the scale of the imaginary axis of Fig. 2.33 and Fig. 2.35, one can see that the graph of the shear stress (Fig. 2.35) is much more 'circle shaped' than the graph of the normal stress (Fig. 2.33), thus indicating a wave propagation towards the centre.

2.3.6 Notation of the mode numbering

The numbering of the modes requires several comments. Mode 0 of the filled shell (see Fig. 2.14) is governed by the 'longitudinal fluid column mode' (mode L) in Fig. 2.9 and has no cut-off frequency. Mode 1 has no cut-off frequency either. Mode 2 is the first mode having a cut-off frequency, at which approximately one P-wavelength in the core equals the diameter of the core or the radius equals a half wave length. Thus eight nodes, i.e. eight half P-wave lengths, can be recognized in the diagrams presenting the radial stress σ_{rr} of mode 9 at 360 kHz (Fig. 2.25 and Fig. 2.32).

2.4 Conclusions

Two wave guides, an elastic shell and a viscoelastic core, have been combined and some aspects of their interaction have been studied.

A theory for thin-walled elastic shells is applied, which provides good results as long as the wall thickness is at least three times smaller than the shortest bending wave length in the shell wall (see Appendix B). In this investigation, the shortest wave length equals 3.2 times the wall thickness. Higher sensitivity of the shell waves to the core properties could be achieved by using a shell material with lower density or a thinner wall thickness. However, to keep the experimental realisation in mind, it should be mentioned that it is difficult to obtain thin-walled elastic tubes of high geometrical accuracy. Therefore shell parameters of a steel tube which is commercially available have been used throughout this numerical investigation.

Among the unlimited number of parameter combinations for the characterization of the viscoelastic core, three main classes have been studied: the inviscid core, the dissipative core, and the shear elastic core, thus establishing three narrow insights into a multi-parametric space.

Since the main interest lies in the dynamic behaviour of the viscoelastic core, the theoretical model developed in this chapter represents a tool for a feasibility study on the way towards a measuring instrument for viscoelastic properties of liquids.

The results can be summarized as follows:

- The projection of the dispersion curves into the plane formed by the real part of the wavenumber and the frequency as well as the cut-off frequencies are highly sensitive to the speed of sound in the core material, which varies in general with the frequency. Thus they can be used to determine the real part of a complex bulk modulus, provided that the density of the core material is known.
- From the imaginary part of the dispersion curves in the area of dominantly radial shell motion, the imaginary part of the complex bulk modulus could be determined.

- A very high sensitivity to the shear resistance of the core material can be identified on the diagrams showing the phase angle between the longitudinal and the radial motion (see Fig. 2.17, Fig. 2.24, and Fig. 2.31). On a future 'fluid' sensor, the time-dependent ratio between a_r and a_x could be directly measured with a micro sensor glued on the shell surface, detecting its acceleration in longitudinal and radial directions.

In this chapter, complex dispersion relations, shell movements, and stress fields have been calculated based on given material properties. However, the practical usage of the phenomena encountered in this way demands the solution of a final challenging obstacle: the inverse problem, or, in other words, 'How can the complex material properties be determined from the measured complex dispersion relations?'

The extreme complexity of the theoretical model and the fact that many effects having no clear borders in the parameter space are involved, impedes an explicit solution.

Therefore the best approach in determining material properties consists of the following steps:

- Focusing on an area of the dispersion relation in which the curves are reasonably sensitive to the material constant of interest.
- Measurement of the dispersion relation in that particular range.
- Determination of the material constant by an optimal fit of the measured curves in an iterative numerical process.

The last step which is performed 'manually' in this investigation can easily be automated in the future. In Chapter 5 this procedure is applied to characterize the material properties of an anisotropic material.

3 High resolution measurement of the complex dispersion relation

3.1 Outline of the problem

In this chapter, a new method is presented to determine the complex dispersion relation directly from a series of displacement recordings along a shell. To explain the metrology, the nature of guided waves propagating along structures of finite cross-sectional dimensions should be outlined first. Small disturbances in an elastic or viscoelastic medium produce P- and S-waves. Constructive interference of these waves and their reflections from the boundaries of the structure leads to 'wave modes' propagating along the structure. These modes may differ in shape, group velocity, phase velocity, and attenuation. In the case of axisymmetric waves in a cylindrical structure, the propagating waves can be described as follows:

$$u(x, t) = \sum_{n=1}^{n=p} (A_n e^{i(\omega t + k_n x)} + B_n e^{i(\omega t - k_n x)}) \quad (3.1)$$

In Eq. (3.1), u denotes the displacement of a surface point of the structure and p the number of travelling modes in the x -direction. ω indicates the circular frequency and k the complex wavenumber which can be regarded as 'frequency' in space domain. The imaginary part of the wavenumber k indicates a decaying or a growing wave mode depending on its sign. A dispersion diagram contains characteristic information about geometry, frequency-dependent material behaviour, and homogeneity of a structure. It is a special advantage of axisymmetric waves in a cylindrical structure that no boundary conditions causing radiation loss have to be considered and that a three-dimensional structure can be inspected or characterized by measuring dispersion relations of one-dimensional wave propagation. To measure a dispersion relation in a defined interval of frequency and wavenumber, a spectrum analysis in time and space domain is required. Applying discrete spectrum analysis methods, two features determining the number of samples and the distance between two consecutive samples (in time and space) must be observed. Firstly, the highest harmonic

component, i.e. the shortest cycle or the shortest wave length, must be sampled at at least two points in time and space respectively.

The second feature concerns the resolution. The question here is how many samples are necessary to separate two neighbouring (in terms of frequency or wavenumber) modes. The resolution of discrete Fourier transformation methods such as FFT grows linearly with the length of the interval over which sampled data is available, and is therefore intrinsically limited by the method. Modern spectrum estimation methods approximate given signals with a harmonic model. Moreover, highly sophisticated methods are able to isolate signals of interest from surrounding noise always present in experimental data. These methods do not have inherent resolution limits, although the prediction quality grows with the number of samples.

In this investigation, a combination of discrete spectrum analysis (FFT) and spectrum estimation (Linear Prediction and Complex Total Least Squares) is seen to be very effective. FFT is applied in order to obtain the complex frequency spectrum versus frequency of recorded shell displacements versus time. In the space domain, a spectrum estimation method is used to decompose the complex wavenumber dependence. Thus the number of required samples in the space domain is reduced to less than a sixth compared with FFT. An additional advantage is the fact that the wavenumbers are decomposed, including their signs indicating the direction of propagation. Thus outgoing pulses can be distinguished from reflected pulses.

Spectrum estimation methods are a still-growing topic in signal processing, and improved algorithms are published frequently. Comprehensive introductions are given by Kay [26], Marple [27] [28], and Hayes [29], as well as in German by Oestreich [30]. A comparison of several methods based on singular value decomposition with FFT is presented by Uike et al. [31]. The algorithm implemented in this investigation, originally developed for the signal processing of NMR signals, was published by Tirendi and Martin [32] and is based on the work of Golub and Van Loan [33] [34]. To the author's knowledge, the work presented in this thesis is one of the first applications of spectrum estimation methods used in structural mechanics to characterize dynamic material properties.

3.2 Experiments

3.2.1 Experimental set-up

The experiments were performed at the Wave Propagation Laboratory of the Institute of Mechanics, ETH Zürich (Fig. 3.1).

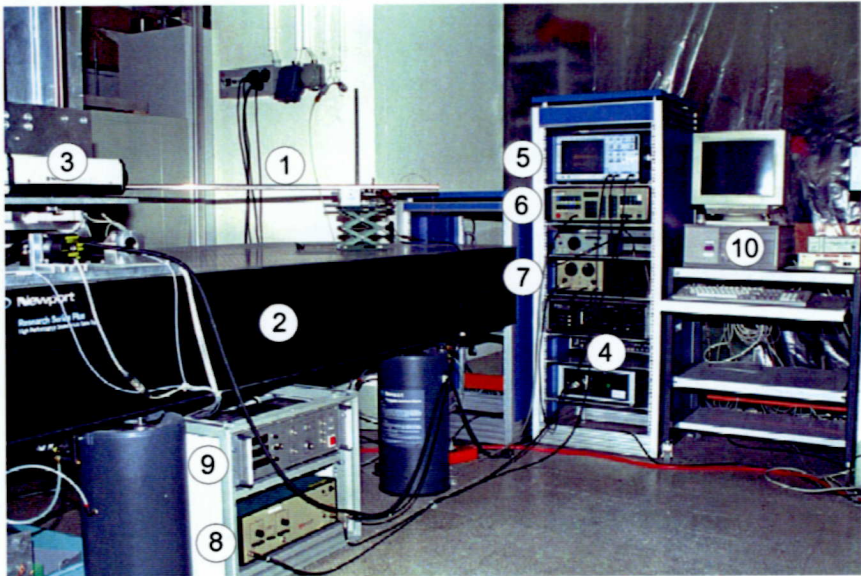


Fig. 3.1 Wave Propagation Laboratory of the Institute of Mechanics, ETH Zürich.

1. Specimen
2. Pneumatically Isolated Research Table: Newport™
3. LASER Sensor Head: Polytec™ OFV 300
4. LASER Demodulators: Polytec™ OFV 2100 and ETH Zürich
5. Digital Storage Oscilloscope: LeCroy™ 9410 Dual 150 MHz
6. Digital Function Generator: Krohn-Hite™ KH 5920
7. Band-Pass Filter: Krohn-Hite™ KH 3202
8. Excitational Signal Amplifier: Krohn-Hite™ KH 7500
9. Stepping Motor Controller of the LASER Head Positioning System
10. PC: Olivetti™ 486, Software: Asyst™ Version 4.01

The order of magnitude of the shell displacements amounts to less than 10 nm. In order to detect such movements and to avoid any disturbance of the travelling waves caused by the measurement itself, the shell displacement function is measured with a heterodyne LASER interferometer which represents the most essential part of the experimental set-up shown in Fig. 3.1. The commercial configuration of this interferometer did not satisfy our resolution requirements in the frequency range, of interest. Therefore a demodulator for the phase-modulated signal with a 40 MHz carrier frequency was developed by Dual and Hägeli [35] at the Institute of Mechanics, ETH Zürich. This phase demodulator allows the measurement of surface displacements over a frequency range of from 1 kHz to 8 MHz with a resolution of $10^{-13} \text{ m}/\sqrt{\text{Hz}}$.

Fig. 3.2 shows the experimental set-up.

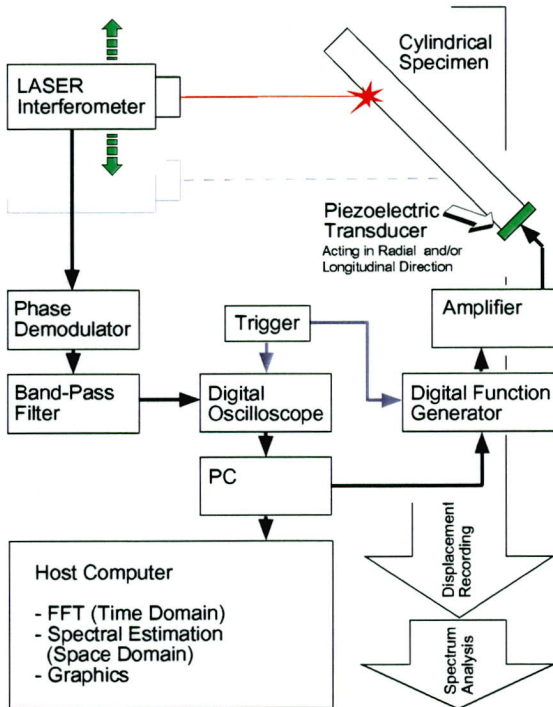


Fig. 3.2 Experimental set-up

Typically the waves are excited by a ring-shaped piezoelectric transducer subjected to a linear sweep pulse with a start frequency of 400 kHz, a stop frequency of 1250 kHz, and a duration of 0.5 ms. This pulse is applied repeatedly with a trigger frequency of 20 Hz. The displacement of the shell surface versus time caused by the outgoing pulse and its reflections is measured and averaged 300 times before the LASER interferometer is shifted to the next location. The displacement function is recorded at up to 160 points along the specimen, depending on the number of expected modes in the frequency range considered.

A typical signal is presented in the screen print of the digital oscilloscope in Fig. 3.3. Here the top graph shows the voltage of the excitation signal and the lower graph the averaged displacement function followed by its amplitude spectrum.

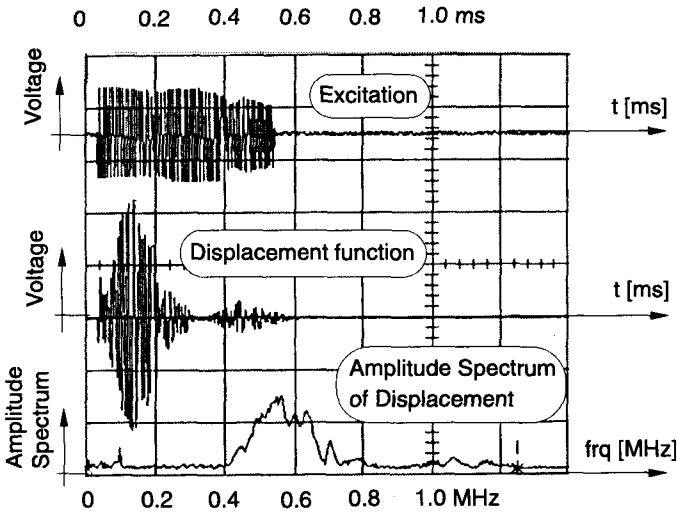


Fig. 3.3 Screen print of the digital oscilloscope displaying:

- Voltage of excitation signal (linear sweep, 400-1250 MHz, 0.5 ms)
- Average of 300 displacement functions (measured at one point)
- Amplitude spectrum of the displacement function above.

(fluid: silicone oil)

- Sampling rate: 5 MHz

3.2.2 Piezoelectric excitation

Piezoelectric transducers are used to convert voltage into mechanical stress. Since the ceramic material (lead-zirconate-titanate) is polarized after firing, transducers are available in various shapes and with various polarisation directions (Fig. 3.4).

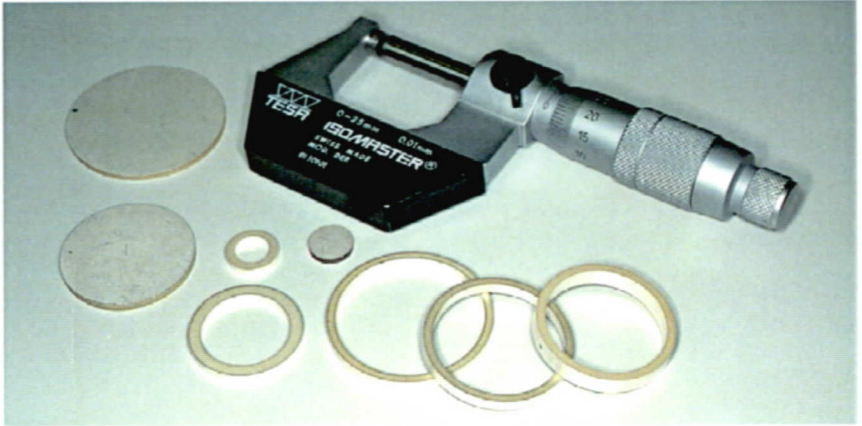


Fig. 3.4 Piezoelectric transducers, discs for longitudinal excitation, rings for radial excitation.

Fig. 3.5 shows the cross-section of a tube and the attached piezoelectric ring transducer.

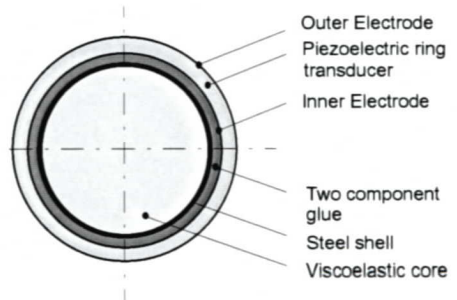
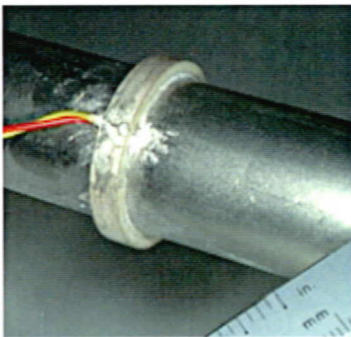


Fig. 3.5 Steel tube with piezoelectric ring transducer acting in radial direction.

For the excitation of axisymmetric waves in an aluminium rod (Fig. 3.6), the best signals are achieved with a ring- and a disc-shaped transducer attached at one end of the rod, acting simultaneously.

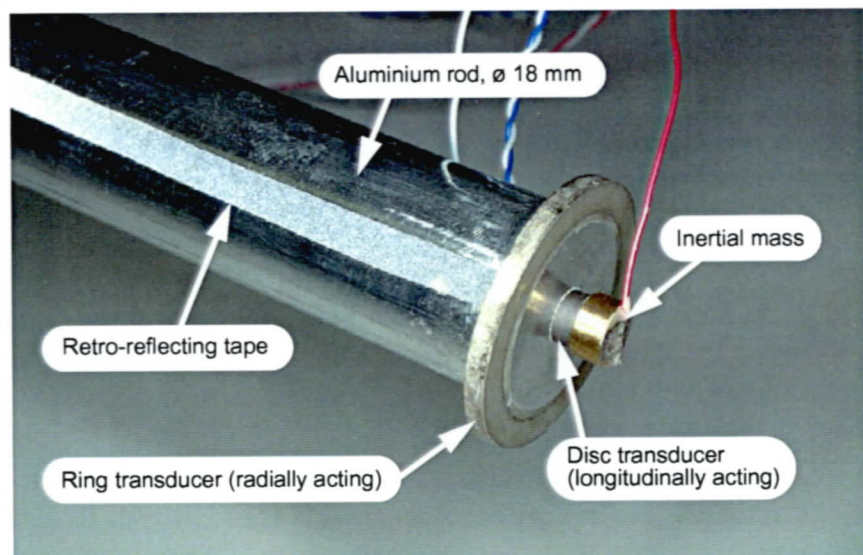


Fig. 3.6 Excitation unit of an aluminium rod with circular-cross section.

A two component glue¹ is used to fasten the transducers² and to fill the gap between the inner electrode and the cylindrical specimen. For further information about piezoelectric excitation, the reader is referred to Dual's dissertation [17], (Appendix B).

1. Hottinger Baldwin Messtechnik, HBM X 60™
2. Ferroperm™ Piezoceramics, Typ PZ 27

3.3 Signal processing

Fig. 3.7 illustrates the digital data processing leading from the displacement measurement to the complex dispersion relation.

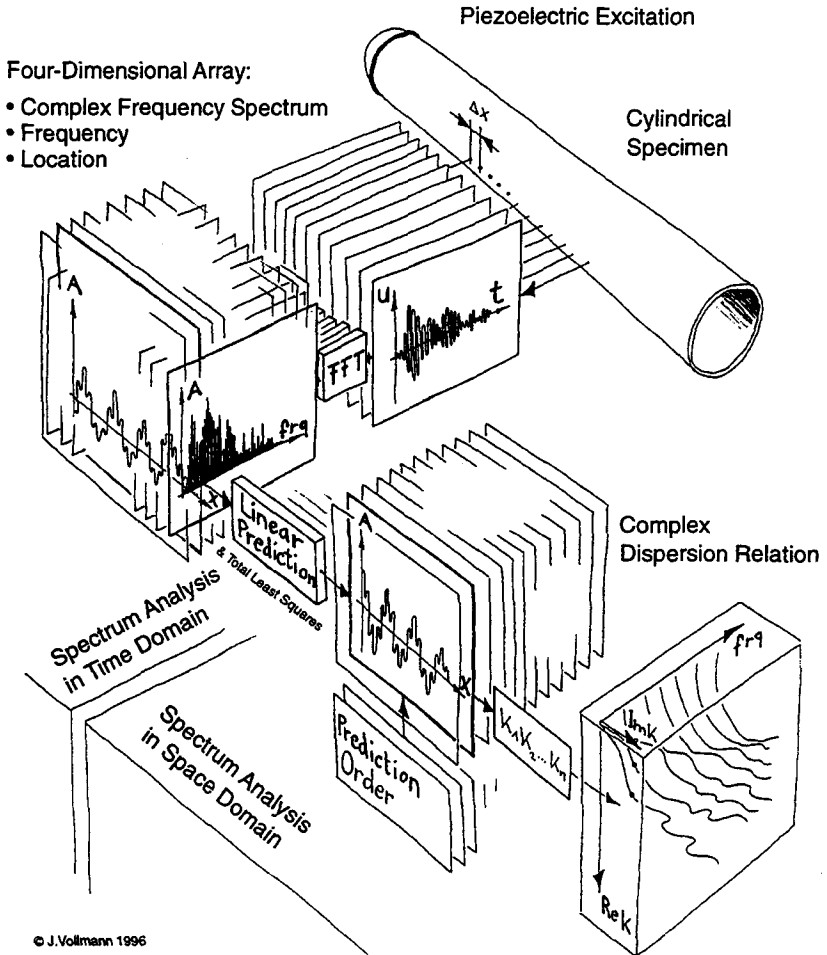


Fig. 3.7 Visualisation of the major steps in signal processing.

3.3.1 Spectrum analysis in time domain

The highly dispersive broad band pulse is propagating to and fro from one end of the tube to the other until its amplitude has decayed below the noise level. The best results are obtained when the whole transient response of the shell to one pulse is recorded to avoid leakage. This demand is, however, a question of storage capacity of the oscilloscope and attenuation characteristics of the structure as well as the frequency range considered. In other words, since the storage capacity of the oscilloscope is limited, one has to balance between a short time window with a high sampling frequency or a long window with a low sampling frequency to achieve good measurement over a wide frequency range. Therefore moderately damped systems are more suitable for broad band frequency measurement than systems with low damping, even though the situation of those systems can be improved by windowing.

Typical values for measurements with an upper frequency limit of 1 MHz and a storage capacity of $n_t = 8192$ samples lead to a frequency resolution of approximately 250 Hz according to Eq. (3.2). (1 MHz signal frequency demands a sampling frequency of at least 2 MHz, thus $\Delta t_{\text{sample}} \leq 0.5 \mu\text{s}$).

$$\Delta f = \frac{1}{n_t \Delta t_{\text{sample}}} = 244 \text{ Hz} \quad (3.2)$$

3.3.2 Spectrum analysis in space domain

Sampling the displacement function versus time is an easy task since it is done automatically by the digital storage oscilloscope. To sample the displacement function along the shell, the LASER interferometer is moved from one point to another by a computer-controlled stepping motor.

According to Eq. (3.3), applying FFT in the space domain would require at least $n_s = 800$ samples along the shell to achieve a wavenumber resolution of 10 rad/m for a given upper wavenumber limit of 4000 rad/m ($\Delta x_{\text{sample}} = 0.79 \text{ mm}$). A wavenumber resolution of 10 rad/m represents a relative resolution which is still 10 times lower than the relative resolution in the frequency range, but it is sufficient to obtain good results for the

systems considered in this investigation.

$$\Delta k = \frac{2\pi}{n_s \Delta x_{\text{sample}}} = 10 \text{ rad/m} \quad (3.3)$$

To circumvent the onerous task of recording a minimum of 800 samples in the space domain, a spectrum estimation method is implemented rather than FFT. The general concept for these types of methods dates back to 1795 when Prony¹ [36] presented a procedure to express an arbitrary function in terms of a linear combination of exponential functions.

The condition that the shortest wave length of interest must be sampled at at least two points, thus determining the distance between two consecutive measurements in the space domain, remains indispensable.

As illustrated in Fig. 3.7, the spectrum estimation method is applied for each frequency given by the discrete Fourier Transform. It consists of two major steps:

Firstly the discrete frequency spectrum versus location (for one particular frequency) can be expressed in terms of exponential functions [see Eq. (3.5)]. This step is called 'Linear Prediction' (LP).

Since the values of the frequency spectrum are available at discrete locations only, where the amplitude versus time function is measured, the location x is described in terms z and Δx_{sample} :

$$x = z \Delta x_{\text{sample}} \quad (3.4)$$

in which z indicates the sampling index along the shell ($z = 0, 1, 2, \dots, N-1$).

$$A(z) \approx C_1 \mu_1^z + C_2 \mu_2^z + \dots + C_n \mu_n^z \quad (3.5)$$

$A(z)$ represents the value of the frequency spectrum at the location z for one particular frequency, and $\mu_i = e^{k_i \Delta x_{\text{sample}}}$. C_i and k_i are to be deter-

1. Riche, Gaspard-Clair-François-Marie, Baron de **Prony**, 1755-1839. French mathematician and engineer. Director of cadastral survey (1791); as inspector general of bridges and roads (1805-39), responsible for all civil engineering projects, such as harbour improvements, drainage of Pontine marshes, and straightening course of Po River; invented a friction brake (1821).

mined.

The linear prediction procedure is outlined below according to Hildebrand [37]. For an autoregressive notation of a similar procedure which reaches the same goal, the reader is referred to Marple [38].

$$\begin{aligned}
 C_1 + C_2 + \dots + C_n &= A(z = 0) \\
 C_1\mu_1 + C_2\mu_2 + \dots + C_n\mu_n &= A(z = 1) \\
 C_1\mu_1^2 + C_2\mu_2^2 + \dots + C_n\mu_n^2 &= A(z = 2) \\
 &\dots\dots\dots = \dots \\
 C_1\mu_1^{N-1} + C_2\mu_2^{N-1} + \dots + C_n\mu_n^{N-1} &= A(z = N - 1) \tag{3.6}
 \end{aligned}$$

Since C_i and μ_i are unknowns, at least $N = 2n$ equations are needed, in principle, to solve the system presented in Eq. (3.6).

Further steps must be introduced to solve this highly nonlinear system. Let μ_1, \dots, μ_n be roots of Eq. (3.7):

$$\mu^n + \alpha_1\mu^{n-1} + \alpha_2\mu^{n-2} + \dots + \alpha_{n-1}\mu + \alpha_n = 0 \tag{3.7}$$

To determine the coefficients $\alpha_1, \dots, \alpha_n$, the first equation of Eq. (3.6) is multiplied by α_n , the second by α_{n-1}, \dots , the n th by α_1 , and the $(n+1)$ th by 1. All equations obtained in this manner are added. The fact that each μ satisfies Eq. (3.7) allows the result to be written in the following form:

$$A_n + \alpha_1 A_{n-1} + \dots + \alpha_n A_0 = 0 \tag{3.8}$$

in which $A_n = A(z=n)$. A set of $N-n-1$ additional equations can be obtained in the same way by starting successively with the second, third, ..., $(N-n)$ th equation leading to the linear system shown in Eq. (3.9).

$$\begin{aligned}
 A_n + A_{n-1}\alpha_1 + A_{n-2}\alpha_2 + \dots + A_0\alpha_n &= 0 \\
 A_{n+1} + A_n\alpha_1 + A_{n-1}\alpha_2 + \dots + A_1\alpha_n &= 0 \\
 \dots\dots\dots &= \dots \\
 A_{N-1} + A_{N-2}\alpha_1 + A_{N-3}\alpha_2 + \dots + A_{N-n-1}\alpha_n &= 0 \tag{3.9}
 \end{aligned}$$

Eq. (3.9) can be written in matrix form:

$$A\alpha = b \tag{3.10}$$

For $N = 2n$, the matrix A has full rank and the linear system [Eq. (3.10)] has a unique solution α , which can be directly calculated by inversion of the matrix A . The values of μ_i are then obtained as roots of Eq. (3.7). With the known values of μ_i , the system of Eq. (3.6) becomes linear, which allows C_i to be determined. The 'beauty' of this method introduced by Prony lies in the fact that the nonlinearity of the problem, which is caused by the exponential approximation, is concentrated in Eq. (3.7), which can be easily solved numerically.

The procedure described up to this point is called 'Forward Linear Prediction' (FLP).

Provided that the values of A_i consist of exponential components caused by propagating waves only, the problem would already be solved by the procedure described above. The number of required samples N would then be two times the number of expected modes m , since C_i and μ_i must be determined and the number of expected modes m would equal the polynomial order n .

In reality, however, the situation is more complicated, demanding a second major step. The signals of interest are hidden in noise and many more samples than $2n$ are needed. Moreover, various non-axisymmetric wave modes are also excited and therefore the number of expected modes m (prediction order) is not known a priori. In this context, some questions arise. What polynomial order n , as a function of the number of samples N , should be chosen for the polynomial introduced in Eq. (3.5)? Two cases shall be discussed:

- $n = m$ and $N > 2n$. In this case, the linear system introduced in Eq. (3.10) is overdetermined and can be solved by standard least squares methods. This approach has no spare parameters to 'describe' the noise and is therefore not providing optimal results by means of distinguishing harmonic components from surrounding noise.
- $n > m$ and $N > 2m$. Here the linear system of Eq. (3.10) might become underdetermined and an infinite number of solutions exist. The pseudoinverse $A^\#$ of the matrix A provides a unique solution having minimum norm, which means that the sum of the squares of all entries in $AA^\# - I$, in which I is an identity matrix, is minimized.

$$\underline{\alpha} = A^\# \underline{b} \quad (3.11)$$

For the signals analysed in this investigation, a polynomial order n , which is higher than the number of expected modes m , is seen to provide better results. Tufts and Kumaresan [39] suggest a polynomial order of $n = 3N/4$ to achieve best accuracy in the determination of the wavenumbers. This result was obtained by analysing synthetic data consisting of two exponential functions and noise. It is also verified by the author of this thesis for four signal components (sinusoids) with noise and is thus adapted for the signal processing of this investigation. The author would like to remark, however, that the optimal polynomial order could depend on the actual signal-to-noise configuration and therefore demands further investigation.

At this point the measured signals consisting of the harmonic components of interest and the noise are described by a parametric model. The next step is the separation of the harmonic components from the noise, a task which is integrated into the calculation process of the pseudoinverse of A . By applying singular value decomposition, the matrix A can be written in the following form:

$$A = U^H \Sigma V \quad (3.12)$$

in which U^H denotes the Hermitian transpose¹ of the matrix U . Both, U

1. The Hermitian transpose, x^H , is the complex conjugate of the transpose of x .

and V are row orthonormal matrices. Σ is a diagonal matrix containing the singular values σ_i of the matrix A .

The pseudoinverse of A is defined in terms of U , Σ , and V as follows:

$$A^\# = V^T \Sigma^{-1} U \quad (3.13)$$

But before this pseudoinversion is carried out, the singular values σ_i are monitored. High values of σ_i are associated with the harmonic components of interest, whereas 'small' values of σ_i are associated with noise and are therefore set to zero. The corresponding columns in V and U are also set to zero, leading to V_q and U_q . In order to realize the quality of the series of measurements, the decision as to what a 'small' singular value means is made in an interactive way for all measurements presented in this thesis, thus determining the prediction order m . With the m remaining singular values, a new matrix $\widehat{\Sigma}$ containing 'less noise' is rebuilt.

$$\widehat{A}^\# = V_q^T \widehat{\Sigma}^{-1} U_q \quad (3.14)$$

And finally, Eq. (3.11) is solved with the improved pseudoinverse $\widehat{A}^\#$.

The procedure described up to this point is called 'Singular Value Decomposition (SVD) of the Data Matrix A '. It provides already very good results when applied to the decomposition of the wavenumbers from the data sets treated in this dissertation.

Further improvements are achieved by applying the method of 'Total Least Squares' (TLS). The main ideas of this method are outlined below: In a classical linear least squares problem, as presented in Eq. (3.15), a linear mathematical model is intended to fit to given (measured) data $\underline{b} + \underline{\varepsilon}$.

$$A\underline{\alpha} = \underline{b} + \underline{\varepsilon} \quad (3.15)$$

Thus, the random errors $\underline{\varepsilon}$ are confined to the right hand side, the 'observation side', of Eq. (3.15). The problem of an exponential approximation is not a linear least squares problem, but it is reduced to one by the linear prediction procedure. Therefore Eq. (3.10) cannot be discussed in terms

of a 'mathematical model' on the left-hand side and an 'observation vector' on the right-hand side. When analysing real measurements, both sides contain 'model' and 'noisy observation' features and a more appropriate version of Eq. (3.10) should be written as shown in Eq. (3.16).

$$(A + E) \underline{\alpha} = \underline{b} + \underline{\varepsilon} \quad (3.16)$$

in which E and $\underline{\varepsilon}$ represent random errors (noise).

The total least squares method provides a solution $\underline{\alpha}$ of Eq. (3.16) while fulfilling the following condition [Eq. (3.17)] in order to minimize influence of the errors on $\underline{\alpha}$.

$$\text{minimize}_{\underline{\varepsilon}, E} \| [\underline{\varepsilon}, E] \|_F \quad (3.17)$$

in which $[\underline{\varepsilon}, E]$ denotes an augmented matrix¹. $\|\bullet\|_F$ denotes the Frobenius² norm. The Frobenius norm of a $m \times n$ matrix M is defined by:

$$\|M\|_F = \sqrt{\sum_{i=1}^m \sum_{j=1}^n m_{ij}^2}$$

If a minimizing pair $[\underline{\varepsilon}, E]$ is found, then any $\underline{\alpha}$ satisfying Eq. (3.16) is said to solve the total least squares problem.

The total least squares problem has been analysed in terms of the singular value decomposition by Golub and Van Loan [33] in 1980.

To evaluate the prediction order, singular value decomposition is applied to the augmented matrix C .

$$C = [\underline{b}, A] = U \Sigma V^H \quad (3.18)$$

-
1. Signifies a matrix the elements of which are the coefficients of a set of simultaneous linear equations with the terms of the equations entered in an added column.
 2. **Frobenius**, Ferdinand Georg, 1849-1917. German mathematician. Professor at the Eidgenössische Polytechnikum, Zürich (1875) and at the Univ. of Berlin (1892).

To be entirely correct, the evaluation of the prediction order m (number of singular values of C which are considered to carry information about the harmonic components) should be made for all frequencies given by the FFT (see Fig. 3.7). But since the FFT provides thousands of samples, the prediction order is evaluated in a pre-process for a selection of frequencies only which are distributed over the whole frequency range by applying singular value decomposition of C in an interactive way. Since the polynomial order is kept constant at $n = 3N/4$, a wrong prediction order scarcely affects the accuracy of the decomposition, but it leads to either modes being omitted or noise being interpreted as a harmonic component, which results in an additional dot on the dispersion diagram.

Then the whole frequency range is subdivided into coherent intervals of constant prediction order (within an interval) to be finally decomposed for each frequency. Therefore the vector $\underline{\alpha}$ [see Eq. (3.16)] is calculated according to Tirendi and Martin [32].

A complete understanding of this procedure would demand several further steps; however, for brevity, the results only are presented below: From V , the matrix V_2 is formed out of the $(m+1)$ th to the $(n+1)$ th column v_j :

$$V_2 = [v_{m+1} \dots v_{n+1}] \quad (3.19)$$

$(v_j)_1$ is the j th element in the first row of V_2 and v'_j is the vector formed by the remaining elements of the j th column [see Eq. (3.20)].

$$v'_j = \begin{bmatrix} (v_j)_1 \\ v'_j \end{bmatrix} \quad (3.20)$$

The vector $\underline{\alpha}$ can now be calculated as:

$$\underline{\alpha} = \sum_{j=m+1}^{n+1} \left[\frac{(v_j)_1^*}{\sum_{i=m+1}^{n+1} |(v_i)_1|^2} \right] v'_j \quad (3.21)$$

in which $(v_i)_1^*$ represents the complex conjugate of $(v_i)_1$.

Now the coefficients $\alpha_1, \dots, \alpha_n$ are known and the values μ_p are the roots of Eq. (3.7). With the values μ_i , Eq. (3.6) becomes a linear system for C_i and the complex wavenumbers k_i can be determined.

3.3.3 Confidence and accuracy

A two-dimensional spectrum analysis consisting of FFT for the decomposition of the frequencies, and a combination of linear prediction and total least squares for the decomposition of the wavenumbers of propagating wave modes, enables the simultaneous measurement of a considerable number of dispersion curves in the space defined by frequency and complex wavenumber. The following questions concerning the reliability and accuracy of this new method may arise:

- 1) Is the method free of systematic errors which reach a level that they could affect the accuracy of the determination of material properties? In statistical terms, is the method biased¹, unbiased, or asymptotically unbiased?
- 2) How do random errors of the input data propagate through the decomposition process?
- 3) What is the lowest signal-to-noise ratio (SNR), the so-called 'threshold', at which the method provides reasonable results?
- 4) How does the prediction order m affect the accuracy of the decomposed signals?

Since spectral estimation methods are generally new, and are applied in this thesis particularly to parameter ranges where other methods failed to work, some of the questions above cannot yet be answered on a quantitative basis and require further investigation.

Evidence that the method appears to be free of systematic errors, however, is given by dispersion curves which are governed by one or two

1. Bias: Systematic deviation of a statistical estimate from the quantity it estimates.

material properties which are very well-known, as presented in the following chapters. In other words, wherever the method could be verified, it showed perfect agreement with other methods and therefore appears to be unbiased.

Each spectrum analysis (in time or space domain) is an independent process (see Fig. 3.7), and random errors of the input quantities and the process itself are therefore directly visible in the dispersion diagram. The better the dots of the single measurements 'line up' to a continuous graph, the lower the influence of random errors.

For a detailed analysis of the total least squares method, especially of its statistical and sensitivity properties, the reader is referred to the work of Sabine Van Huffel [40].

Another feature, quantifying the quality of a spectrum estimation method, is the lowest signal-to-noise ratio (threshold) for which the method provides reasonable results. The signal-to-noise ratio is defined as follows:

$$\text{SNR} = 10 \log_{10} \left(\frac{a^2}{2\sigma_n^2} \right) \quad (3.22)$$

in which a represents the amplitude of the signal and σ the variance of the complex Gaussian white noise. The method applied in this thesis (linear prediction and total least squares) provides reasonable results down to a SNR level of 7 dB, which means that the amplitude of the signals amounts to 3.17 times the variance of the surrounding noise. A numerical analysis of the accuracy of several methods, based on singular value decomposition as a function of the SNR, is given by Uike et al.[31].

An analysis of the influence of the polynomial order n and the prediction order m on the detectability and the accuracy of the signals is given by Tufts and Kumaresan [39].

4 Experimental results versus theory

Numerous combinations of shells and 'fluids' like water, milk, alcohol, glycerine, silicone oil, and polyisobutylene are investigated in this project. An extract of these experimental results outlining the main aspects and phenomena will be presented here. The shell remains unchanged by means of geometry and material. A steel tube with a diameter of 26 mm, a wall thickness of 0.5 mm, and a length of 1 or 2 m is used to perform the experiments.

To verify the theoretical model derived in Chapter 2, as well as the numerical accuracy of the root-finding algorithm in the parameter range of strong shear elasticity, dispersion curves of axisymmetric waves in an isotropic aluminium rod with a diameter of 18 mm are also measured and compared with the numerical results.

4.1 The empty shell

The properties of the shell material are determined by the longitudinal mode in an empty shell which is excited with a longitudinally-acting piezo transducer at one end.

The best fit for the longitudinal mode and for the coupling area is achieved with the following parameters:

Young's modulus	$E =$	$2.000 \cdot 10^{11}$	N/m ²
Poisson's ration	$\nu =$	0.28	
Density	$\rho =$	7800	kg/m ³ .

A value of $\kappa = 0.8$ is chosen from [23] for the shear correction factor. The corresponding theoretical model is presented in Chapter 2.

In Fig. 4.1 the experimental and the theoretical curves are compared, showing perfect agreement for the longitudinal mode and for the coupling area.

The slight difference for the flexural mode is probably caused either by a boundary layer of air diminishing its wavespeed, an effect which is not considered in this calculation, or by a non-optimal value for κ .

The difference could also be caused by a slight elastic anisotropy of the tube.

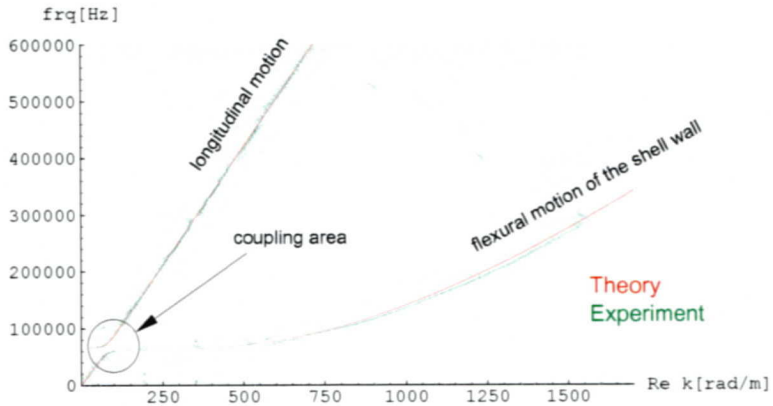


Fig. 4.1 Measured dispersion curves versus calculated curves of axisymmetric wave modes (excluding the torsional mode) in an empty shell with a diameter of 26 mm and a wall thickness of 0.5 mm.

4.2 The shell filled with silicone oil in low frequency range

One of the first series of measurements was performed on a silicone oil (Dow Corning[®] 200 Fluid) with a density of 969.0 kg/m^3 and a nominal viscosity of $60000 \text{ mm}^2/\text{s}$ which means that the viscosity equals roughly 60000 times the value of water at 20°C . The primary question was whether the dynamic behaviour of the silicone core could be at all described by the viscoelastic models introduced in Section 2.3 and if so, whether it could be classified (more or less) as an inviscid, a dissipative, or a shear elastic core.

At the time these curves were measured, a commercial frequency demodulator, limiting the frequency range to $\approx 300 \text{ kHz}$, was used.

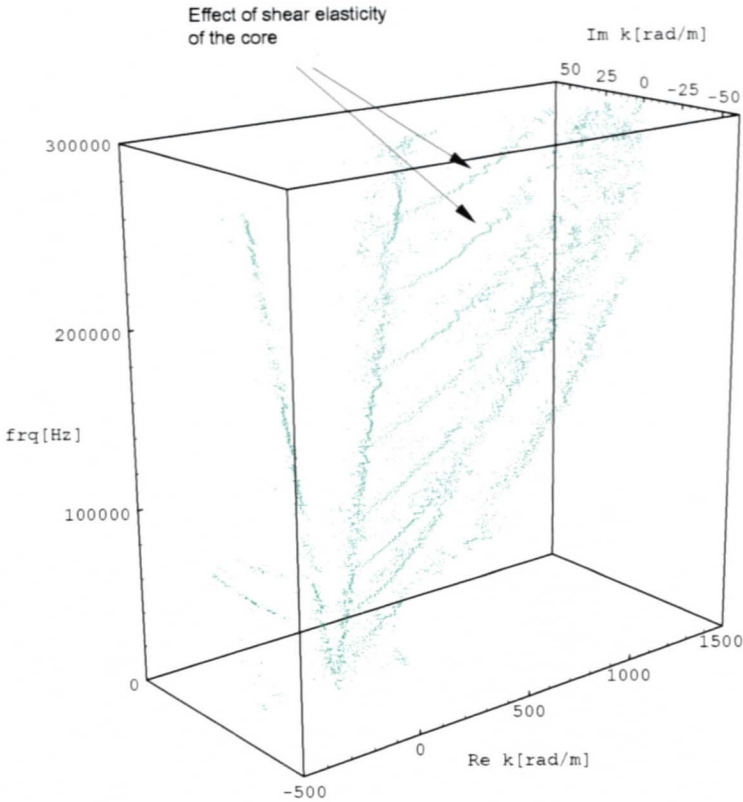


Fig. 4.2 Measured dispersion curves of the first 9 axisymmetric wave modes in a cylindrical shell filled with silicone oil with a nominal viscosity of $60000 \text{ mm}^2/\text{s}$; temperature: $24.1 \text{ }^\circ\text{C}$.

In reference to the diagram in Fig. 4.2 and its projection into the real plane in Fig. 4.3, two features should be emphasized. The curves in the half space of positive real wavenumbers represent outgoing waves from the piezoelectric excitation. The strong damping caused by the highly viscous oil leads to the fact that little information is received from the reflected waves propagating towards the excitation. The steep parts of the dispersion curves are associated with the longitudinal motion of the shell. Since

the density of the shell equals approximately eight times the density of the fluid, the interaction is relatively weak along these parts of the curves, and reflected signals can therefore be clearly identified.

Another feature (indicated by the arrow in Fig. 4.2) can be observed regarding the two highest modes. Here the curves tend to leave the plane defined by frequency and real wavenumber periodically. According to Section 2.3.5, such behaviour is also visible in theoretical results when the shear elasticity of the viscoelastic core is increased. This effect is small, however, when compared to the sensitivity of the system to changes in the velocity of P-waves in the core. Therefore the experimental data of Fig. 4.3 were used to determine a first set of parameters for an inviscid core.

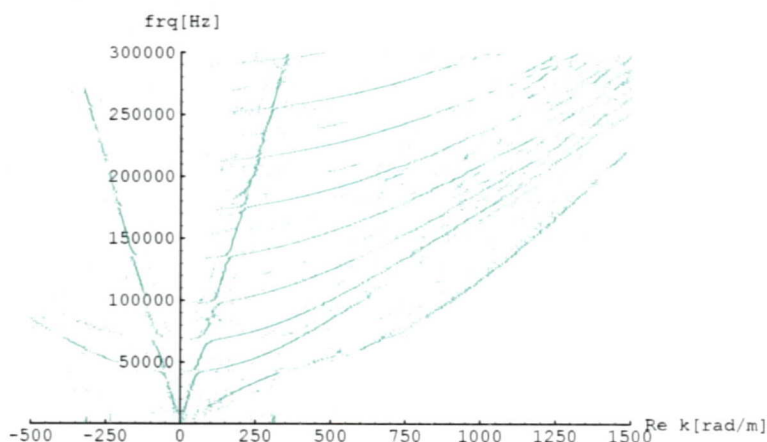


Fig. 4.3 Projection of the curves presented in Fig. 4.2 into the real plane.

4.3 The shell filled with silicone oil in high frequency range

An improved phase demodulator enables one to measure up to 2 MHz. The validity of the core parameters determined below 300 kHz can now be verified in a higher frequency range. Fig. 4.4 shows experimental dispersion curves for the same shell-core configuration (silicone oil with a density of 969.0 kg/m^3 and a nominal viscosity of $60000 \text{ mm}^2/\text{s}$).

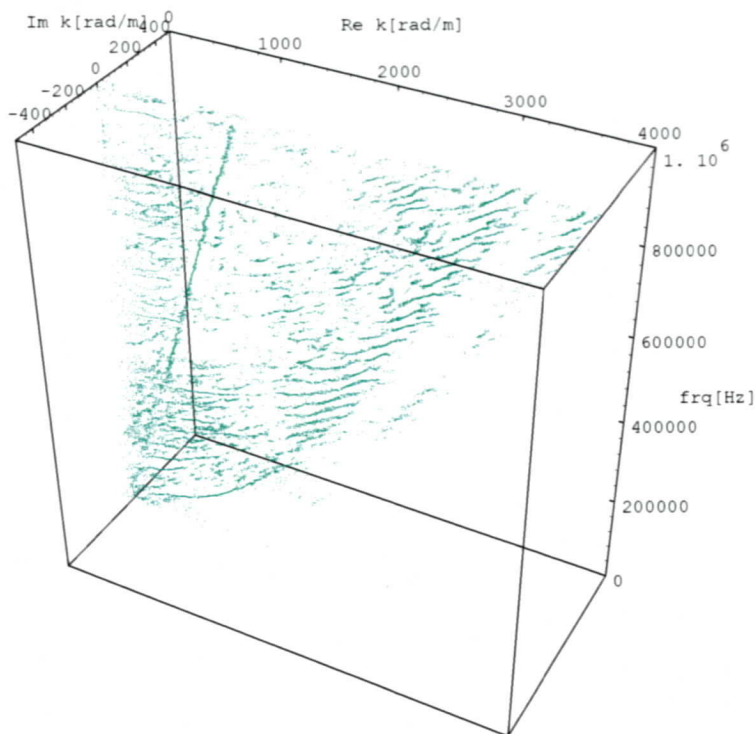


Fig. 4.4 Measured dispersion curves of the first 25 axisymmetric wave modes in a cylindrical shell filled with silicone oil with a nominal viscosity of $60000 \text{ mm}^2/\text{s}$; temperature: $24.0 \text{ }^\circ\text{C}$.

Even at an upper frequency which is more than three times the upper frequency of the first series of experiments, the inviscid core model still fits quite well (see Fig. 4.4 and Fig. 4.5). Thus the relation between real wavenumber and frequency is obviously governed primarily by the velocity of P-waves c_p in the core.

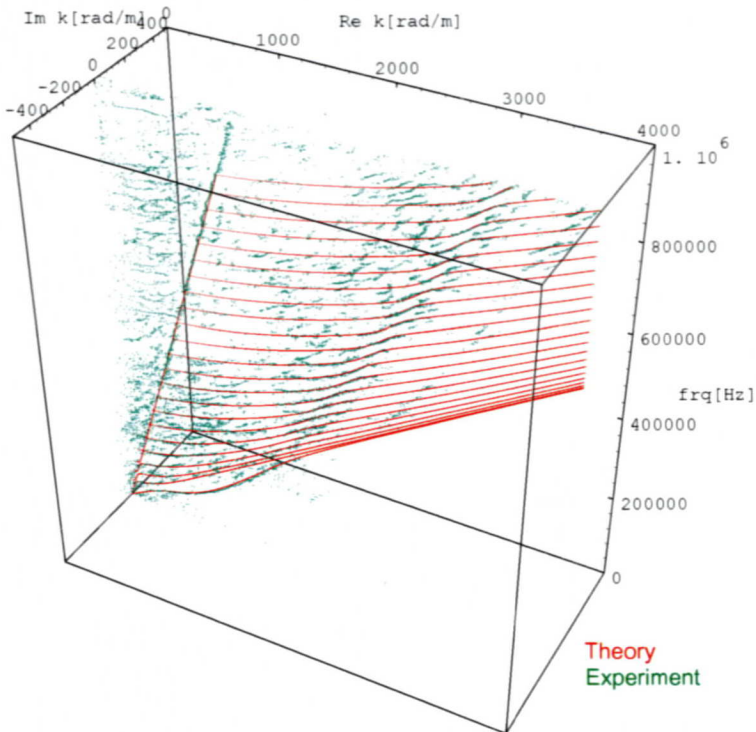


Fig. 4.5 Superposition of the measured dispersion curves of the first 25 axisymmetric wave modes in a cylindrical shell filled with silicone oil with a nominal viscosity of $60\,000 \text{ mm}^2/\text{s}$ and theoretical results for a shell filled with an inviscid core material having the same velocity of P-waves c_p as silicone oil.

By viewing the data presented in Fig. 4.4 from a different angle and blowing up the scaling of the imaginary axis, one can visualize the periodically

alternating values of the imaginary parts of some dispersion curves. This effect may appear meagre, nevertheless, it is clear evidence for the shear elastic behaviour of the silicone core, as the comparison between Fig. 4.6 and Fig. 4.7 shows.

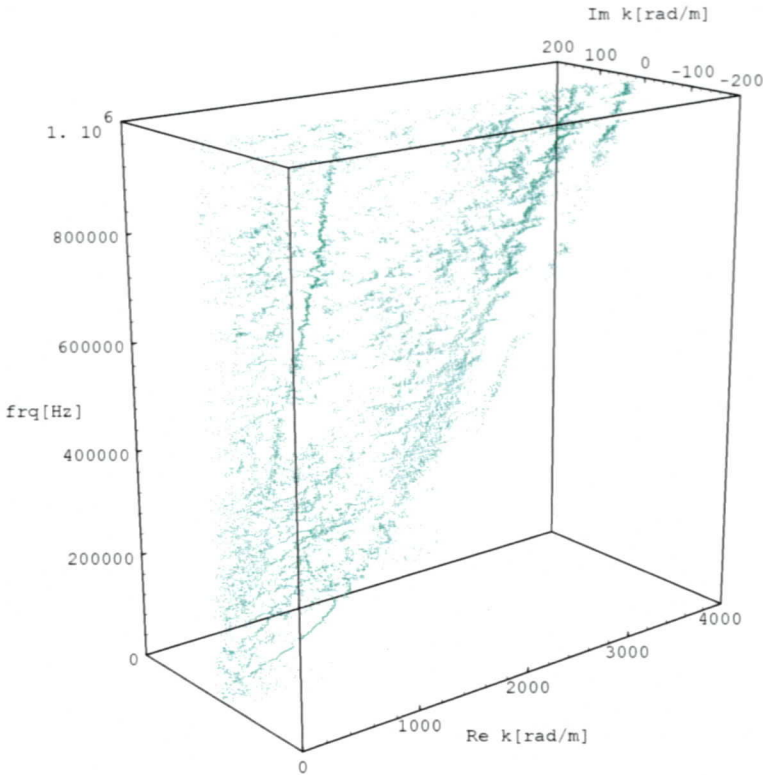


Fig. 4.6 Measured dispersion curves of the first 25 axisymmetric wave modes in a cylindrical shell filled with silicone oil with a nominal viscosity of $60000 \text{ mm}^2/\text{s}$; temperature: $24.0 \text{ }^\circ\text{C}$, scaled to emphasize the effect of shear elasticity.

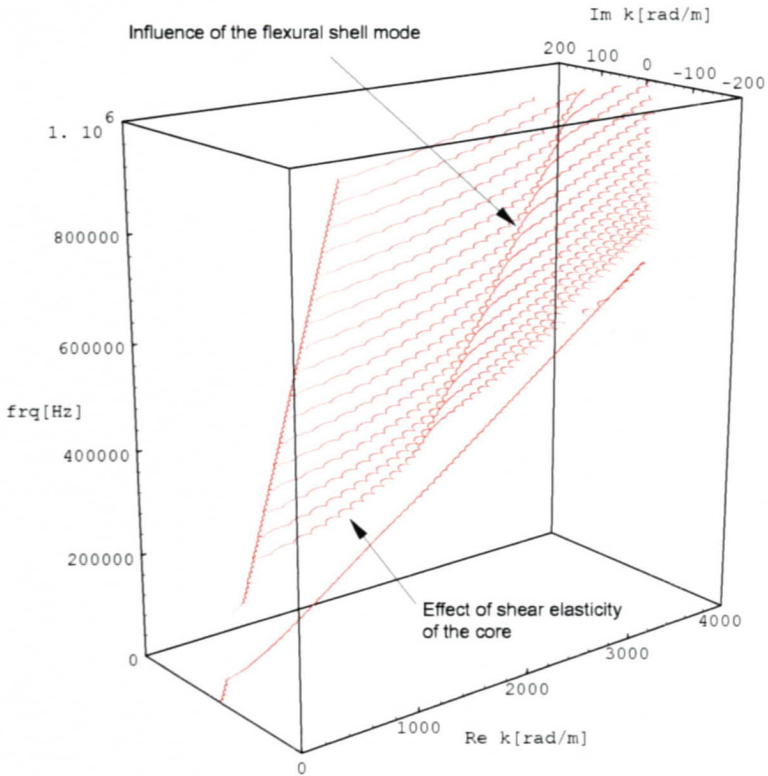


Fig. 4.7 Theoretical dispersion relation of axisymmetric modes of a shell containing a shear elastic core material having the same velocity of P-waves c_e as silicone oil. (Due to numerical reasons, some lower modes could not be calculated.)

The region indicated by the arrow in Fig. 4.7 is connected with the flexural mode of the empty shell (see Fig. 2.14 of Section 2.3.3). The imaginary part of the curves is very small there, a fact which explains the good measurability in that particular range.

4.4 The shell filled with alcohol (low viscosity)

Dispersion curves are also measured for a shell filled with ethyl alcohol (density: 789 kg/m^3 , nominal viscosity: $1.52 \text{ mm}^2/\text{s}$ at 20°C). Since the velocity of P-waves c_p in this fluid is lower than in silicone oil, the wavelength is shorter. Therefore more concentric zones of equal pressure are present in the core at one particular frequency, thus increasing the number of detectable modes as shown in Fig. 4.8.

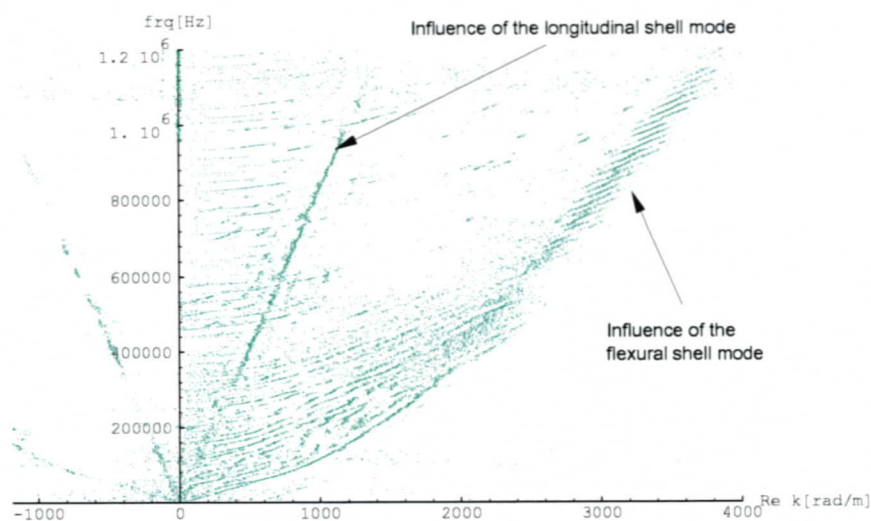


Fig. 4.8 Measured dispersion curves (projection into the real plane) of axisymmetric wave modes in a cylindrical shell containing ethyl alcohol (density: 789 kg/m^3 , nominal viscosity: $1.52 \text{ mm}^2/\text{s}$ at 20°C); temperature: 23.8°C .

Again the curves can only be measured clearly in the region of the flexural mode of the empty shell for frequencies above 500 kHz. It is most likely that the complex spectral estimation method reaches its limits by interpreting the periodically alternating imaginary part of the wavenumber as noise beyond the region mentioned above.

4.5 The shell filled with polyisobutylene (high viscosity)

Not all measured dispersion diagrams can be explained by the theoretical model introduced in Chapter 2. As an example, the data of a shell filled with polyisobutylene (BASF® Opanol™ b 10) are presented below (Fig. 4.9 to Fig. 4.11). Polyisobutylene is a linear, flexible polymer with a glass temperature of -65°C . Above this temperature the material can be considered an amorphous homogeneous melt. According to BASF®, the density of Opanol™ b 10 equals 890 kg/m^3 , the real part of the shear modulus $\text{Re } G^*(f=100\text{ kHz}, t=150^{\circ}\text{C}) \approx 2 \cdot 10^5\text{ N/m}^2$, and the imaginary part $\text{Im } G^*(f=100\text{ kHz}, t=150^{\circ}\text{C}) \approx 2 \cdot 10^5\text{ N/m}^2$.

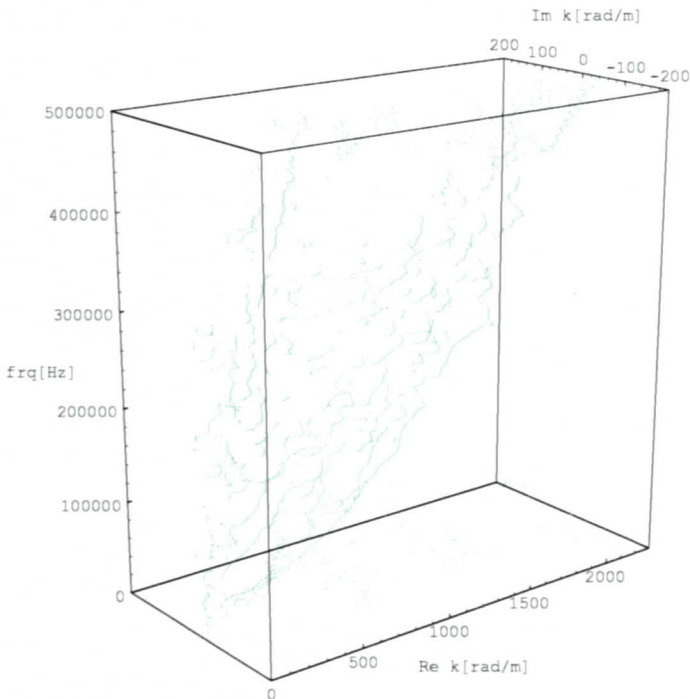


Fig. 4.9 Dispersion curves of axisymmetric waves in a cylindrical shell filled with polyisobutylene (BASF® Opanol™ b 10), measured at 26.0°C .

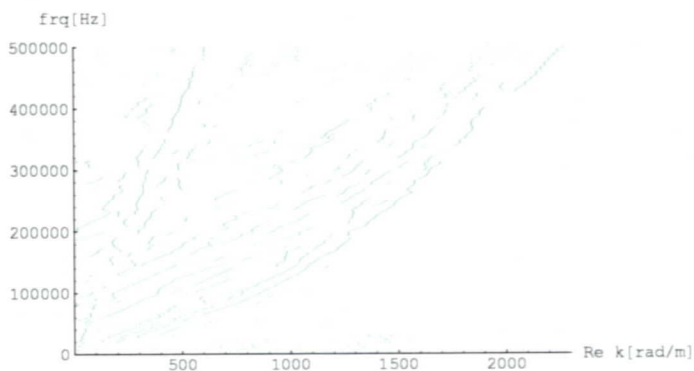


Fig. 4.10 Projection of the curves presented in Fig. 4.9 into the real plane.

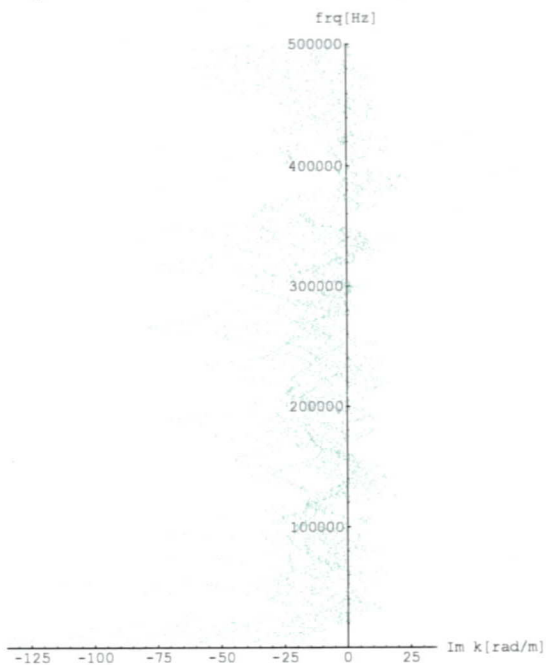


Fig. 4.11 Projection of the curves presented in Fig. 4.9 into the imaginary plane.

4.6 The linear elastic aluminium rod

When considering the 'fluids' which have been investigated, it seems that dispersion curves in the complex space have either a very complicated shape which is barely describable by a theoretical model with a limited number of parameters (Fig. 4.9 to Fig. 4.11), or can be detected only very close to the real plane (Fig. 4.8). An intrinsic requirement of the linear prediction method is that the amplitude of propagating waves needs to be sufficient in order to separate them from surrounding noise. Therefore highly damped modes are difficult to measure.

To the author's knowledge, the mechanical behaviour of fluids subjected to shear forces alternating with high frequency (MHz range) is not yet well-known but a fluid with a well-defined, high shear resistance would be very helpful in order to verify the calculated dispersion curves in this parameter range. This thought led to the following idea:

Linear elasticity can be considered as an extreme case of viscoelasticity having long relaxation times compared with the deformation cycles. To ascertain the validity of the theoretical model as well as the computational precision, especially in the range of strong shear elasticity, the dispersion curves of axisymmetric waves in an aluminium rod with circular cross-section are also measured (Fig. 4.12 and Fig. 4.13). The corresponding dispersion relation is calculated by running the same computer program used for the shell filled with a viscoelastic medium (Fig. 4.14). Therefore the relaxation times for shear and bulk behaviour of the core material are set to high values compared with the reciprocal value of the lowest frequency within the range considered. The thickness of the shell wall h is set to a very small value (10 μm).

Excellent agreement between material constants received in this manner and values determined by other dynamic methods is found, thus confirming the validity of the theoretical model and the numerical procedure.

The diameter of the aluminium rod (ALUSWISS® Anticorodal™ -112-hard) is 18 mm. With a density of 2751.6 kg/m³, a Young's modulus of $7.041 \cdot 10^{10}$ N/m², and a Poisson ratio of 0.35, the best fit with experimental curves is obtained as presented in Fig. 4.15.

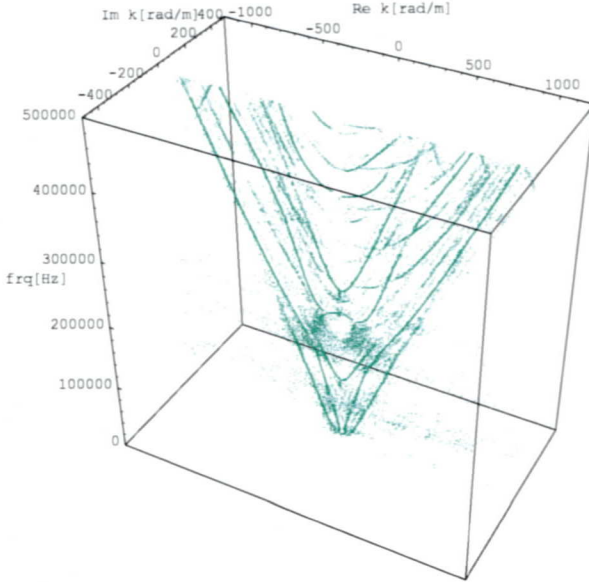


Fig. 4.12 Measured dispersion relation of axisymmetric wave modes of an aluminium rod with circular cross-section (diameter: 18 mm).

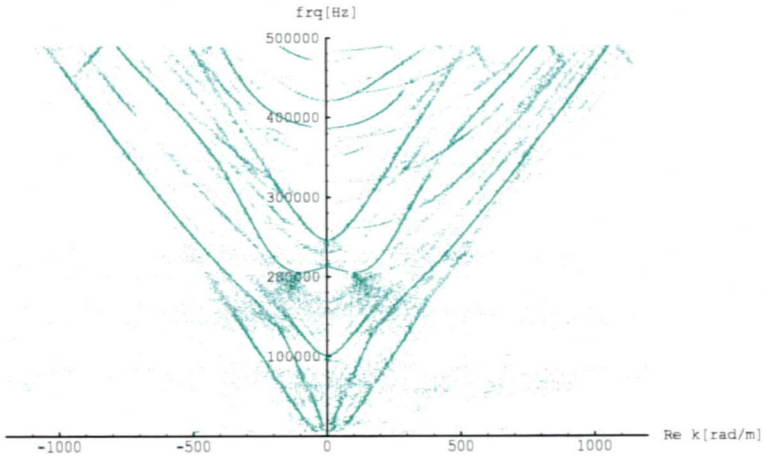


Fig. 4.13 Projection of the curves presented in Fig. 4.12 into the real plane.

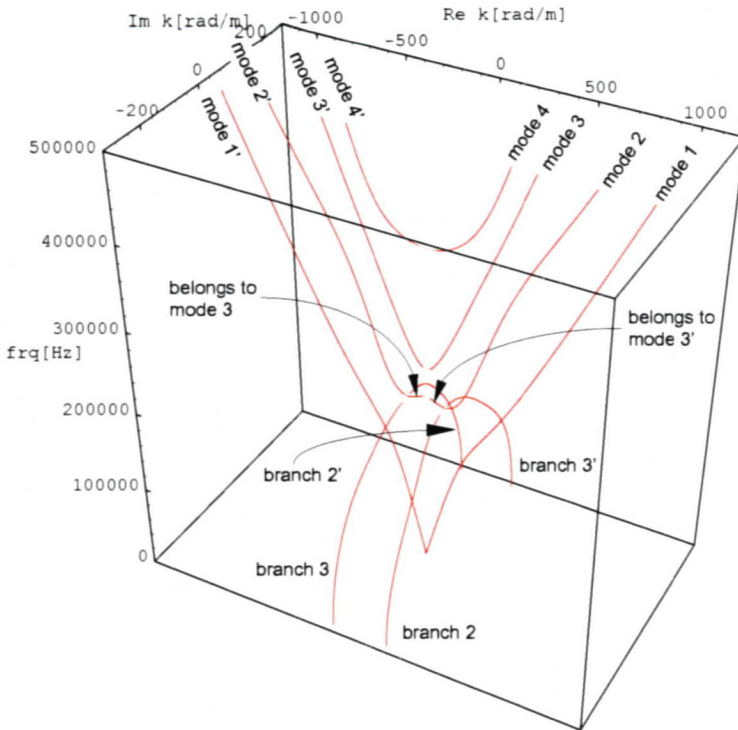


Fig. 4.14 Theoretical dispersion relation of axisymmetric wave modes of an aluminium rod with circular cross-section (diameter: 18 mm). The curves in the imaginary plane are not presented in this diagram.

In Fig. 4.14 the various modes and branches, which will be discussed in the next section, are labelled. Modes and branches with an index followed by an apostrophe are associated with energy reflected from the end of the specimen propagating towards the excitational end. The half-circle shaped curves in the imaginary plane, connecting the upper and lower parts of mode 3 and mode 3', could not be calculated with the present model due to numerical reasons. The reader is therefore referred to Onoe et al. [41] or Achenbach [20].

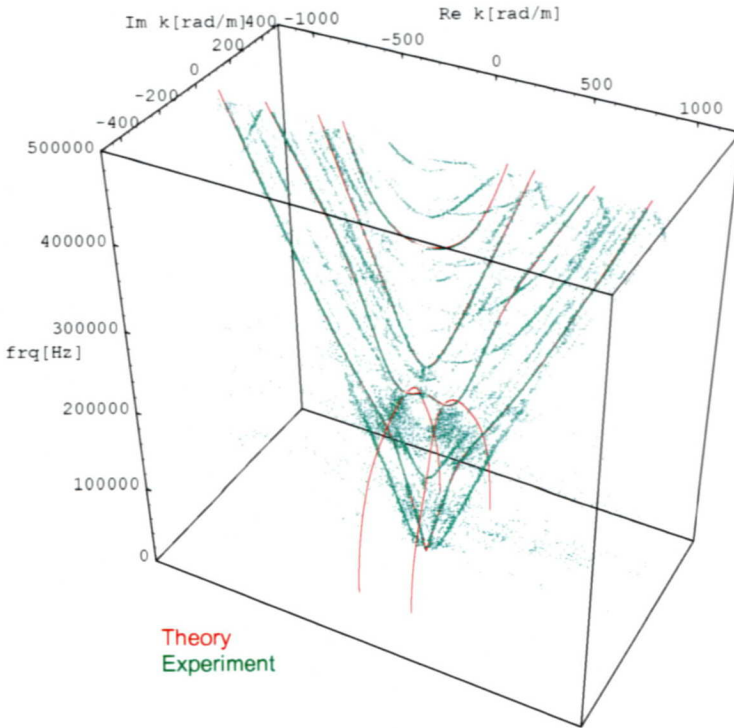


Fig. 4.15 Superposition of the measured dispersion curves of axisymmetric wave modes of an aluminium rod with circular cross-section (diameter: 18 mm) and theoretical dispersion curves.

Fig. 4.15 shows excellent agreement between theoretical and experimental results for all axisymmetric modes in the frequency range of between 1 kHz and 500 kHz. Apart from axisymmetric waves, the dispersion curves of several non-axisymmetric modes are also detected, visible in Fig. 4.15. These modes are always present due to imperfections in the excitation, the structure itself, or the support devices of the specimen.

Fig. 4.16 shows the projection of the theoretical and the experimental curves of Fig. 4.15 into the imaginary wavenumber versus frequency plane.

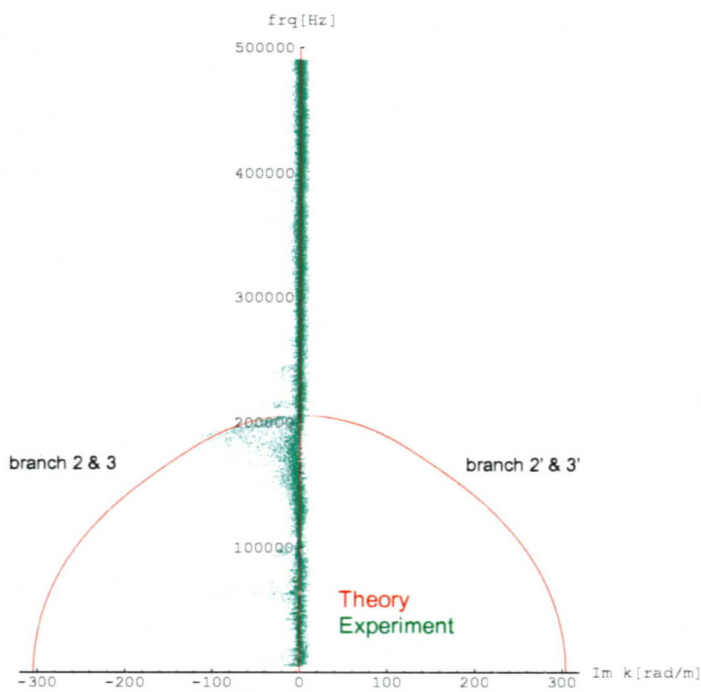


Fig. 4.16 Projection of the curves presented in Fig. 4.15 into the imaginary plane.

4.7 Backward wave propagation and boundary movements

Since the damping of the waves propagating in an aluminium rod is much lower than in a silicone-filled shell, the dispersion curves of waves reflected at the end of the rod, which have negative wavenumbers, are detected as well (see Fig. 4.12 and Fig. 4.13). The fact that energy is propagating in both directions enables the detectability of the phenomenon of 'backward-wave propagation', mentioned by Onoe, McNiven, and Mindlin in 1962 [41], in which group velocity and phase velocity of one particular mode have opposite signs in the range of long wavelength (see Fig. 4.13 and Fig. 4.18). This phenomenon was the subject of extensive discussions in the early 1960s. In order to outline this phenomenon, the group velocity of propagating and decaying or growing waves must be defined.

The group velocity c_g , introduced in Eq. (4.1), represents the velocity of the energy carried by a wave. It is proportional to the slope of the dispersion curves in the frequency-wavenumber diagram.

Group velocity c_g :

$$c_g := \frac{d\omega}{dk} \quad ;$$

Phase velocity c :

$$c = \frac{\omega}{k} \quad (4.1)$$

and since k is complex:

$$c_{gr} = \frac{d\omega dk_r}{dk_r^2 + dk_i^2} \quad ; \quad c_{gi} = \frac{-d\omega dk_i}{dk_r^2 + dk_i^2} \quad (4.2)$$

in which c_{gr} , k_r are real parts and c_{gi} , k_i are imaginary parts of the group velocity and the wavenumber, respectively.

In Fig. 4.17 the theoretical dispersion relation presented in Fig. 4.14 is translated into the complex group velocity versus frequency form.

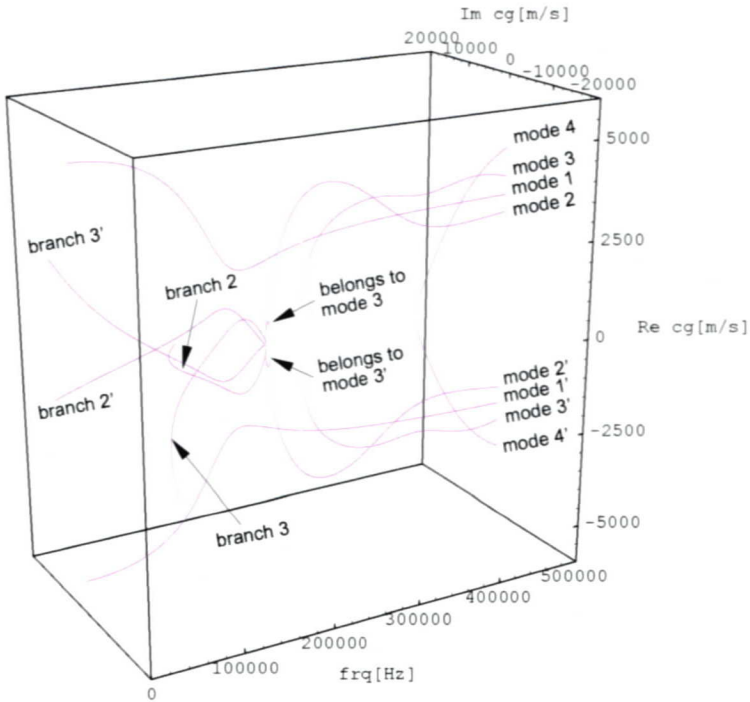


Fig. 4.17 Group velocity representational form of the theoretical dispersion relation of axisymmetric wave modes of an aluminium rod with circular cross-section (diameter: 18 mm).

As Folk [42] explained, the path of a consistent mode, drawn in the wave-number-frequency plane, cannot change the sign of its slope, but in Fig. 4.14 the slopes of mode 2 and mode 2' appear to do so. In actual fact, these modes cease to exist beyond the point where their slopes reach the zero level (point S and S' in Fig. 4.18) since no energy can escape from the excitational piezo transducer once the group velocity has become zero. The four branches (2,3,2',3') leaving the real plane at these points (point S and S' in Fig. 4.18) represent 'boundary movements' existing only very close to the excitational source. Nevertheless, the traces of branch 2 and branch 3 are measured, as visible in Fig. 4.16 and Fig. 4.18, a fact which indicates that these 'boundary movements' are still

propagating but also strongly decaying waves, otherwise they could not be detected. Of the four branches, only branches 2 & 3 are detectable. This is in agreement with the general wave approaches made in Eq. (2.41) and Eq. (2.42), in which a wavenumber with a positive real part and a negative imaginary part indicates a decaying wave, propagating away from the excitation.

The two curves between the points S and S' in Fig. 4.18 show the area of 'backward wave propagation', a name which has obviously been chosen because of the opposite signs of the phase velocity and the group velocity of these curves, according to Eq. (4.1).

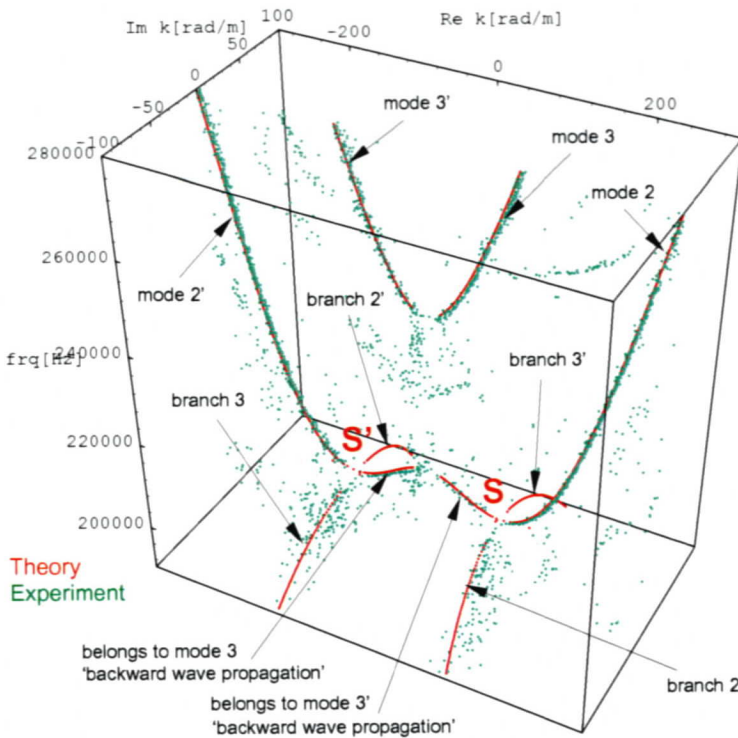


Fig. 4.18 Experimental and theoretical dispersion relation of axisymmetric wave modes of an aluminium rod with circular cross-section, scaled to show the area of 'backward wave propagation'.

Close examination of the 'backward wave propagation' of mode 3 in Fig. 4.18 shows that this curve is more easily detected than the corresponding curve of mode 3'. This is due to the fact that the 'backward wave propagation' of mode 3 represents outgoing waves, coming directly from the excitational source.

The two curves between the points S and S' of Fig. 4.18 become arches in the group velocity versus frequency form, as shown in Fig. 4.19.

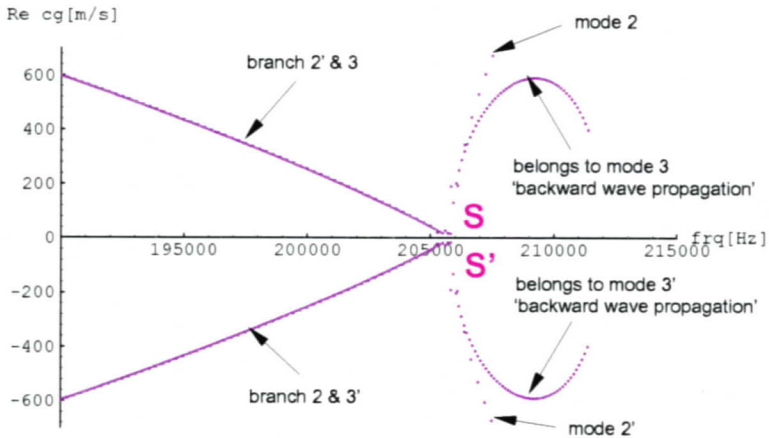


Fig. 4.19 Group velocity representational form of the theoretical dispersion relation of axisymmetric wave modes of an aluminium rod with circular cross-section, scaled to visualize the area of 'backward wave propagation'.

A first attempt to measure 'backward-wave propagation' was undertaken by Meitzler [43] in 1965, and in 1988 Wolf [44] investigated the same phenomenon in plates. However, measuring 'backward wave propagation' by means of gauging time delays of narrow band pulses is an onerous task since the wavelength and therefore the pulses become long compared to the longitudinal dimension of the specimen, impeding a clear detectability of the arriving pulses and thus reducing the quality of the measurement. Mention should be made of the notation used by Wolf et al. [44].

It is misleading to talk about a 'negative group velocity' since such a velocity does not virtually exist and leads to the illusion that one could receive the energy from pulses which would be emitted in the future !

Imagine a specimen of semi-infinite longitudinal extent with the excitational source at the only end. In this case all modes and branches indicated by an apostrophe in Fig. 4.14, Fig. 4.17, Fig. 4.18, and Fig. 4.19 disappear and no negative group velocity can be identified in the real wavenumber versus frequency plane. What becomes negative is the phase velocity of the lower part of mode 3. This means that the crest of the waves of a narrow band pulse flows towards the excitation while the whole pulse propagates away from it in the particular frequency range of 'backward wave propagation'.

When comparing the topology of the dispersion relation of a linear elastic rod (Fig. 4.14) with that of an inviscid fluid column (see Fig. 2.9 of Section 2.3.2), it seems that the appearance of 'backward wave propagation' is connected with shear elasticity of the medium, since it does not occur in the dispersion diagram of the fluid column consisting of an inviscid fluid. Therefore further research efforts should be devoted to the influence of the constitutive parameters on the appearance of this phenomenon.

4.8 Conclusions

A new contactless measurement technique for structural mechanics has been developed by combining modern spectral estimation methods with a high resolution LASER interferometer. Some aspects of dynamic fluid structure interaction in the high frequency range, where fluid behaviour is not well-known, are investigated. The validity of a multiparameter model describing the dynamic behaviour of a thin-walled elastic shell containing various core materials derived in Section 2.2 is verified for several core materials. Since the method is based on propagating waves, the detectability of a mode decreases with increasing damping. A main advantage of the axisymmetry is the fact that the system is mechanically highly decoupled from the surrounding world.

The tools developed in this investigation can be used to explore the topology of the dispersion relation of axisymmetric waves in cylindrical structures. Thus they form a basis for various applications such as the design of fluid sensors or fluid providing systems, the development of non-destructive material and structural testing methods, the inspection of coatings, and so on. If optimal damping of a structure is required, such as for vibration or noise absorbers, this model can be used to specify a material which best fits the purpose for a specific frequency range.

The phenomenon of 'backward wave propagation', in which group velocity and phase velocity have opposite signs, is clearly measured and partly explained on a heuristic base. The 'boundary movements' which are connected with the phenomenon of 'backward wave propagation' are also detected and explained on a heuristic basis.

Future work at the Institute of Mechanics, ETH Zürich, deals with the extension of complex spectrum estimation methods to more than one dimension, as well as with the improvement of the signal-to-noise ratio, with the aim to increase the detectability of attenuating waves.

The measurement technique is used for determining complex material properties of anisotropic materials, which is presented in Chapter 5 of this thesis.

5 Complete elastic characterization of anisotropic material by guided waves

5.1 Motivation

The growing application of composite materials demands reliable, nondestructive testing methods in order to evaluate the mechanical behaviour of new composite materials, as well as for the in-situ inspection of existing structures.

In this chapter the experimental methods described in Chapter 3 are applied for the complete elastic characterization of a transversely isotropic rod with circular cross-section in a frequency range of between 1 kHz to 1 MHz. Transverse isotropy is one of the simplest cases of anisotropy in which the stiffness of the material differs in only one direction. The rod consists of carbon fibres embedded in an epoxy matrix parallel to the longitudinal axes of the rod and has a diameter of 11 mm.

Homogenizing the composition of the two components (fibres and epoxy matrix) which differ strongly in stiffness, the elastic behaviour of the composite material is described by a constitutive equation consisting of five constants. Provided that the wavelength of the guided structural waves remain 'long' compared with the characteristic length of the inhomogeneity caused by the fibres, the analysis of wave propagation phenomena is an excellent - not to say the only - way to investigate the elastic behaviour of such structures. Thus the dispersion relation of higher axisymmetric wave modes, including the torsional modes, has been used to determine the five material constants.

Based on a theoretical model introduced by Mirsky [15] in 1965, a computer program, similar to the program for the fluid-filled shells treated in Chapter 2, has been written to calculate the dispersion relation of axisymmetric waves. The numerical variation of the elastic constants as well as the analysis of various mode shapes led step by step to the determination of the real parts of the material constants. As the imaginary wavenumbers are measured as well, the frequency dependent damping behaviour of the composite material is also discussed on a qualitative basis.

5.2 Derivation of the dispersion relation of axisymmetric wave modes in a transversely isotropic rod

5.2.1 Constitutive equation of anisotropic material

For the most general case of linear elasticity, the relation between the components of the two-dimensional stress tensor σ and the components of the two-dimensional strain tensor ε is expressed by the four-dimensional tensor C which contains $3^4=81$ elements. Using Einstein's summation convention¹ for repeated indices, the generalized Hooke's law can be written as follows:

$$\sigma_{ij} = C_{ijkl}\varepsilon_{kl} \quad (5.1)$$

For reason of the symmetry of the strain tensor ε and the stress tensor σ , the tensor C is reduced to 36 components. Furthermore, the existence of a deformation energy reduces C to a tensor of 21 independent components. Thus, the generalized Hooke's law can be written in the matrix form, as presented in Eq. (5.2).

$$\begin{Bmatrix} \sigma_{11} \\ \sigma_{22} \\ \sigma_{33} \\ \sigma_{23} \\ \sigma_{31} \\ \sigma_{12} \end{Bmatrix} = \begin{bmatrix} C_{1111} & C_{1122} & C_{1133} & C_{1123} & C_{1131} & C_{1112} \\ \dots & C_{2222} & C_{2233} & C_{2223} & C_{2231} & C_{2212} \\ \dots & \dots & C_{3333} & C_{3323} & C_{3331} & C_{3312} \\ \dots & \dots & \dots & C_{2323} & C_{2331} & C_{2312} \\ \dots & \text{sym.} & \dots & \dots & C_{3131} & C_{3112} \\ \dots & \dots & \dots & \dots & \dots & C_{1212} \end{bmatrix} \begin{Bmatrix} \varepsilon_{11} \\ \varepsilon_{22} \\ \varepsilon_{33} \\ 2\varepsilon_{23} \\ 2\varepsilon_{31} \\ 2\varepsilon_{12} \end{Bmatrix} \quad (5.2)$$

Nevertheless, one should keep in mind that both sides of Eq. (5.2) are actually two-dimensional data structures, a fact which must be considered when transforming Hooke's law into other coordinate systems.

1. Each index can have the value 1,2, or 3. If an index appears twice, terms must be added over that index. An index may appear only twice in one term.

5.2.2 Orthotropic and transversely isotropic material

If the elastic material behaviour is symmetric with respect to three orthogonal planes, three main directions can be identified and the material is called orthotropic. In this case the following constants vanish:

$$\begin{aligned} C_{1131} = C_{1112} = C_{2231} = C_{2212} = C_{3331} = C_{3312} = C_{2331} = C_{2312} = 0 \\ C_{1123} = C_{2223} = C_{3323} = C_{3112} = 0 \end{aligned} \quad (5.3)$$

Thus, the elastic behaviour of orthotropic material is described by 9 constants. Provided that the stiffness of the orthotropic material is equal in the \underline{e}_1 direction, the \underline{e}_2 direction, as well as in all directions in the plane defined by \underline{e}_1 and \underline{e}_2 , and differs only in the \underline{e}_3 direction, the material is called transversely isotropic.

$$\begin{aligned} C_{1111} = C_{2222} \quad ; \quad C_{1133} = C_{2233} \\ C_{2323} = C_{3131} \quad ; \quad C_{1212} = C_{1111} - C_{1122} \end{aligned} \quad (5.4)$$

Using Eq. (5.3) and Eq. (5.4) and switching to Mirsky's notation, Eq. (5.2) becomes:

$$\begin{Bmatrix} \sigma_{rr} \\ \sigma_{\theta\theta} \\ \sigma_{zz} \\ \tau_{\theta z} \\ \tau_{rz} \\ \tau_{r\theta} \end{Bmatrix} = \begin{bmatrix} c_{11} & c_{12} & c_{13} & 0 & 0 & 0 \\ \dots & c_{11} & c_{13} & 0 & 0 & 0 \\ \dots & \dots & c_{33} & 0 & 0 & 0 \\ \dots & \dots & \dots & c_{44} & 0 & 0 \\ \dots & \text{sym.} & \dots & \dots & c_{44} & 0 \\ \dots & \dots & \dots & \dots & \dots & c_{66} \end{bmatrix} \begin{Bmatrix} \varepsilon_{rr} \\ \varepsilon_{\theta\theta} \\ \varepsilon_{zz} \\ \gamma_{\theta z} \\ \gamma_{rz} \\ \gamma_{r\theta} \end{Bmatrix} \quad (5.5)$$

representing Hooke's law for transversely isotropic material.

For the derivation of the dynamic equations, this representational form of the stiffness tensor is used. In engineering mechanics, however, it is more

common to write the relation between stress and strain in terms of the Young's modulus E , the shear modulus G , and Poisson's ratio ν as presented in Eq. (5.6). This notation enables one to express simple cases in a very compact form.

$$\{\varepsilon\} = [S] \{\sigma\}$$

$$\begin{Bmatrix} \varepsilon_{11} \\ \varepsilon_{22} \\ \varepsilon_{33} \\ 2\varepsilon_{23} \\ 2\varepsilon_{13} \\ 2\varepsilon_{12} \end{Bmatrix} = \begin{bmatrix} \frac{1}{E_{11}} & -\frac{\nu_{12}}{E_{11}} & \frac{\nu_{13}}{E_{33}} & 0 & 0 & 0 \\ -\frac{\nu_{12}}{E_{11}} & \frac{1}{E_{11}} & \frac{\nu_{13}}{E_{33}} & 0 & 0 & 0 \\ \frac{\nu_{13}}{E_{33}} & \frac{\nu_{13}}{E_{33}} & \frac{1}{E_{33}} & 0 & 0 & 0 \\ 0 & 0 & 0 & \frac{1}{G_{13}} & 0 & 0 \\ 0 & 0 & 0 & 0 & \frac{1}{G_{13}} & 0 \\ 0 & 0 & 0 & 0 & 0 & \frac{2(1+\nu_{12})}{E_{11}} \end{bmatrix} \begin{Bmatrix} \sigma_{11} \\ \sigma_{22} \\ \sigma_{33} \\ \sigma_{23} \\ \sigma_{13} \\ \sigma_{12} \end{Bmatrix} \quad (5.6)$$

The elements c_{ij} of the stiffness tensor $[C]$ are obtained by inversion of the compliance tensor $[S]$.

$$[C] = [S]^{-1} \quad (5.7)$$

$$\begin{aligned}
c_{11} &= \frac{E_{11} (E_{33} - E_{11} v_{13}^2)}{(1 + v_{12}) (E_{33} - E_{33} v_{12} - 2E_{11} v_{13}^2)} \\
c_{12} &= \frac{E_{11} (E_{33} v_{12} + E_{11} v_{13}^2)}{(1 + v_{12}) (E_{33} - E_{33} v_{12} - 2E_{11} v_{13}^2)} \\
c_{13} &= \frac{E_{11} E_{33} v_{13}}{E_{33} - E_{33} v_{12} - 2E_{11} v_{13}^2} \\
c_{33} &= \frac{E_{33}^2 (1 - v_{12})}{E_{33} - E_{33} v_{12} - 2E_{11} v_{13}^2} \\
c_{44} &= G_{13} \\
c_{66} &= \frac{E_{11}}{2(1 + v_{12})}
\end{aligned} \tag{5.8}$$

By combining Eq. (5.5) and Eq. (5.8), the elastic behaviour of the transversely isotropic material is now expressed in terms of E_{11} , E_{33} , G_{13} , v_{12} , and v_{13} .

5.2.3 Dynamic equations for the transversely isotropic rod

The derivation below is based on Mirsky's investigation. It differs, however, in the following points and shall therefore be outlined.

- The numerical handling of Bessel functions with complex arguments is easier today. Therefore a distinction between real and imaginary arguments can be omitted and the solutions can be written in a more compact form.

- Mirsky's investigation treats hollow rods whereas this investigation is limited to full rods representing a certain case of Mirsky's investigation.
- In contrast to this derivation, Mirsky's solution does not contain the lowest torsional mode.

Provided that the principal axis of anisotropy \underline{e}_z is parallel to the longitudinal-(symmetry)-axis of the rod, the dynamic equations can be written as shown in [15], in which u , v , and w denote the displacement components in the radial, circumferential, and axial direction, respectively.

$$\sigma_{rr,r} + \frac{1}{r}\tau_{r\theta,\theta} + \tau_{rz,z} + \frac{1}{r}(\sigma_{rr} - \sigma_{\theta\theta}) = \rho u_{,tt} \quad (5.9)$$

$$\tau_{\theta z,z} + \frac{1}{r}\sigma_{\theta\theta,\theta} + \frac{2}{r}\tau_{r\theta} + \tau_{r\theta,r} = \rho v_{,tt} \quad (5.10)$$

$$\sigma_{zz,z} + \frac{1}{r}\tau_{\theta z,\theta} + \frac{2}{r}\tau_{rz} + \tau_{rz,r} = \rho w_{,tt} \quad (5.11)$$

Substituting Hooke's law [Eq. (5.5)] into Eq. (5.9), Eq. (5.10), and Eq. (5.11) leads to three coupled differential equations for the displacements u , v , and w , which can be expressed in terms of the displacement potentials $\varphi(r, \theta)$, $\psi(r, \theta)$ and the arbitrary constant λ :

$$u(r, \theta, z, t) = \left(\varphi_{,r} + \frac{1}{r}\Psi_{,\theta} \right) \cos(\omega t + kz) \quad (5.12)$$

$$v(r, \theta, z, t) = \left(\frac{1}{r}\varphi_{,\theta} - \Psi_{,r} \right) \cos(\omega t + kz) \quad (5.13)$$

$$w(r, \theta, z, t) = \lambda \varphi \sin(\omega t + kz) \quad (5.14)$$

in which ω is the angular frequency and k is the wavenumber. With the substitution of Eq. (5.12), Eq. (5.13), and Eq. (5.14) into Eq. (5.9), Eq. (5.10), and Eq. (5.11), a new set of differential equations is obtained:

$$\left(\nabla^2 \varphi + \frac{\rho\omega^2 - k^2 c_{44} + \lambda k (c_{44} + c_{13})}{c_{11}} \varphi \right)_{,r} + \frac{1}{r} \left(\nabla^2 \psi + \frac{\rho\omega^2 - k^2 c_{44}}{c_{66}} \psi \right)_{,\theta} = 0 \quad (5.15)$$

$$\frac{1}{r} \left(\nabla^2 \varphi + \frac{\rho\omega^2 - k^2 c_{44} + \lambda k (c_{44} + c_{13})}{c_{11}} \varphi \right)_{,\theta} - \left(\nabla^2 \psi + \frac{\rho\omega^2 - k^2 c_{44}}{c_{66}} \psi \right)_{,r} = 0 \quad (5.16)$$

$$\nabla^2 \varphi + \frac{(\rho\omega^2 - k^2 c_{33}) \lambda}{\lambda c_{44} - k (c_{44} + c_{13})} \varphi = 0 \quad (5.17)$$

A possible solution of Eq. (5.15) and Eq. (5.16) can be written in the form of the following conditions which must both be satisfied:

$$\nabla^2 \psi + \frac{\rho\omega^2 - k^2 c_{44}}{c_{66}} \psi = 0 \quad (5.18)$$

$$\nabla^2 \varphi + \frac{\rho\omega^2 - k^2 c_{44} + \lambda k (c_{44} + c_{13})}{c_{11}} \varphi = 0 \quad (5.19)$$

Eq. (5.17) is identical to Eq. (5.19) if the following additional condition is satisfied:

$$\frac{(\rho\omega^2 - k^2 c_{33}) \lambda}{\lambda c_{44} - k (c_{44} + c_{13})} = \frac{\rho\omega^2 - k^2 c_{44} + \lambda k (c_{44} + c_{13})}{c_{11}} \quad (5.20)$$

representing a quadratic equation for the arbitrary constant λ . Substituting the solutions of Eq. (5.20) (λ_1, λ_2) into Eq. (5.15), Eq. (5.16), and Eq. (5.17) leads to the following set of equations for the potentials $\psi(r, \theta)$ and $\varphi_{1,2}(r, \theta)$.

$$\nabla^2 \psi + q^2 \psi = 0 \quad (5.21)$$

$$\nabla^2 \varphi_1 + p_1^2 \varphi_1 = 0 \quad (5.22)$$

$$\nabla^2 \varphi_2 + p_2^2 \varphi_2 = 0 \quad (5.23)$$

in which

$$q^2 = (\rho \omega^2 - k^2 c_{44}) / c_{66} \quad (5.24)$$

$$p_{1,2}^2 = (\rho \omega^2 - k^2 c_{44} + \lambda_{1,2} k (c_{44} + c_{13})) / c_{11} \quad (5.25)$$

Note that the term $p_{1,2}^2$ has opposite signs compared with Mirsky's investigation [15]. To solve Eq. (5.21), Eq. (5.22), and Eq. (5.23), functions are introduced which consist of harmonic components in the circumferential direction and of the unknown functions $f(r)$, $g_1(r)$, $g_2(r)$.

$$\psi(r, \theta) = f(r) \sin(n\theta) \quad (5.26)$$

$$\varphi_1(r, \theta) = g_1(r) \cos(n\theta) \quad (5.27)$$

$$\varphi_2(r, \theta) = g_2(r) \cos(n\theta) \quad (5.28)$$

in which n is an integer indicating the number of circumferential waves. This leads to the differential equations for the functions $f(r)$, $g_1(r)$, $g_2(r)$:

$$r^2 f_{,rr} + r f_{,r} + (q^2 r^2 - n^2) f = 0 \quad (5.29)$$

$$r^2 g_{1,rr} + r g_{1,r} + (p_1^2 r^2 - n^2) g_1 = 0 \quad (5.30)$$

$$r^2 g_{2,rr} + r g_{2,r} + (p_2^2 r^2 - n^2) g_2 = 0 \quad (5.31)$$

The substitution $z = r\sqrt{q^2}$ transforms the equation for $f(r)$ Eq. (5.29) into a standard Bessel differential equation:

$$z^2 f_{,zz}(z) + z f_{,z}(z) + (z^2 - n^2) f(z) = 0 \quad (5.32)$$

The solution of Eq. (5.32) can be written in terms of Bessel functions of the first kind $J_n(z)$ and Bessel functions of the second kind $Y_n(z)$. Resubstitution of z leads to the solution of the original equation for the function $f(r)$:

$$f(z) = A_1 J_n(z) + B_1 Y_n(z) \Rightarrow f(r) = A_1 J_n\left(r\sqrt{q^2}\right) + B_1 Y_n\left(r\sqrt{q^2}\right) \quad (5.33)$$

in which A_1 and B_1 are arbitrary constants. Note that q^2 can also become negative, leading to Bessel functions with imaginary arguments.

The differential equations for the functions g_1 and g_2 can be solved in a similar manner. The results are:

$$g_1(r) = A_2 J_n\left(r\sqrt{p_1^2}\right) + B_2 Y_n\left(r\sqrt{p_1^2}\right) \quad (5.34)$$

$$g_2(r) = A_3 J_n\left(r\sqrt{p_2^2}\right) + B_3 Y_n\left(r\sqrt{p_2^2}\right) \quad (5.35)$$

5.2.4 Boundary conditions and dispersion relation

The obvious facts that the stress vectors must vanish at the circumferential surface of the rod ($r = R$) and that the stress remains finite on the longitudinal axis of the rod ($r = 0$), provide information for the determination of the constants A_i and B_i of Eq. (5.33), Eq. (5.34), and Eq. (5.35). Since the values of the Bessel functions Y_n go to infinity for r going to zero, the second condition can only be satisfied if all constants B_i are set to zero. The formulation of the stresses at the circumferential surface of the rod leads to a homogeneous system of linear equations for the constants A_1 , A_2 , and A_3 . This system [Eq. (5.36)] has non-trivial solutions only if the determinant of the coefficients equals zero [Eq. (5.37)].

The coefficients a_{ij} are presented in Appendix C of this thesis.

$$\begin{bmatrix} a_{11} & a_{12} & a_{13} \\ a_{21} & a_{22} & a_{23} \\ a_{31} & a_{32} & a_{33} \end{bmatrix} \begin{pmatrix} A_1 \\ A_2 \\ A_3 \end{pmatrix} = \begin{pmatrix} 0 \\ 0 \\ 0 \end{pmatrix} \quad (5.36)$$

$$\text{Det}[a_{ij}] = 0 \quad (5.37)$$

Eq. (5.37) represents the implicit dispersion relation for axisymmetric as well as non-axisymmetric wave modes in a transversely isotropic rod with circular cross-section.

5.2.5 Special case of axisymmetry

Due to experimental reasons, this investigation is limited to axisymmetric, longitudinal/radial, and torsional modes.

In the axisymmetric case, n is set to zero and some coefficients a_{ij} vanish (see Appendix C). Eq. (5.36) becomes:

$$\begin{bmatrix} 0 & a_{12} & a_{13} \\ 0 & a_{22} & a_{23} \\ a_{31} & 0 & 0 \end{bmatrix} \begin{pmatrix} A_1 \\ A_2 \\ A_3 \end{pmatrix} = \begin{pmatrix} 0 \\ 0 \\ 0 \end{pmatrix} \quad (5.38)$$

The corresponding dispersion relation can directly be written as:

$$a_{31} (a_{12}a_{23} - a_{13}a_{22}) = 0 \quad (5.39)$$

Eq. (5.39) has two solutions:

- a) $(a_{12} a_{23} - a_{13} a_{22}) = 0$
- b) $a_{31} = 0$

In case a) the constants of the displacement potentials become:

$$\begin{pmatrix} A_1 \\ A_2 \\ A_3 \end{pmatrix} = \begin{pmatrix} 0 \\ \hat{A}_2 \\ \hat{A}_3 \end{pmatrix}; \quad \sqrt{\hat{A}_2^2 + \hat{A}_3^2} = 1 \quad (5.40)$$

and the potential functions become:

$$\psi(r) = 0$$

$$\varphi_1(r) = \hat{A}_2 J_0(r\sqrt{p_1^2})$$

$$\varphi_2(r) = \hat{A}_3 J_0(r\sqrt{p_2^2}) \quad (5.41)$$

It is now obvious that case a) represents the radial and longitudinal wave motion of the rod, whereas case b) leads to the following constants and potentials:

$$\begin{pmatrix} A_1 \\ A_2 \\ A_3 \end{pmatrix} = \begin{pmatrix} 1 \\ 0 \\ 0 \end{pmatrix} \quad (5.42)$$

$$\psi(r) = J_0(r\sqrt{q^2})$$

$$\varphi_1(r) = 0$$

$$\varphi_2(r) = 0 \quad (5.43)$$

which represent torsional wave motion. Regarding the terms of a_{31} (see Appendix C), one can see that one solution is $q^2 = 0$. According to the

definition of q^2 [see Eq. (5.24)], this leads to the following frequency-wavenumber dependence:

$$\frac{\omega}{k} = c = \sqrt{\frac{C_{44}}{\rho}} = \sqrt{\frac{G_{13}}{\rho}} \quad (5.44)$$

representing the wavespeed for the lowest torsional mode. Curiously, when substituting this solution into Eq. (5.13) all displacements become zero. Therefore Mirsky has forgotten the lowest torsional mode or was simply not interested in it. The reason of this contradiction lies in an assumption which was made when solving the system of differential equations for the potentials φ and ψ [Eq. (5.15) and Eq. (5.16)]. This system is also solvable when the right hand side of Eq. (5.18) is constant rather than zero, a fact which does not change the situation until q^2 equals zero. Then a new differential equation occurs [Eq. (5.45)] leading to the deformation potential of the lowest torsional mode [Eq. (5.46)].

$$\nabla^2 \psi = \psi_{,rr} + \frac{1}{r} \psi_{,r} + \frac{1}{r^2} \psi_{,\theta\theta} = c \quad (5.45)$$

$$\psi(r, \theta) = ar^2 + b\theta^2 \quad (5.46)$$

Since only torsional modes are considered, the constant b must be set to zero.

The dispersion relation can now be calculated by numerically solving the implicit dispersion relations found in Eq. (5.39). Numerical results are presented in the next section.

5.3 Influence of the material constants on the dispersion relation

Provided that the derivation of the dispersion relation above is correct and that the numerical find-root procedure works accurately, the calculation of dispersion relations with shapes similar to those of measured dispersion relations is an almost hopeless task without a rough knowledge of at least some of the five elastic constants. Fortunately the author could rely on three values determined by Dual [45] in an earlier investigation.

Dual used broad band pulses (1-150 kHz) as well as phase-locked resonance measurements to determine the elastic properties of the same specimen. He measured the following values:

$$\begin{aligned}
 E_{33} &= 1.2624 \cdot 10^{11} & [\text{N/m}^2] \\
 \nu_{13} &= 0.32 \\
 G_{13} &= 6.010 \cdot 10^9 & [\text{N/m}^2] \\
 \rho &= 1.5735 \cdot 10^3 & [\text{kg/m}^3] \\
 R &= 5.5 \cdot 10^{-3} & [\text{m}]
 \end{aligned}$$

Since the values for E_{33} and G_{13} are determined directly from the resonance frequencies of longitudinal and torsional vibrations, their accuracy is considerably high when compared with the other parameters.

In order to obtain a complete set of parameters the following values for E_{11} and ν_{12} are estimated:

$$\begin{aligned}
 E_{11} &= 1.21 \cdot 10^{10} & [\text{N/m}^2] \\
 \nu_{12} &= 0.30
 \end{aligned}$$

Despite some uncertainties of the values for E_{11} and ν_{12} , the parameter set above is used as the starting point for the numerical investigation. Therefore one parameter after another is varied and the resulting dispersion curves are compared with those of the standard values.

Similar to the cylindrical shells and the isotropic rod, the dispersion diagram of the transversely isotropic rod (Fig. 5.1) with the values from

above can be divided into three main areas according to its mode shapes: The horizontal tangents close to the frequency axis represent the cut-off frequencies. There the motion is a purely radial breathing motion and the wavelength becomes infinite in longitudinal direction. The steepest parts of the curves are connected with longitudinal wave motions. In contrast to a plate where the longitudinal mode is represented by a continuous line, cylindrical symmetry and lateral contraction of the materials couple radial and longitudinal motion. Thus the steep line is interrupted. The more gradual parts of the curves on the right hand side represent dominantly radial motion.

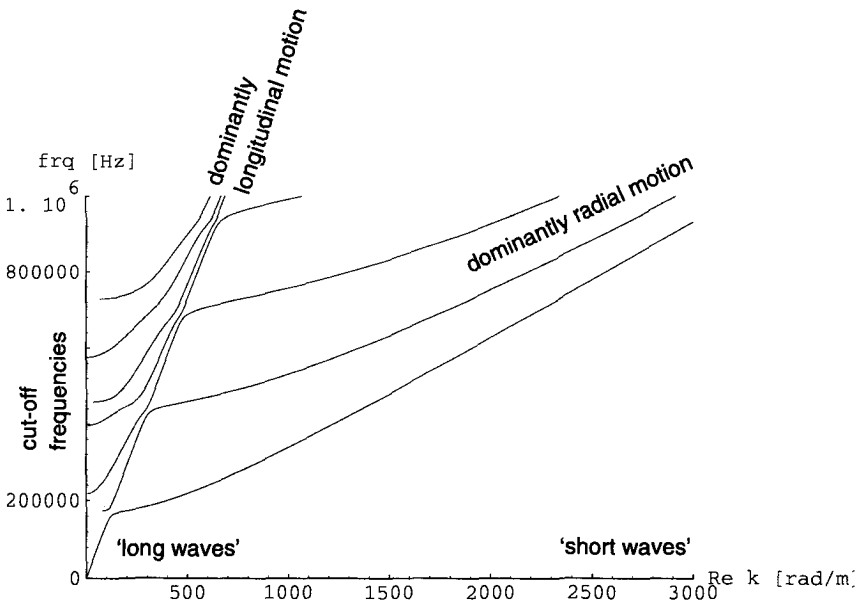


Fig. 5.1 Theoretical dispersion curves of the longitudinal/radial wave modes in a transversely isotropic rod with circular cross-section (diameter: 11 mm).

Fig. 5.2 shows the dispersion curves of the torsional modes which are essential for the complete characterization of the material. The mode shape of the lowest mode is equal to the static torsional deformation of the rod. It is not dispersive. To visualize the shapes of the higher modes, one should consider the rod as a number of concentric shells, twisted

alternatingly in clockwise and anticlockwise directions (see Fig. 5.3). Therefore the lowest mode is sensitive to G_{13} (which equals G_{23})¹ only, whereas the higher modes are sensitive to G_{13} and G_{12} , a constant which is not explicitly varied in this section. Eq. (5.47), however, shows that G_{12} changes when the stiffness in radial direction E_{11} and/or the Poisson's ratio ν_{12} is varied.

$$G_{12} = \frac{E_{11}}{2(1 + \nu_{12})} \quad (5.47)$$

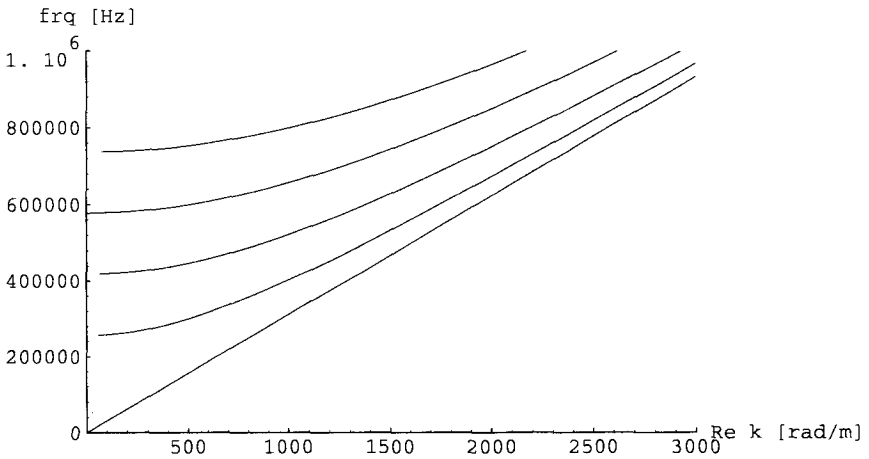


Fig. 5.2 Theoretical dispersion curves of the torsional wave modes in a transversely isotropic rod with circular cross-section (diameter: 11 mm).

The cut-off frequencies of the higher torsional modes can directly be obtained from Eq. (5.39). Therefore the value for the wavenumber k must be set to zero, indicating wavelength of infinite longitudinal extent.

-
1. \mathbf{e}_1 radial unit base vector
 - \mathbf{e}_2 circumferential unit base vector
 - \mathbf{e}_3 longitudinal unit base vector

Eq. (5.48) shows the implicit equation for the cut-off frequencies ω_c . The only deformation that occurs when the wavelength becomes infinite ($k = 0$) is shear in the cross-sectional plane. Therefore G_{12} is the only material constant in Eq. (5.48).

$$\frac{\rho\omega_c^2}{G_{12}} J_0\left(\omega_c R \sqrt{\frac{\rho}{G_{12}}}\right) - \frac{2\sqrt{G_{12}\rho}}{R} \omega_c J_1\left(\omega_c R \sqrt{\frac{\rho}{G_{12}}}\right) = 0 \quad (5.48)$$

If the wavelength becomes finite ($|k| > 0$), the additional stiffness of G_{13} will be involved, thus increasing the frequency of the higher torsional modes.

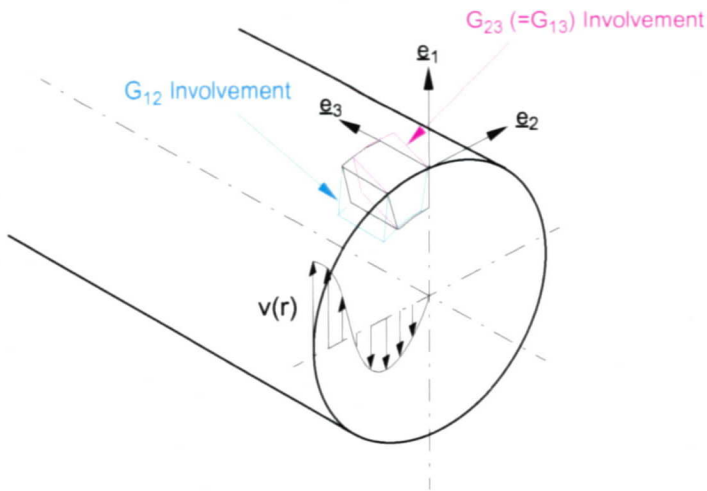


Fig. 5.3 Illustration of the mode shape of the second torsional mode in a transversely isotropic rod with the principal axis of anisotropy e_3 . Illustration of two kinds of shear deformation associated with the torsional mode shapes.

On the following pages, the black curves show the dispersion relation of the standard values and the red curves show the dispersion relation when one parameter is varied.

5.3.1 Variation of the Young's modulus E_{33}

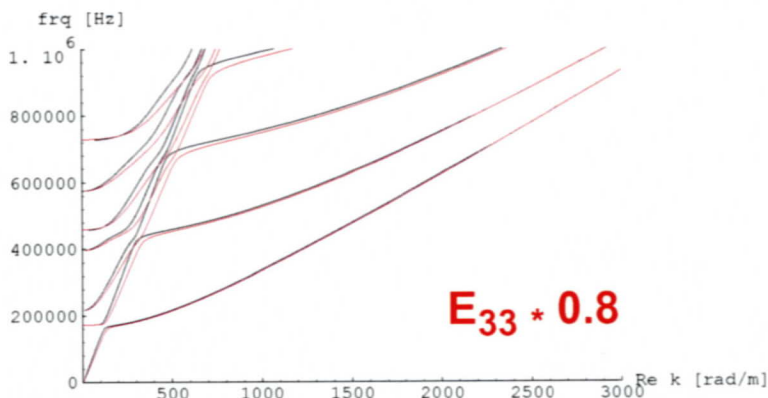


Fig. 5.4 Longitudinal/radial modes; variation of E_{33} .

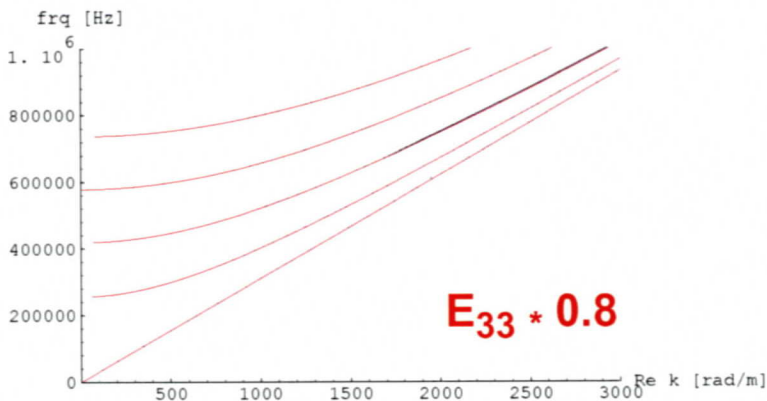


Fig. 5.5 Torsional modes; variation of E_{33} .

- A lower value for E_{33} leads to a lower speed of longitudinal waves.
- Cut-off frequencies, torsional modes, and the areas where the motion is mainly radial remain unchanged.
- A higher value for E_{33} leads to opposite effects.

5.3.2 Variation of the shear modulus G_{13}

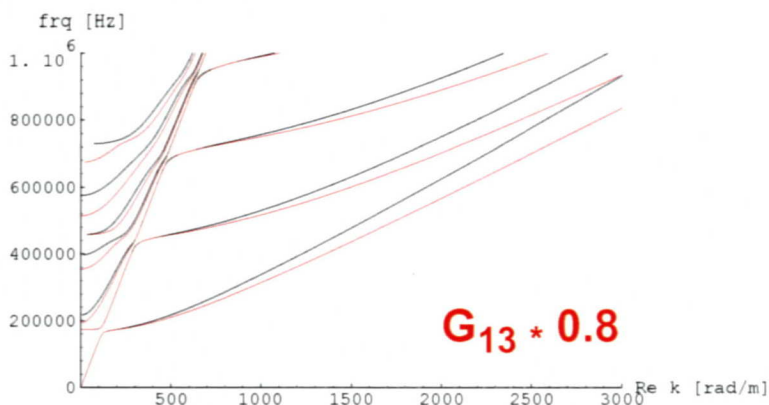


Fig. 5.6 Longitudinal/radial modes; variation of G_{13} .

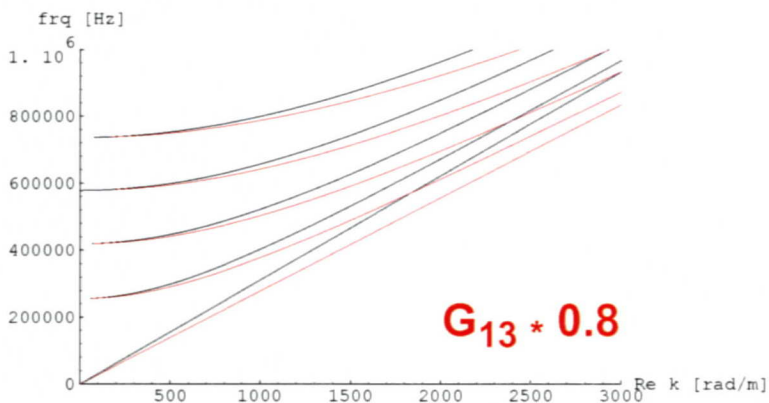


Fig. 5.7 Torsional modes; variation of G_{13} .

- The main effect of a lower shear modulus G_{13} (which equals G_{23}) is the lower speed of all torsional modes and of the radial modes for 'short' wavelength.
- The radial cut-off frequencies are shifted to lower values.
- A higher value for G_{13} leads to opposite effects.

5.3.3 Variation of the Young's modulus E_{11}

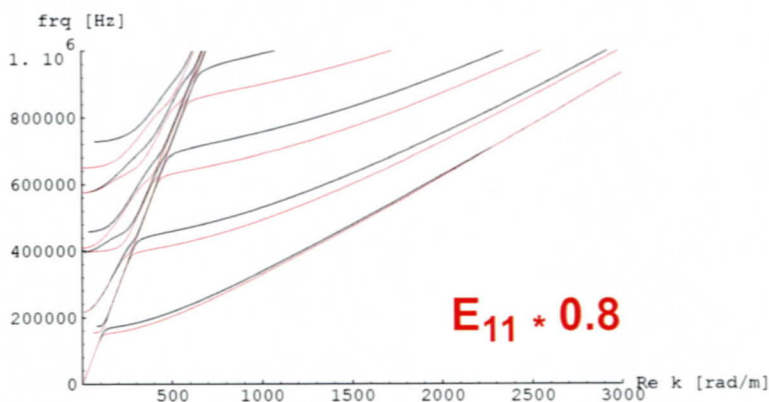


Fig. 5.8 Longitudinal/radial modes; variation of E_{11} .

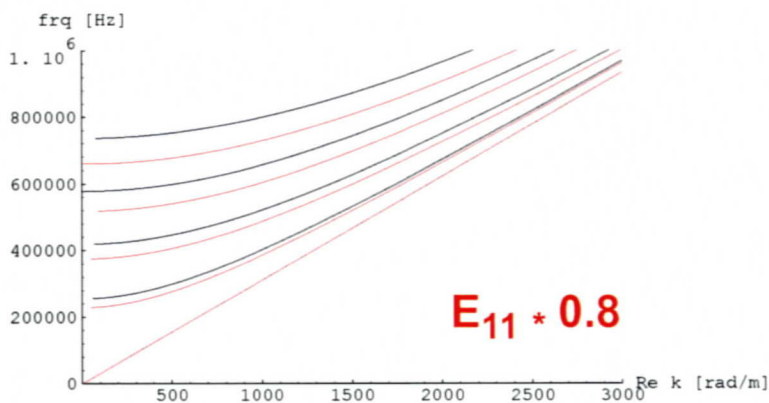


Fig. 5.9 Torsional modes; variation of E_{11} .

- With a lower value for E_{11} , the cut-off frequencies decrease and the coupling areas are shifted to lower frequencies (see Fig. 5.8).
- Only the higher torsional modes are affected [see Eq. (5.47)].
- The speed of longitudinal waves remains unchanged.
- A higher value for E_{11} leads to opposite effects.

5.3.4 Variation of the Poisson's ratio ν_{12}

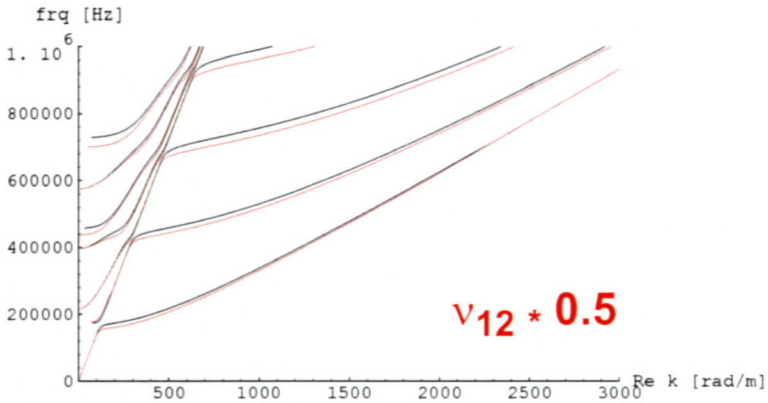


Fig. 5.10 Longitudinal/radial modes; variation of ν_{12} .

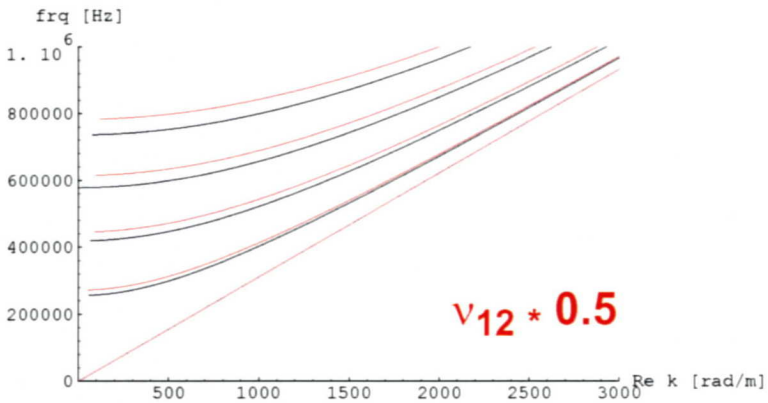


Fig. 5.11 Torsional modes; variation of ν_{12} .

- A lower value for ν_{12} shifts the coupling area to lower frequencies.
- According to Eq. (5.47), a lower value for ν_{12} increases the value of G_{12} , resulting in higher cut-off frequencies of the higher torsional modes.
- A higher value for ν_{12} leads to opposite effects.

5.3.5 Variation of the Poisson's ratio ν_{13}

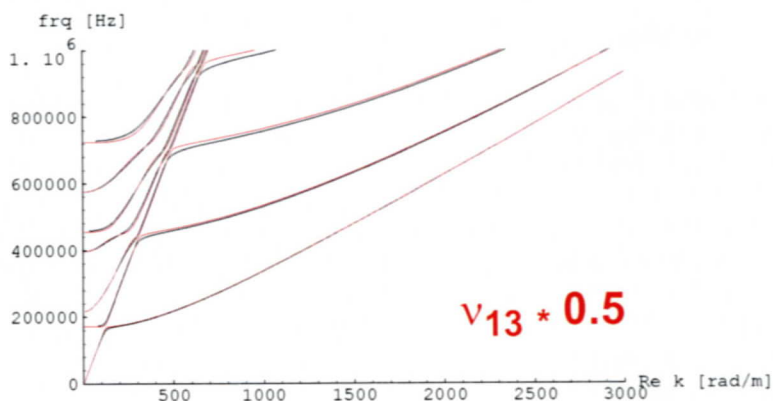


Fig. 5.12 Longitudinal/radial modes; variation of ν_{13} .

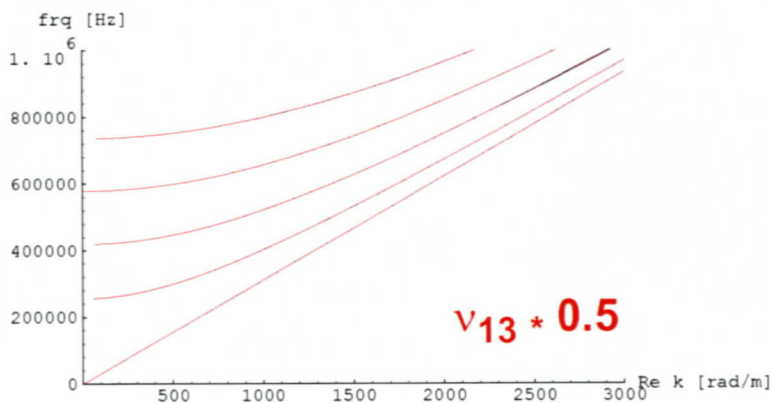


Fig. 5.13 Torsional modes; variation of ν_{13} .

- In general, the influence of ν_{13} is minor when compared with the other constants.
- Slight changes occur only in the coupling area between radial and longitudinal motion.
- A higher value for ν_{13} leads to opposite effects.

5.4 Experiments

5.4.1 Longitudinal and radial modes

The experimental procedure for the detection of longitudinal/radial wave modes is exactly the same as for the isotropic aluminium rod (see Chapter 3) with the following exception:

The complexity of the material leads to even more difficulties in exciting axisymmetric wave modes exclusively. Therefore the displacement functions are measured and recorded at 160 points along one side of the rod. The rod is then turned around its longitudinal axis by 180° and the displacement functions are measured again. By averaging the measurements of two subtended points, at least some non-axisymmetric components can be eliminated.

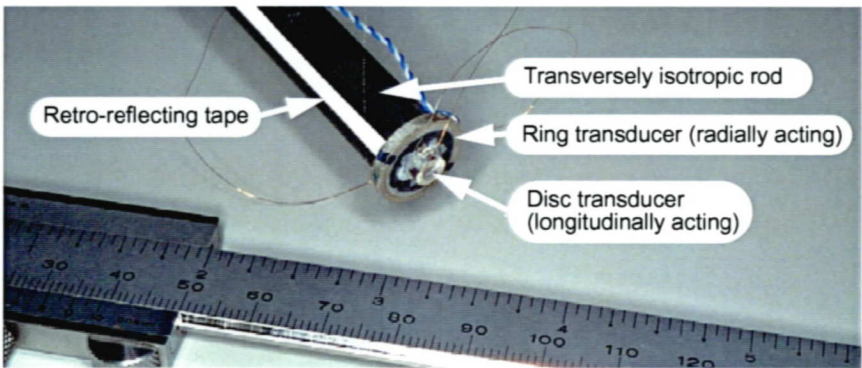


Fig. 5.14 Excitation unit for longitudinal/radial wave modes in a transversely isotropic rod with circular cross-section (diameter: 11 mm).

For the experimental results below, linear sweep pulses with a start frequency of 300 kHz, a stop frequency of 1200 kHz, and duration of 0.5 ms are applied repeatedly with a frequency of 20 Hz. In order to detect longitudinal and radial components of the displacement, the angle between the LASER beam and the longitudinal axis of the rod is adjusted to 45° . In contrast to the aluminium rod, the damping appears to be much higher, resulting in a clear detectability only for outgoing pulses from the piezo-excitation.

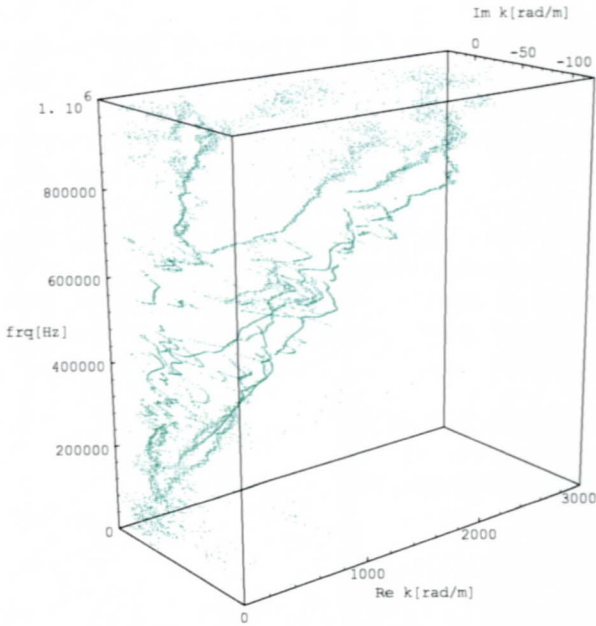


Fig. 5.15 Measured dispersion relation of longitudinal/radial wave modes in a transversely isotropic rod with circular cross-section (diameter: 11 mm).

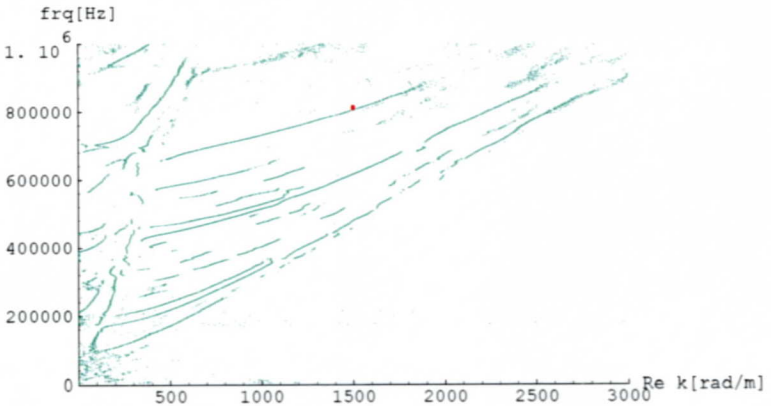


Fig. 5.16 Projection of the curves presented in Fig. 5.15 into the real plane.

5.4.2 Torsional modes

To excite torsional waves, a longitudinally polarized ring transducer is cut into four segments. The electrodes are attached to the new surfaces, which occur when cutting the ring. Thus the circumferential electric field causes a circumferential shear deformation of the piezo segments. The technique described above was developed in the PhD thesis of Dual [17]. These segments are glued on a transmission disc as shown in Fig. 5.17. To be able to excite higher torsional modes, the transmission disc is connected with the transversely isotropic rod on a narrow ring close to the circumferential surface of the rod only. For the excitation of the torsional waves, the same linear sweep pulses are used as for the longitudinal/radial excitation (300 kHz to 1200 kHz during 0.5 ms).

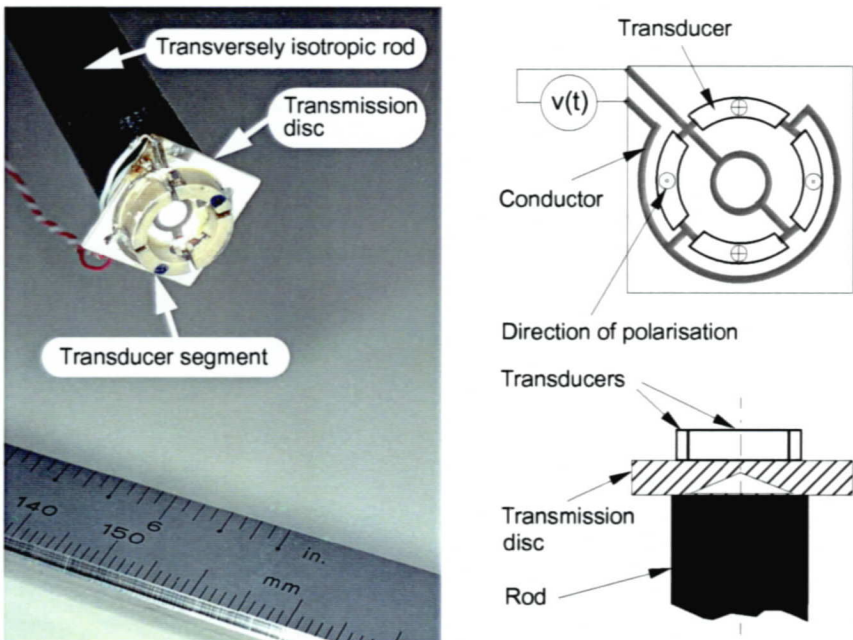


Fig. 5.17 Excitation unit for torsional wave modes in a transversely isotropic rod with circular cross-section (diameter: 11 mm).

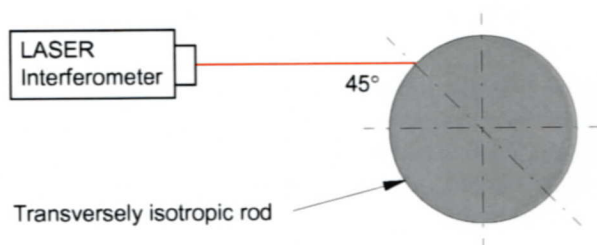


Fig. 5.18 Positioning of the LASER beam for the detection of torsional wave modes.

Fig. 5.18 shows the configuration of the measuring LASER beam relative to the cross-section of the specimen used to measure circumferential movements. It is obvious that lateral components of the surface displacement which are always present due to imperfections of the excitation, the support devices, or the material itself are detected as well.

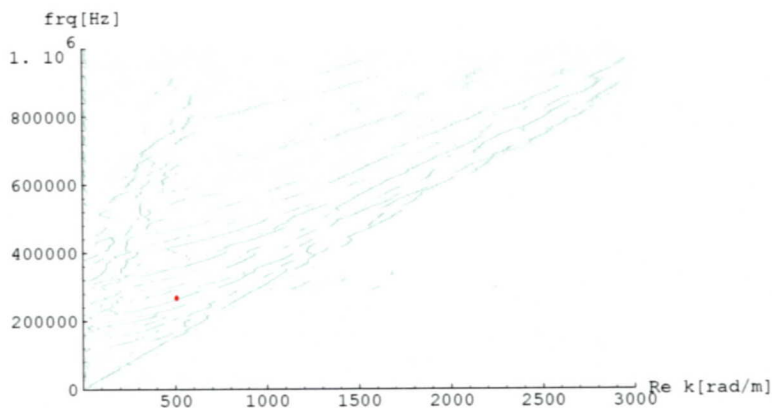


Fig. 5.19 Measured dispersion relation of waves in a transversely isotropic rod with torsional excitation (projection of the curves into the real plane).

5.5 Determination of the material constants from the measured dispersion relation

The diagrams in Section 5.3 show that each of the five possible variations leads to characteristic changes in the dispersion curves. Thus the five elastic constants can now be determined from the measured dispersion relations by systematic, iterative variations. For the determination of the constants E_{11} and ν_{12} , the inverse problem, leading from two measured points directly to the values of the constants, can be solved as outlined below.

5.5.1 Determination of E_{33} and G_{13}

G_{13} equals G_{23} , a modulus which can be determined from the lowest torsional mode. The value presented by Dual [45] can be confirmed in this manner. The situation for E_{33} , the longitudinal stiffness of the rod, is very similar, since its variation affects the speed of longitudinal waves only and the value found for the best fit is equal to the one in Dual's investigation.

5.5.2 Determination of E_{11} and ν_{12}

Regarding Fig. 5.8 to Fig. 5.11, one can see that for lower values of E_{11} and ν_{12} the curves of the longitudinal/radial modes are both shifted towards lower frequencies.

The torsional modes, on the other hand, behave different: Whereas a lower value for E_{11} results in lower curves of the higher torsional modes, the same curves rise towards higher frequencies when ν_{12} is reduced. This effect leads to the following concept:

From the measured dispersion relation two points are chosen, one from a higher longitudinal/radial mode and one from a higher torsional mode. Provided that the specific longitudinal/radial curve and the specific torsional curve of the calculated dispersion relation coincide with the measured points chosen, the values of E_{11} & ν_{12} pairs fulfilling this condition are calculated for the point on the longitudinal/radial mode as well as for the point on the torsional mode. This procedure leads to two crossing curves in the E_{11} ν_{12} plane (Fig. 5.20); one for the point on the longitudinal/radial mode (blue curve) and the other for the point on the torsional

mode (red curve). The cross point in the $E_{11} \nu_{12}$ plane represents the particular pair of values (E_{11} and ν_{12}) which fulfils the condition of coincidence for both points, the one on the longitudinal/radial mode and the one on the torsional mode. In this investigation a point on the third longitudinal/radial modes ($k = 1500$ [rad/m], frq = 811 ± 2 [kHz]) and one on the second torsional mode ($k = 500$ [rad/m], frq = 262 ± 1 [kHz]) are chosen. The points are indicated by red dots in Fig. 5.16 and Fig. 5.19.

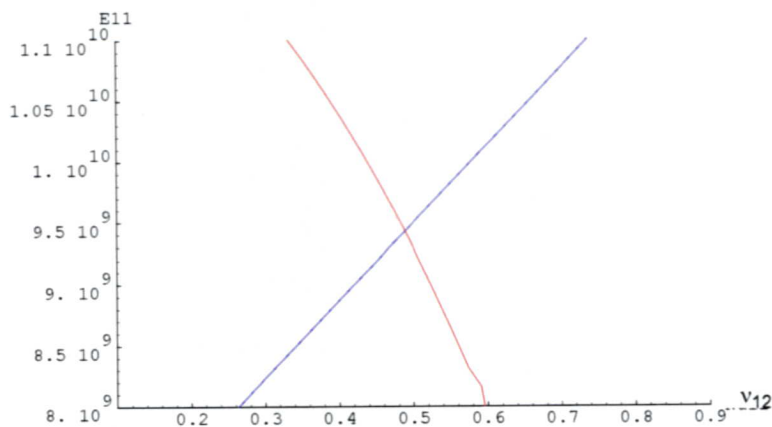


Fig. 5.20 Blue: $E_{11} \nu_{12}$ pairs which fulfil the longitudinal/radial dispersion relation in such a way that it coincides with the measured point ($k = 1500$ [rad/m], frq = 811 [kHz]).

Red: $E_{11} \nu_{12}$ pairs which fulfil the torsional dispersion relation in such a way that it coincides with the measured point ($k = 500$ [rad/m], frq = 262 [kHz]).

The values at the cross point are:

$$E_{11} = 9.43 \cdot 10^9 \quad [\text{N/m}^2]$$

$$\nu_{12} = 0.488$$

The frequencies of the measured points are given with a certain accuracy. In order to estimate the consequence of the accuracy of E_{11} and ν_{12} , the curves presented in Fig. 5.20 are calculated for the same wavenumbers and for frequencies which are varied by ± 10 [kHz]. Then the accuracy intervals are calculated by linear interpolation.

$$E_{11} = 9.43 \cdot 10^9 \pm 0.1 \cdot 10^9 \quad [\text{N/m}^2]$$

$$\nu_{12} = 0.488 \pm 0.02$$

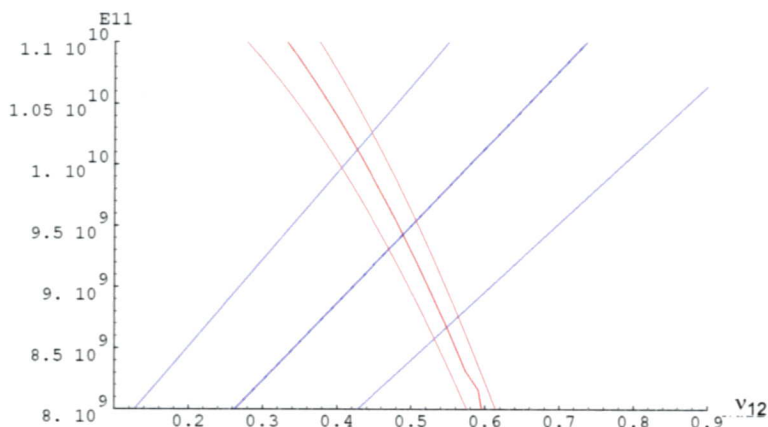


Fig. 5.21 Blue: E_{11} ν_{12} pairs for the points $k = 1500$ [rad/m], $\text{frq} = 801/811/821$ [kHz] of the longitudinal/radial dispersion relation.

Red: E_{11} ν_{12} pairs for the points $k = 500$ [rad/m], $\text{frq} = 272/262/252$ [kHz] of the torsional dispersion relation.

5.5.3 Determination of ν_{13}

The determination of ν_{13} is the final step in fitting the theoretical model into the measured dispersion relations. In Fig. 5.12 and Fig. 5.13 one can see that a 50% reduction of the value of ν_{13} leads to very small changes in the coupling area of the longitudinal/radial modes only. Magnifying these areas, however, enables the determination of ν_{13} with an accuracy similar to the other constants.

5.5.4 Results for the best fit

The calculated dispersion curves, visible as red curves in Fig. 5.22 and Fig. 5.23, are based on the following values which provide the best fit:

$E_{11} =$	$9.43 \cdot 10^9$	$\pm 0.1 \cdot 10^9$ [N/m ²]
$E_{33} =$	$1.2624 \cdot 10^{11}$	$\pm 0.005 \cdot 10^{11}$ [N/m ²]
$\nu_{13} =$	0.320	± 0.02
$\nu_{12} =$	0.488	± 0.02
$G_{13} =$	$6.010 \cdot 10^9$	$\pm 0.005 \cdot 10^9$ [N/m ²]
$\rho =$	$1.5735 \cdot 10^3$	$\pm 0.001 \cdot 10^3$ [kg/m ³]
$R =$	$5.5 \cdot 10^{-3}$	$\pm 0.001 \cdot 10^{-3}$ [m]

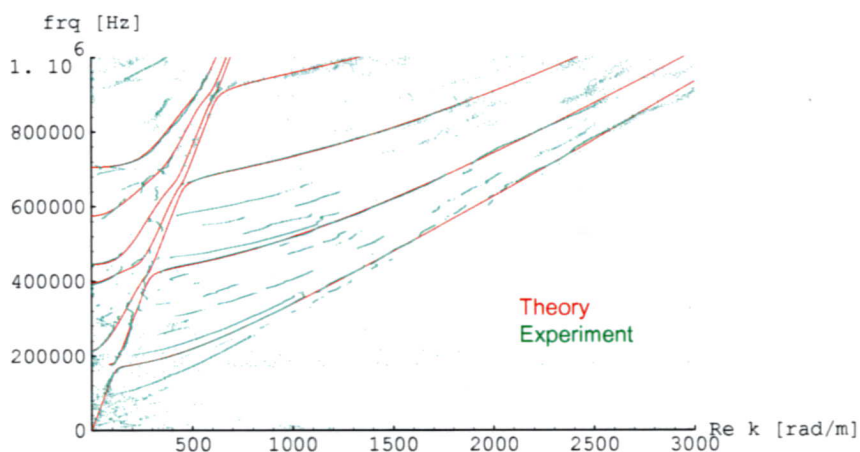


Fig. 5.22 Superposition of theoretical and measured dispersion curves of longitudinal/radial modes in a transversely isotropic rod with circular cross-section (diameter: 11 mm).

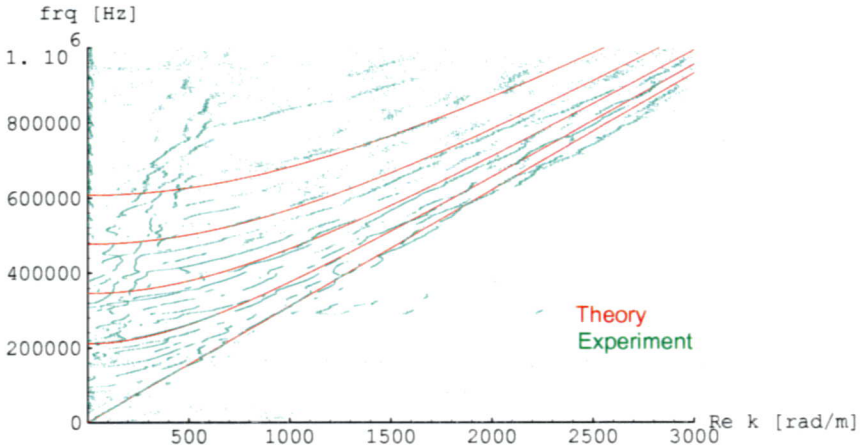


Fig. 5.23 Superposition of theoretical and measured dispersion curves of torsional modes in a transversely isotropic rod with circular cross-section (diameter: 11 mm).

Despite the fact that many other, probably non-axisymmetric, modes are present in the diagram in Fig. 5.23, the combination of values above is the only possible one.

In general, the accuracy of the modes which have been determined by prior resonance experiments (E_{33} and G_{13}) and which are verified by this method is very high, followed by the accuracy of E_{11} . Since the sensitivity of the dispersion curves to changes in the Poisson's ratios is distinctly lower when compared with the other modes, the accuracy is estimated to be a few percent.

A detailed quantification of the confidence intervals, however, demands primarily a systematic investigation of the accuracy of the spectrum estimation methods applied in this section.

5.6 Conclusions

The complete set of five elastic constants describing the dynamic behaviour of transversely isotropic material could be determined with considerable accuracy in a nondestructive way over a wide frequency range. To the author's knowledge, this is one of the first investigations to provide a complete nondestructive elastic characterisation of anisotropic material with high accuracy and reliability.

Applications for the inspection of existing structures are conceivable as well as the investigation of new types of anisotropic materials to check the validity of laminate theories.

The extension of the theoretical and experimental methods presented in this thesis towards the investigation of higher non-axisymmetric modes in order to evaluate material properties of even more sophisticated systems such as orthotropic rods or shells is mainly a question of computer capacity and can therefore be considered very optimistically.

Another aspect concerns the clear detectability of the attenuation of various wave modes (see Fig. 5.24).

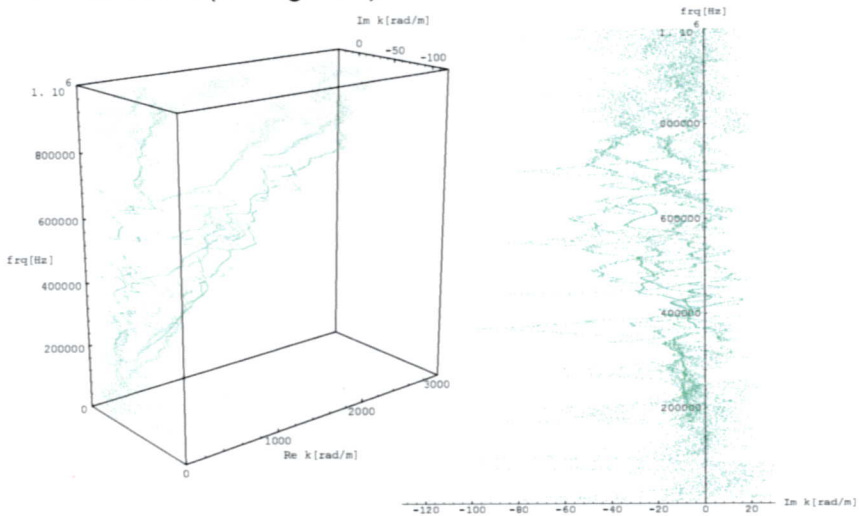


Fig. 5.24 Measured complex dispersion relation of longitudinal/radial wave modes in a transversely isotropic rod (left) and its projection into the imaginary plane (right).

Regarding Fig. 5.24 and by comparing it with the corresponding diagram of an isotropic aluminium rod (Fig. 4.15), the quickly changing imaginary parts of the propagating wave modes seem to illustrate a highly complex energy interchange between various modes which is caused by the anisotropy and/or by the viscoelastic behaviour of the matrix. A similar shape of the imaginary wavenumbers versus frequency occurs when the dispersion curves of a shell filled with polyisobutylene (high viscosity) is measured, as presented in Fig. 4.11. In both cases it can be observed that the 'net' attenuation is growing with the frequency.

Research efforts should therefore be devoted to establishing theoretical models which permit predictions of the attenuation behaviour of various fibre-matrix combinations of composite rods. Whether such a step could be undertaken within the frame of homogenized complex material parameters or whether new complex lamina theories need to be developed is an open question. A possible experimental approach to this field could be the investigation of a rod which consists of the matrix material only. Provided that the viscoelastic material of the matrix can be described by a reasonable number of parameters, the elastic constants of the anisotropic material could then be extended with frequency-dependent, imaginary components.

6 Outlook

Research is a continuous flow whereas a thesis has a beginning and an end, at best providing some starting points for further investigations or at least new approaches and ideas. With this in mind, the author would like to outline some aspects in conjunction with future work.

- The tools developed in this thesis enable one to investigate the dynamic behaviour of any solid materials (including anisotropic materials), viscoelastic materials, and liquids in a broad frequency range. The Maxwell model, used to describe the viscoelastic core material in Chapter 2, can easily be replaced by another time dependent constitutive relation between stress and strain.
- Applications in the fields of chemistry and biology in which suspensions of particles or cells need to be analysed or supervised, are conceivable as long as the particles and the distances between them are small compared with the length of the waves. The 'smooth' way in which the mechanical properties of highly fragile structures such as suspensions of cells are measured could be a decisive advantage when compared with other methods.
- Modern spectrum estimation methods have been widely used since the 1980s in the fields of astronomy, geophysics, communication engineering, medical imaging and underwater acoustics, just to mention a few examples. The development of these algorithms as well as the number of potential applications is strongly connected with the astounding growth and availability of computer capacities, a process which is at the beginning rather than at the end.
- In contrast to the well-established Fast Fourier Transform method (FFT), spectrum analysis with the methods of linear prediction and complex total least squares, as used in this thesis, can distinguish between the positive and negative harmonic components of the signal and, furthermore, can supply information about the attenuation or the growth of a component by extracting its imaginary part. These extensions are highly advantageous when analysing structures

by guided mechanical waves since inhomogeneities such as cracks can cause reflections, and viscoelasticity or radiation loss in neighbouring media can cause attenuation.

- In the field of nondestructive evaluation and/or characterization of materials and structures, the author expects a wide variety of potential applications. The analysis of guided, attenuating, one-dimensional waves in various cylindrical structures containing viscoelastic and anisotropic components shows promising results, thus encouraging the extension of approaches presented in this thesis.
- One possible direction for future work could be the extension of the measurement technique towards two-dimensional wave propagation phenomena. This step would permit the characterization and inspection of structures like anisotropic plates, sandwich plates, or orthotropic shells. In the case of orthotropic shells or rods, higher non-axisymmetric wave modes could be excited and detected in order to determine further elastic constants. The present experimental set-up would be sufficient for a first series of experiments.
- The detectability of the complex harmonic components and therefore the quality of the dispersion measurements could be improved in many ways. Excitation methods which are more specific for one particular family of wave modes could be elaborated and the angle between the LASER beam and the surface of the specimen could be optimized, just to give a few examples.
- Since the LASER interferometer used in this investigation permits the detection of movements in a frequency range of up to 8 MHz, a higher storage depth of the digital storage oscilloscope would increase the interval in which dispersion relations could be measured.
- As far as the results of the spectrum estimation method can be compared with those obtained by other methods, perfect agreement is found as shown for the isotropic aluminium rod and partially for the anisotropic rod. To increase the confidence in these new methods, however, the author suggests a systematic investigation of their accuracy and resolution limits as a function of the number of samples and

the signal-to-noise ratio. This investigation, which is of particular importance in the range of complex components, could be carried out based on synthetic signals.

- Another aspect concerns the inverse problem. Once the complex dispersion relation for a particular family of waves can be calculated and measured, the parameters of interest need to be extracted from the measured dispersion relation in an iterative process. In the rather simple case of one-dimensional wave propagation in cylindrical structures in which some areas of the dispersion diagram can be identified, which are governed by one or two parameters only, this iterative process can be performed in an interactive way as presented in Chapter 5. In future applications with increasingly complex structures and wave modes, this inversion could become one of the main obstacles in the way of developing new nondestructive evaluation methods. Therefore the author suggests the application of neural network methods. Based on a theoretical dispersion relation, a neural network could be trained through the influence of various geometrical and constitutional parameters on the topology of the complex dispersion relation of guided mechanical waves. In a second step, the trained neural network could then be used to find an optimal fit for the measured curves, thus providing the structural parameters of interest.

Since the spectral estimation method provides single dots which form the dispersion curves, parametric modelling algorithms could be applied in order to reduce the amount of experimental data. The parameterized dispersion curves could then be used more readily by the neural network process.

- Apart from detecting dispersion relations of propagating waves, spectrum estimation methods can also be applied to extract the harmonic components from signals in the time domain. During the writing of this thesis, a first, successful attempt was made to adapt the methods of linear prediction and total least squares to modal analysis of the structure of a railroad car, with the aim of analysing its dynamic behaviour in order to reduce the acoustic emission.

Appendix A: Matrix m_{ij}

Here the coefficients of the linear system used in Eq. (2.46) are presented. These expressions are derived from Eq. (2.37), Eq. (2.14), and Eq. (2.15). The constants D (bending stiffness of a plate) and C (longitudinal stiffness of plate) are written in terms of c_p , h and ρ_s , because these terms can be measured more readily on an empty shell.

$$D = \frac{c_p^2 h^3 \rho_s}{12}; \quad C = c_p^2 \rho_s h; \quad c_p^2 = \frac{E}{\rho_s (1 - \nu^2)}; \quad c_2^2 = \frac{G}{\rho_s} = \frac{E}{2\rho_s (1 + \nu)}$$

$$m_{11} = 0$$

$$m_{12} = 1$$

$$m_{13} = \beta_\phi * J_1 (\beta_\phi * R)$$

$$m_{14} = -ik * J_1 (\beta_\psi * R)$$

$$m_{21} = 1$$

$$m_{22} = -\frac{i\omega}{c} \left(1 - \frac{c^2}{c_2^2 \kappa} \right) \frac{h}{2} \cdot \frac{1}{2} \left(\text{Sign} \left[1 - \frac{(\text{Re}[c])^2}{c_2^2 \kappa} \right] + 1 \right)$$

$$m_{23} = ik * J_0 (\beta_\phi * R)$$

$$m_{24} = -\beta_\psi * J_0 (\beta_\psi * R)$$

$$m_{31} = -\frac{ik * c_p^2 h \rho_s \nu}{\kappa G R} \left(\frac{k^2 c_p^2 h^2 \rho_s}{12} + \kappa G - \frac{\rho_s h^2 \omega^2}{12} \right)$$

$$m_{32} = \frac{k^{*4} c_p^2 h^3 \rho_s}{12} - \left(\frac{c_p^2 \rho_s}{\kappa G} + \frac{1}{12} \right) k^{*2} \omega^2 \rho_s h^3 + \frac{k^{*2} c_p^4 h^3 \rho_s^2}{12 \kappa G R^2} \\ - \left(1 + \frac{c_p^2 \rho_s h^2}{12 \kappa G R^2} \right) \rho_s h \omega^2 + \frac{c_p^2 h \rho_s}{R^2} + \frac{\omega^4 \rho_s^2 h^3}{12 \kappa G}$$

$$m_{33} = \frac{-1}{12 \kappa G} (12 \kappa G - \rho_s h^2 \omega^2 + k^{*2} c_p^2 h^2 \rho_s) \\ \{ J_0(\beta_\phi^* R) [k^{*2} \lambda^* + (\lambda^* + 2\mu^*) \beta_\phi^{*2}] - J_1(\beta_\phi^* R) \left[\frac{2\mu^* \beta_\phi^*}{R} \right] \} \\ + (ik^* \mu^* h) J_1(\beta_\phi^* R) [ik^* \beta_\phi^*]$$

$$m_{34} = \frac{-1}{12 \kappa G} (12 \kappa G - \rho_s h^2 \omega^2 + k^{*2} c_p^2 h^2 \rho_s) \\ \{ -J_0(\beta_\psi^* R) [2ik^* \mu^* \beta_\psi^*] + J_1(\beta_\psi^* R) \left[\frac{2ik^* \mu^*}{R} \right] \} \\ + \frac{(ik^* \mu^* h)}{2} J_1(\beta_\psi^* R) [k^{*2} - \beta_\psi^{*2}]$$

$$m_{41} = \omega^2 - c_p^2 k^{*2}$$

$$m_{42} = \frac{-ik^* v c_p^2}{R}$$

$$m_{43} = \frac{i\mu^*}{\rho_s h} J_1(\beta_\phi^* R) [2k^* \beta_\phi^*]$$

$$m_{44} = \frac{\mu^*}{\rho_s h} J_1(\beta_\psi^* R) [k^{*2} - \beta_\psi^{*2}]$$

in which $\text{Sign}[x] = 1$ for $x > 0$, $\text{Sign}[x] = -1$ for $x < 0$, and $\text{Sign}[x] = 0$ for $x = 0$. $\text{Re}[c]$ takes the real part of the complex phase velocity c .

Appendix B: Shell theory versus exact theory

To ensure the validity of the shell theory derived in Chapter 2, the interaction with the viscoelastic medium can be excluded, reducing Eq. (2.46) to:

$$\begin{bmatrix} 0 & 0 & 0 & 0 \\ 0 & 0 & 0 & 0 \\ m_{31} & m_{32} & 0 & 0 \\ m_{41} & m_{42} & 0 & 0 \end{bmatrix} \begin{pmatrix} a_x \\ a_r \\ a_1 \\ b_1 \end{pmatrix} = \begin{pmatrix} 0 \\ 0 \\ 0 \\ 0 \end{pmatrix}$$

leading to the dispersion condition for the empty shell:

$$m_{31}m_{42} - m_{41}m_{32} = 0$$

The results of this equation are compared with a three-dimensional, exact solution published by Herrmann and Mirsky [24] in which several shell theories for shells of 'medium' thickness are compared.

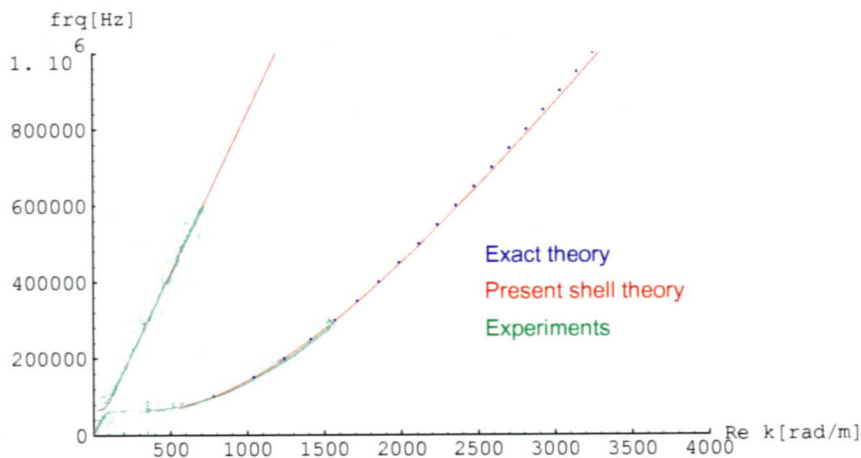


Fig. B.1 Present shell theory (red curves) vs. exact theory according to Herrmann and Mirsky [24] (blue dots) vs. experimental results (green dots).

The curves in Fig. B.1 are based on the following parameters:

Radius of the shell-mid plane	$R =$	12.85	mm
Shell wall thickness	$h =$	0.55	mm
Young's modulus	$E =$	$2.000 \cdot 10^{11}$	N/m^2
Poisson's ration	$\nu =$	0.28	
Density	$\rho =$	7800	kg/m^3 .
Timoshenko's factor	$\kappa =$	0.8	

The maximum deviation of the phase velocities of the flexural mode at 1 Mhz between the exact theory and the present shell theory amounts to less than 1 %. Thus the present shell theory appears to be sufficient as long as neither the frequency range nor the ratio formed by the shell wall thickness and the shell radius are increased.

The small difference between the theoretical and the experimental curves for the flexural mode is probably caused by a boundary layer of air diminishing the wavespeed, an effect which is not considered in this calculation, or caused by a non-optimal value for κ .

Appendix C: Matrix a_{ij}

Here the coefficients of the dispersion relation for waves in a transversely isotropic rod, presented in Eq. (5.36), are listed. The variable n as well as the index n for the Bessel functions indicates the number of circumferential waves, which equals zero for all axisymmetric wave modes.

$$a_{11} = \frac{2c_{66}n}{R^2} (n-1) J_n(R\sqrt{q^2}) - \frac{2c_{66}n}{R} \sqrt{q^2} J_{n+1}(R\sqrt{q^2})$$

$$a_{12} = \left(c_{44}k^2 + \frac{2c_{66}n}{R^2} (n-1) - \omega^2\rho - c_{44}k\lambda_1 \right) J_n(R\sqrt{p_1^2}) + \frac{2c_{66}}{R} \sqrt{p_1^2} J_{n+1}(R\sqrt{p_1^2})$$

$$a_{13} = \left(c_{44}k^2 + \frac{2c_{66}n}{R^2} (n-1) - \omega^2\rho - c_{44}k\lambda_2 \right) J_n(R\sqrt{p_2^2}) + \frac{2c_{66}}{R} \sqrt{p_2^2} J_{n+1}(R\sqrt{p_2^2})$$

$$a_{21} = -\frac{c_{44}kn}{R} J_n(R\sqrt{q^2})$$

$$a_{22} = \frac{c_{44}n}{R} (\lambda_1 - k) J_n(R\sqrt{p_1^2}) + c_{44}\sqrt{p_1^2} (k - \lambda_1) J_{n+1}(R\sqrt{p_1^2})$$

$$a_{23} = \frac{c_{44}n}{R} (\lambda_2 - k) J_n(R\sqrt{p_2^2}) + c_{44}\sqrt{p_2^2} (k - \lambda_2) J_{n+1}(R\sqrt{p_2^2})$$

$$a_{31} = c_{66} \left(q^2 + \frac{2n}{R^2} (1-n) \right) J_n(R\sqrt{q^2}) - \frac{2c_{66}}{R} \sqrt{q^2} J_{n+1}(R\sqrt{q^2})$$

$$a_{32} = \frac{2c_{66}n}{R^2} (1-n) J_n \left(R\sqrt{p_1^2} \right) + \frac{2c_{66}n}{R} \sqrt{p_1^2} J_{n+1} \left(R\sqrt{p_1^2} \right)$$

$$a_{33} = \frac{2c_{66}n}{R^2} (1-n) J_n \left(R\sqrt{p_2^2} \right) + \frac{2c_{66}n}{R} \sqrt{p_2^2} J_{n+1} \left(R\sqrt{p_2^2} \right)$$

in which

$$\lambda_{1,2} = \frac{-B \pm \sqrt{B^2 - 4AC}}{2A}$$

$$A = c_{44} (c_{13} + c_{44}) k$$

$$B = (c_{11}c_{33} - c_{13}^2 - 2c_{13}c_{44} - 2c_{44}^2) k^2 + (\rho c_{44} - \rho c_{11}) \omega^2$$

$$C = (c_{13} + c_{44}) k (c_{44}k^2 - \rho\omega^2)$$

Bibliography

- [1] L. Pochhammer, **“Ueber die Fortpflanzungsgeschwindigkeit kleiner Schwingungen in einem unbegrenzten isotropen Kreiscylinder”**, Journal für die reine und angewandte Mathematik. In zwanglosen Heften, Band 81, pp 324-336, Berlin (1876).
- [2] N. Joukowsky, **“Ueber den hydraulischen Stoss in Wasserleitungsrohren”**, Mémoir de l’Academie Impérial de Sciences de St. Petersburg, Vol.9, 8.Ser., No. 5 (1900).
- [3] R. Skalak, **“An Extension of the Theory of Water Hammer”**, Paper No. 55-S-18, Hydraulics Division, ASME, Baltimore, MD, (1955).
- [4] C.R. Fuller and F. J. Fahy, **“Characteristics of Wave Propagation and Energy Distributions in Cylindrical Elastic Shells Filled with Fluid”**, Journal of Sound and Vibration, 81 (4), pp 501-518, (1982).
- [5] J.H. Heimann and H. Kolsky, **“The Propagation of Elastic Waves in Thin Cylindrical Shells”**, Journal of the Mechanics and Physics of Solids, Vol. 14, pp 121-130, (1966).
- [6] T.C. Lin and G. W. Morgan, **“Wave Propagation through Fluid Contained in a Cylindrical, Elastic Shell”**, Journal of the Acoustical Society of America, Vol. 28 (6), pp 1165-1176, (1956).
- [7] Y.P. Guo, **“Approximate solutions of the dispersion equation for fluid-loaded cylindrical shells”**, Journal of the Acoustical Society of America, Vol. 95(3), pp 1435-1440, (1994).
- [8] Y.P. Guo, **“Attenuation of helical wave radiation from cylindrical shells by viscoelastic layer”**, Journal of the Acoustical Society of America, Vol. 95(3), pp 1435-1440, (1994).
- [9] T.J. Plona et al., **“Axisymmetric wave propagation in fluid-loaded cylindrical shells. II: Theory versus experiment”**, Journal of the Acoustical Society of America, Vol. 92 (2), pp. 1144-1155, (1992).

- [10] B.K. Sinha et al., "**Axisymmetric wave propagation in fluid-loaded cylindrical shells. I: Theory**", Journal of the Acoustical Society of America, Vol. 92 (2), pp. 1132-1143, (1992).
- [11] L.D. Lafleur and F. D. Shields, "**Low-Frequency Propagation Modes in a Liquid-filled Elastic Tube Waveguide**", Journal of the Acoustical Society of America, Vol. 97 (3), pp. 1435-1445, (1995).
- [12] J. Zemanek, "**An Experimental and Theoretical Investigation of Elastic Wave Propagation in a Cylinder**", Journal of the Acoustical Society of America, Vol. 51 (1), pp. 265-283, (1972).
- [13] N. Krause, W. Goldsmith, and J.L. Sackman, "**Transients in Tubes containing Liquids**", International Journal of Mechanical Science, Vol. 19, pp 53-68, (1977).
- [14] F. Barez, W. Goldsmith, and J.L. Sackman, "**Longitudinal Waves in Liquid-filled Tubes I (Theory) and II (Experiments)**", International Journal of Mechanical Science, Vol. 21, pp 213-236, (1979).
- [15] I. Mirsky, "**Wave Propagation in Transversely Isotropic Circular Cylinders, Part I: Theory**", Journal of the Acoustical Society of America, Vol. 37(6), pp. 1016-1021, (1965).
- [16] I. Mirsky, "**Wave Propagation in Transversely Isotropic Circular Cylinders, Part II: Numerical Results**", Journal of the Acoustical Society of America, Vol. 37(6), pp. 1022-1026, (1965).
- [17] J. Dual, "**Experimental Methods in Wave Propagation in Solids and Dynamic Viscometry**", Diss. ETH No. 8659, Zürich, (1988).
- [18] N.A. Shulga, "**Propagation of Axisymmetrical Elastic Waves in an Orthotropic Hollow Cylinder**", Soviet Applied Mechanics 10, No. 9, (1974).
- [19] E.I. Ramskaya, N.A. Shulga, "**Study of the Velocities and Modes of Propagation of Axisymmetric Waves along an Orthotropic Hollow Cylinder**", Soviet Applied Mechanics 19, No. 3, (1983).

- [20] J.D. Achenbach, "**Wave Propagation in Elastic Solids**", North-Holland, Amsterdam, (1993).
- [21] K.F. Graff, "**Wave Motion in Elastic Solids**", Oxford University Press, Oxford, (1975).
- [22] S.P. Timoshenko, "**On the Correction for Shear of the Differential Equation for Transverse Vibrations of Prismatic Bars**", Philosophical Magazine, Vol.41, pp 125-131, (1921).
- [23] G.R. Cowper, "**The Shear Coefficient in Timoshenko's Beam Theory**", Journal of Applied Mechanics, Vol. 33, pp 335-340, (1966).
- [24] G. Herrmann and I. Mirsky, "**Three-Dimensional and Shell-Theory Analysis of Axially Symmetric Motions of Cylinders**", Journal of Applied Mechanics, Vol.23, pp 563-568, (1956).
- [25] M. Abramowitz and I.A. Stegun, "**Handbook of Mathematical Functions**", Dover Publications, New York, (1968).
- [26] S.M. Kay, "**Modern Spectral Estimation: Theory and Application**", Prentice-Hall, Englewood Cliffs, N.J. (1988).
- [27] S.L. Marple Jr., "**Digital Spectral Analysis**", Prentice-Hall, Englewood Cliffs, N.J. (1987).
- [28] S.L. Marple Jr., "**A Tutorial Overview of Modern Spectral Estimation**", Proc. IEEE, pp. 2152-2157, (1989).
- [29] M.H. Hayes, "**Statistical Digital Signal Processing and Modelling**", John Wiley & Sons, Inc., New York, (1996).
- [30] S. Oestreich, "**Digitale Spektralanalyse, Theorie und Anwendung bei Vibrationssignalen**", Dissertation, Universität der Bundeswehr München, München, (1992).
- [31] M. Uike, T. Uchiyama, and H. Minamitani, "**Comparison of Linear Prediction Methods Based on Singular Value Decomposition**", Journal of Magnetic Resonance, Vol. 99, pp. 363-371, (1992).

- [32] C.F. Tirendi and J.F. Martin, "**Quantitative Analysis of NMR Spectra by Linear Prediction and Total Least Squares**", Journal of Magnetic Resonance, Vol.85, pp. 162-169, (1989).
- [33] G.H. Golub and C.F. Van Loan, "**An Analysis of the Total Least Squares Problem**", SIAM (Society for Industrial and Applied Mathematics) Journal, Vol. 17, No. 6, (December 1980).
- [34] G.H. Golub and C.F. Van Loan, "**Matrix Computations**", 2nd edition, Johns Hopkins University Press, Baltimore, (1989).
- [35] J. Dual, M. Hägeli, M.R. Pfaffinger, J. Vollmann, "**Experimental Aspects of Quantitative Nondestructive Evaluation using Guided Waves**", Ultrasonics, Vol.34, pp. 291-295, Elsevier Science, Amsterdam, (1996).
- [36] R. Prony, "**Essai Expérimental et Analytique sur les lois de la Dilatabilité des fluides élastiques et sur celles de la Force expansive de la vapeur de l'eau et de la vapeur de l'alkool, à différentes températures.**", Journal Polytechnique ou Bulletin du Travail fait à L'Ecole Centrale des Travaux Publics, Paris, Premier Cahier, An. III (1795).
- [37] F.B. Hildebrand, "**Introduction to Numerical Analysis**", 2nd edition, McGraw-Hill, New York, (1974).
- [38] S.L. Marple Jr., "**A New Autoregressive Spectrum Analysis Algorithm**", presented at the 12th Annu. Asilomar Conf. Circuits and Systems, Asilomar, California, (Nov. 1978).
- [39] D. W. Tufts and R. Kumaresan, "**Estimation of Frequencies of Multiple Sinusoids: Making Linear Prediction Perform like Maximum Likelihood**", Proc. of the IEEE, Vol. 70 (9), pp. 975-989, (1982).
- [40] S. Van Huffel and J. Vandewalle, "**The Total Least Squares Problem, Computational Aspects and Analysis**", SIAM (Society for Industrial and Applied Mathematics), Philadelphia, (1991).

- [41] M. Onoe, H.D. McNiven, R.D. Mindlin, "**Dispersion of Axially Symmetric Waves in Elastic Rods**", *Journal of Applied Mechanics*, Vol. 29 (61 - 4), pp. 729-734, (1962).
- [42] R.T. Folk, "**Time Dependent Boundary Value Problems in Elasticity**", Ph.D. Dissertation, Lehigh University, Bethlehem, Pennsylvania, (1958).
- [43] A.H. Meitzler, "**Backward-Wave Transmission of Stress Pulses in Elastic Cylinders and Plates**", *Journal of the Acoustical Society of America*, Vol. 38, pp. 835-842, (1965).
- [44] J. Wolf, T.D.K. Ngoc, R. Kille, and W.G. Mayer, "**Investigation of Lamb waves having a negative group velocity**", *Journal of the Acoustical Society of America*, Vol. 83 (1), pp. 122-126, (1988).
- [45] J. Dual, "**Dynamic Measurements of Elastic Properties in Solid Circular Cylinders**", *Ultrasonics International 93, Conference Proceedings*, pp. 319-322, (1993).

Curriculum vitae

Johannes Vollmann

Born on 1 April 1964 in Baden, Switzerland.

- 1971 - 1980 Primary and secondary school in Oberrohrdorf, AG Switzerland.
- 1980 - 1984 Practical, mechanical apprenticeship at Brown Boveri Ltd. (today ABB, Asea Brown Boveri), Baden, Switzerland. Journeyman examination as Maschinenmechaniker.
- 1984 Employment as Maschinenmechaniker at ABB. Fulfilment of Swiss Army requirement.
- 1984 - 1987 Studies at the Department of Mechanical Engineering of the HTL Brugg-Windisch (Swiss Engineering College). Graduation with the degree Masch.-Ing. HTL.
- 1987 Practical training at Shin Meiwa Industry Co. Ltd. Takarazuka-shi, Hyogo-ken, Japan.
- 1987 - 1992 Studies at the Department of Civil and Structural Engineering of the Swiss Federal Institute of Technology ETH, Zürich, Switzerland. Graduation with the degree Dipl. Bau-Ing. ETH. Awarded the first Heinrich Hatt-Bucher Prize, 1992.
- 1991 Practical training at Mosproject - 3, Kuznetsky Most, Moscow, Russia.
- 1992 - 1996 *Doctoral student, research and teaching assistant at the Institute of Mechanics of the ETH Zürich.*
- 1995 Awarded the R.W.B. Stephens Prize at the Ultrasonics International Conference, Edinburgh, Scotland, July 1995.
- 1996 Awarded the IUTAM Bureau Prize at the 19th International Congress of Theoretical and Applied Mechanics, Kyoto, Japan, August 1996.

